HYDRODYNAMIC CHARACTERISTICS AND CAPILLARY-ASSISTED HEAT TRANSFER ENHANCEMENT OF NON-CONDENSING/CONDENSING TWO-PHASE FLOWS

A Dissertation

presented to

the Faculty of Graduate School

at the University of Missouri-Columbia

In Partial Fulfilment

of the Requirements for the Degree

Doctor of Philosophy

By

MILAD DARZI

Dr. Chanwoo Park, Dissertation Supervisor

May 2020

The undersigned, appointed by the dean of the Graduate School, have examined the dissertation entitled

HYDRODYNAMIC CHARACTERISTICS AND CAPILLARY-ASSISTED HEAT TRANSFER ENHANCEMENT OF NON-CONDENSING/CONDENSING TWO-PHASE FLOWS

presented by Milad Darzi,

a candidate for the degree of Doctor of Philosophy in Mechanical Engineering

and hereby certify that, in their opinion, it is worthy of acceptance.

Professor Chanwoo Park

Professor Yuwen Zhang

Professor Gary L. Solbrekken

Professor Hongbin Ma

Professor Jacob McFarland

Professor Stephen Montgomery-Smith

ACKNOWLEDGEMENTS

I would like to appreciate my supervisor Dr. Chanwoo Park for his guidance and support through conducting this research at University of Missouri-Columbia.

I would like to express my sincerest gratitude to my committee members for their willingness to serve on my committee and for providing me with precious suggestions and insightful comments.

I would also like to thank my fellow labmates for their stimulating discussions, friendship, and all the fun we have had in the past years. Mr. Minwoo Lee, and Ms. Elnaz Norouzi, it would have been a lonely lab without you. I wish you all the best and I look forward to working with you in the future.

Very special thanks are to my parents, Maryam and Houshang, who love and encourage me by standing by me to overcome all difficulties in study and life. Your sacrificial love and gracious support are my drive to reach my goals in all my life. You have given me so much, and in return, so little. There is no way for me to express my utmost gratitude to you.

TABLE OF CONTENTS

LIST OF FIGURES

LIST OF TABLES

NOMENCLATURE

A	cross-sectional area, surface area [m^2]
AR	aspect ratio [-]
Bo	Bond number, Bo=$(\rho_L - \rho_G)gD^2/\sigma$ [-]
C	Courant number, $C=u\Delta t/\Delta x$ [-]
Ca	Capillary number, Ca=$\mu u/\sigma$ [-]
c_p	specific heat capacity, [J/kg-K]
D	tube dimeter [m]
EF	enhancement factor [-]
$\boldsymbol{F}$	force per length [N/m]
Fr	Froude number [-], Fr=$J/(gD)^{0.5}$
G	mass flux [kg/m^2-s]
g	gravity [m/s^2]
g_o	normal gravity constant, 9.8 m/s^2
h	capillary rise [mm], heat transfer coefficient [W/m^2-K]
i	enthalpy [J]
J	superficial velocity [m/s]
J_g	dimensionless vapor velocity [-]
L	distance, or length [m]
n	refraction indices of media [-]
k	thermal conductivity [W/m-K]
K_c	adjustable coefficient [-]
Nu	Nusselt number [-]
p	pressure [Pa]
PF	penalty factor [-]
PEC	performance evaluation criteria [-]
Pr	Prandtl number [-]
p_r	reduced pressure [-]
Q	volumetric flow rate [m^3/s]
q''	heat flux [W/m2]
$\dot{q}$	volumetric heat rate [W/m^3-s]

r	radial coordinate, radius of porous tube [m]
R	tube radius [m]
S	surface area [m^2], slip ratio [-]=u_G/u_L
Re	Reynolds number [-]
t	time [s], tube wall thickness [mm]
T	temperature [°C], total time [s]
$\boldsymbol{u}$	velocity [m/s]
V	volume [m^3]
v	vertical distance [mm]
w	pore width [μm]
We	Weber number [-]
x	vapor quality [-], x-coordinate in a Cartesian system [mm]
y	y-coordinate in a Cartesian system [mm]
X	Martinelli parameter [-]
z	axial coordinate [m], z-coordinate in a Cartesian system [mm]
Δp	pressure drop [Pa]

Greek Letters

α	phase fraction in a computational cell [-], angle [deg]
β	volumetric fraction [-], $\beta_G=J_G/J_m$, $\beta_L=J_L/J_m$
γ, δ, Ω	angle [deg]
ε	error [%], void fraction [-], $\varepsilon=V_G/(V_G+V_L)$ or $A_G/(A_G+A_L)$
μ	dynamic viscosity [Pa/s]
υ	kinematic viscosity [m^2/s]
ρ	density [kg/m^3]
δ	liquid film thickness, wire thickness [μm]
σ	surface tension [N/m^{-1}]
τ	shear stress [N/m^2]
κ	interface curvature [m^{-1}]
Δ	annular gap dimension [mm]
θ	contact angle [°]

Subscripts

1,2	location indices
1φ	single-phase
2φ	two-phase
a	actual
ave	average
b	bulk, bubble, bisector, buoyancy
bare	bare tube
c	computed, or corrected, capillary
CFL	Courant–Friedrichs–Lewy condition
D	dynamic
d	distorted, detachment
e	exact, equilibrium
f	fluid
G	gas
GT	gas total
g	gas, hydrostatic head
i	inner, interfacial
L	liquid
l	liquid
LO	Liquid only
lim	limitation
m	mixture, momentum
mass	mass conservation
max	maximum
o	outer
p	point, cell index
PTI	porous-tube-insert
r	rod
s	liquid slug, superficial
sat	saturation
su	slug unit

t	translational
TB	Taylor bubble
w	wall

Superscripts

$'$	shifted or corrected

Symbols

$< >$	area-averaged
$\bar{}$	time-averaged

ABSTRACT

Interfacial characteristics of two-phase flows were studied through visualization experiments and numerical simulation using computational fluid dynamics (CFD) based on the volume-of-fluid (VOF)-continuum surface force (CSF) method. An experimentally-validated analytical method was also presented for the geometrical correction of the optically-distorted objects in cylindrical tubes that is applicable to geometrical measurements (e.g., liquid-gas interfaces, solid particles, gas bubbles, void fraction) inside the tubes. The numerically-simulated two-phase flows agreed favorably with the visually-observed flows. The simulation of two-phase flows under reduced gravities indicated the important contribution of gravity on hydrodynamics of intermediate scale two-phase flows such as void fraction, pressure drop, slip ratio, and bubble velocity; the pressure drop of horizontal plug/bubble flows and Taylor bubble velocity of vertical slug flow is minimum around normal gravity. The computational model is then extended to account for convective and condensation heat transfer. The numerical results for a vertical slug flow show that a porous-tube-insert (PTI) promotes the internal liquid circulations in both axial and radial directions resulting in an enhanced convective heat transfer up to five times of that in bare tube. In addition, the PTI enhances the flow condensation heat transfer up to three times mainly due to the enforced ultra-thin liquid film near the tube wall and increased area for thin-film condensation.

1 CHAPTER 1: INTRODUCTION

1.1 CAPILLAY FLOW AND DYNAMIC CONTACT ANGLE

The fluid's flow in capillaries has been the subject of interest for decades due to the significance in various applied sciences such as geoscience [1], biotechnology [2], lab-on-a-chip [3], space [4], enhanced oil recovery [5], microelectronics cooling technology [6], and MEMS technology [7]. The classical analytical model describing the capillary-driven flow of a liquid through uniform circular capillaries is the Lucas−Washburn−Rideal (LWR) equation [8-10]:

$$\rho h\frac{d^2h}{dt^2}=\frac{2\sigma\cos\theta}{R}-\rho\left(\frac{dh}{dt}\right)^2-8\frac{\mu}{R^2}h\frac{dh}{dt}-\rho gh, \tag{1-1}$$

where h is capillary rise, σ is surface tension, μ is liquid viscosity, ρ is liquid density and R is the tube's radius, and θ is the triple point (liquid-gas-solid intersection) equilibrium (static) contact angle. The terms on the right hand side in Eq. (1-1) represent various governing forces of surface tension, inertia, viscous, and gravity, respectively. Note that the gas-liquid surface evaporation was neglected in Eq. (1-1).

Although the contact angle changes during the capillary flow, the LWR equation [Eq. (1-1)] was originally solved assuming the constant equilibrium contact angle. This assumption helps to simplify the problem which still provide valuable information. The LWR equation using constant contact angle is applicable for several important applications such as inject printing [11], food processing [12], and petroleum engineering [13]. However, experimental data show a slower capillary rise than that predicted by the LWR equation using a constant contact angle [14-16]. Such deviation was attributed to many possible factors such as the uncertainty of capillary radius [16], possible formation of gas

bubbles in liquid [16], entrance effect [17, 18], displaced gas (outlet) effect [19], and instantaneous (dynamic) contact angle [14, 15]. Amon all those parameters, the dynamic contact angle (θ_D) is believed to be the most important one affecting the inaccurate calculation of the capillary flow [20]. In addition, in several real world situations, this equilibrium state is never reached and the dynamic contact angle is important.

There has been numerous theoretical and experimental researches to correct the original LWR equation by replacing the constant (equilibrium) contact angle, (θ_e) with the dynamic contact angle (θ_D). And thus, several correlations have been proposed in literature that was comprehensively discussed by Wu et al. [20]. It is well-known that the dynamic contact angle strongly depends on the velocity of the triple point contact line. This means that the instantaneous velocity of the meniscus should be known to find the contact angle in each moment of the capillary flow that is beyond an analytical treatment. Therefore, the non-dimensional correlations for dynamic contact angle are functions of capillary number (Ca = $\mu u/\sigma$), where μ is the liquid viscosity, u is the speed of the interface, and σ is the liquid-gas surface tension. Table 1.1-1 summarizes the important predictive correlations for DCA that has been published in literature. The conditions in which the correlation models were derived are also included in Table 1.1-1.

Table 1.1-1 Correlations for prediction of dynamic contact angle (DCA)

Author(s)	Experiment	Correlation model
Joos et. al (1990) [21]	Droplet (on a surface)	$\cos\theta_D = \cos\theta_e - 2(1+\cos\theta_e)\mathrm{Ca}^{1/2}$
Tanner (1979) [22]	Droplet	$\mathrm{Ca}=k(\theta_D-\theta_e)^3$ k : material constant obtained empirically

Cox (1986) [23]	Droplet	$\mathrm{Ca} = \left(\ln\left(\varepsilon^{-1}\right) - \frac{Q_1}{f(\theta_D)} + \frac{Q_2}{f(\theta_e)} \right)^{-1} \times$ $\left[g(\theta_D) - g(\theta_e) \right] + O\left(\frac{1}{\ln\left(\varepsilon^{-1}\right)} \right)^3$ $Q_1 \,\&\, Q_2$:constants associated with outer flow and wall slip ε :small dimensionless parameter associated with micro-region of contact line f & g : functions defined in [23]
Hoffman (1975) [24]	Droplet	$\theta_D^3 - \theta_e^3 \cong c_T \mathrm{Ca}$ c_T : constant from [25]
Shikhmurzaev et al. (1993) [26]	Droplet	$V = \frac{\sin\theta_D - \theta_D \cos\theta_D}{\sin\theta_D \cos\theta_D - \theta_D}$
Cox-Voinov [23, 25]	Droplet	$\theta_D^3 = \theta_e^3 \pm 9\mathrm{Ca} \ln\left(\frac{L}{l}\right)$ l : slip length ($\approx 10^{-9}$), L :characteristic length α : constant dependent on geometry
Blake-Haynes (1969) [27]	Droplet	$\theta_D = \cos^{-1}\left[\cos\theta_e - \frac{2k_B T}{\gamma\lambda^2} \sinh^{-1}\left(\frac{V}{2K_\omega \lambda} \right) \right]$ k_B : Boltzmann constant, T : temperature (K) λ : distance between adsorption sites on the solid surface ($\approx 10^{-9} m$) K_ω : equilibrium frequency of the random molecular displacements occurring within the three-phase zone ($\approx 10^6 s^{-1}$)
Jiang et. al (1979) [28]	Capillary rise	$\frac{\cos\theta_e - \cos\theta_D}{\cos\theta_e + 1} = \tanh\left(4.96\mathrm{Ca}^{0.702}\right)$
Kistler (1993) [29]	Droplet	$\theta_D = f_H\left[\mathrm{Ca} + f_H^{-1}(\theta_e) \right]$

		$f_H(x) = \arccos\left\{1 - 2\tanh\left[5.16\left(\frac{x}{1+1.31x^{0.99}}\right)^{0.706}\right]\right\}$ f_H is Hoffman's function and f_H^{-1} is its inverse function
Blake (1993) [27]	Capillary rise	$h_t = 2\kappa_s^0 \lambda \frac{h}{\eta\upsilon}\sinh\left(\frac{\sigma\left[\cos\theta_e - \cos\theta_D\right]}{2nkT}\right)$ κ_s^0: κ_w^0 is the frequency of molecular displacements at equilibrium and $\kappa_s^0 = \kappa_w^0 \frac{\eta\nu}{h}$ κ: Boltzmann's constant ($=1.38\times10^{-23}\,J/K$) h: Plank's constant $=6.63\times10^{-34}\,Js$ T: Temperature, ν: molecular flow volume (volume of one molecule for 'simple' fluids) λ: distance between adsorption sites on the solid surface ($\approx 10^{-9}\,m$) n: number of adsorption sites per unit area
Seeberg et. al (1992) [30]	Capillary rise	$\frac{\cos\theta_e - \cos\theta_D}{\cos\theta_e + 1} = 4.47\mathrm{Ca}^{0.42}$ for $\mathrm{Ca} \le 10^{-3}$ $\frac{\cos\theta_e - \cos\theta_D}{\cos\theta_e + 1} = 2.24\mathrm{Ca}^{0.54}$ for $Ca > 10^{-3}$
Kalliadasis (1994) [31]	Capillary rise	$\tan\theta_D = \left[\tan^3\theta_e + 9\left\lvert\log\left(\left(R_m/R\right)\mathrm{Ca}^{2/3}\right)\right\rvert\mathrm{Ca}\right]^{1/3}$ $\lambda = R_m/R$ where R is the radius of the tube and R_m for most liquids is in the order of Ångström. So as mentioned in [31], if $Ca \ll \lambda$, second-term on the right hand side can be ignored.

Zhou (1990) [32]	Capillary rise	$G(\theta)=G(\theta_e)+\mathrm{Ca}\ln\left(\frac{K}{l_s}\right), G(q)=\int_0^q d\phi\left[f(\phi)\right]^{-1}$ & $f(\phi)=\frac{\left[2\sin\phi\left\{\begin{matrix}q^2\left(\phi^2-\sin^2\phi\right)+2q\left[\phi(\pi-\phi)+\sin^2\phi\right]\\+(\pi-\phi)^2-\sin^2\phi\end{matrix}\right\}\right]}{\left\{\begin{matrix}q\left(\phi^2-\sin^2\phi\right)\left[(\pi-\phi)+\sin\phi\cos\phi\right]+\\(\phi-\sin\phi\cos\phi)\left[(\pi-\phi)^2-\sin^2\phi\right]\end{matrix}\right\}}$
Newman (1968) [33]	Capillary rise	$\cos\theta_D=\left(1-e^{-\sigma t/\mu M}\right)\cos\theta_e$ t is the time elapsed and M is a constant dependent on the tube surface condition

θ_D : Dynamic Contact Angle, θ_e : Equilibrium Contact Angle, Ca : Capillary Number ($=\frac{\mu u}{\sigma}$ where u is the velocity of triple-point, μ is the dynamic viscosity and σ is the surface tension)

As compared to their experimental counterparts, there are few numerical studies in the past to investigate the dynamic contact angle in capillary flows [34-38]. Schönfeld and Hardt [34] using the Volume-of-Fluid (VOF) method and implementation of an empirical correlation for the velocity-dependent contact angle, simulated the capillary rise. It was shown that the variation of the contact angle and the contact line friction are more accurately captured on finer meshes. Therefore, in order to eliminate the strong mesh dependency of the results, they proposed a macroscopic slip range near the triple-phase-point contact line and applied a body force to compensate the neglected friction. Deganello et al. [37] presented a level-set finite-volume numerical framework for modelling the dynamic contact angle in capillary flows in which they applied a force on the triple-point contact region, instead of prescribing a dynamic contact angle.

In this research, first, an experimental work was carried out to capture the liquid rise of water in cylindrical glass capillary tubes. The experimentally-observed images of meniscus during capillary rise was corrected accounting for optical distortion to obtain the corrected contact angle. The experimentally-obtained capillary height versus time were compared against original LWR model as well as the modified LWR using an empirical correlation for dynamic contact angle. Then, a computational fluid dynamic (CFD) model based on Volume of Fluid-Continuum Surface Force (VOF-CSF) method was developed that used an empirical correlation to predetermine the dynamic contact angle with the bulk liquid velocity. The numerical results were compared with the experimental data for capillary height and dynamic contact angles.

1.1.1 Optical distortion correction

Objects inside cylindrical tubes appear distorted as seen outside the tube due to the refraction of the light passing through different media. Such optical distortion may cause significant errors in geometrical measurements using optical observations of objects (e.g., liquid-gas interfaces, solid particles, gas bubbles) inside the tubes.

In microfluidics, it is common to require a visual observation of objects such as solid particles, gas bubbles and phase interfaces in cylindrical tubes. In such observation, an optical distortion arises from the refraction of light passing through different media of refractive indices at the curved test section of the tubes. In fact, the optical distortion may unknowingly exist in a wide variety of optical observations in microfluidics involving multi-phase flow in cylindrical glass tubes and geometrical measurements such as contact angle, liquid-gas interfaces (meniscus), and volume of particles. Although the

determination of the precise locations and shapes of the objects in the tubes demands analytical calculations of the light rays' refractions at the two concentric interfaces of the outer and inner tube walls, the efforts to eliminate the light refraction problem or reduce image distortion will prove to be valuable in such experiments involving precise geometrical measurements.

There are a number of studies that apply Laser Doppler Velocimeter (LDV, sometimes referred to as Laser-Doppler Anemometry, LDA) to correct the refraction of the laser beams at the wall interfaces [39-42]. In 1992, Lowe and Kutt [43] presented a set of equations that determined the coordinates of a point located inside a cylindrical tube that required an observation of the point inside the tube from two viewing directions. In order to validate the equations, they carried out an experiment using a single camera and a mirror oriented so that the direct and mirror images are simultaneously obtained. A precise pattern of small holes was drilled in a disk and tracer points were placed in the holes at various radial and azimuthal directions to set the known coordinates. The disk was then placed in a glass tube filled with water, with the plane of the disk perpendicular to the tube axis. Excellent experimental validation was achieved as the actual and calculated tracer positions inside the tube remained within 3% along the radius and ±1° in the angle.

Meniscus formation and dynamic and static contact angle measurements in cylindrical tubes have been found to be of much interest in microfluidics [24, 44, 45]. It is clear that these optical observations are always accompanied by the optical distortion and the original photographs from these observations require an appropriate correction before further analysis. Because of simplicity and convenience, the contact angle has been often

measured assuming a spherical shape of an ideal meniscus which sometimes leads to inaccurate measurements. So far, to the best knowledge of the authors, there is not a comprehensive study to specifically address the effect of the light refraction on the meniscus profile and contact angles in cylindrical tubes.

In this study, an analytical method using a point-by-point correction of the optical distortion was developed. For an experimental validation, the method was used to correct the apparent profiles of the water-air interfaces (menisci) in cylindrical glass tubes with different tube diameters and wall thicknesses. Then, the corrected meniscus profiles were used to calculate the corrected static contact angles.

1.2 TWO-PHASE FLOWS IN A TUBE

Simultaneous flow of gas and liquid (two-phase) in a channel (e.g. tube) is inherently a complicated phenomenon which is controlled by different competing forces such as surface tension, shear stress, gravity, momentum and inertia. The continuous movement of phase interfaces, makes the already complex two-phase flow even more complicated introducing a destabilizing effect into the flows and resulting in changes of temporal and spatial distributions of the phases. Due to the complex nature of the gas and liquid mixture flow, the two-phase flow is often classified by unique flow pattern and presented in a flow-pattern (sometime refers to "flow-regime") map. Therefore, the correlations for heat transfer and pressure drop for the two-phase flows should be flow regime-specific for accurate prediction of two-phase flow characteristics.

1.2.1 Two-phase flow regimes

Among several flow regime maps available in literature, Baker's [46], Mandhane's [47], and Taitel-Dukler's [48] maps are recognized as the most cited for horizontal adiabatic gas-liquid flow. For phase change (condensing or boiling) two-phase flow, the matter is further complicated by a continuous change in vapor and liquid fractions, which is accompanied by a similar change in the spatial distributions of the phases.

Although interpretation of two-phase flow patterns using photo images is usually subjective and there is no such a unique and accurate quantitative procedure to classify the flow patterns [49], the following descriptions are widely accepted classifications of the classification of gas-liquid two-phase flows in a horizontal tube:

(a) Stratified flow: Two phases are completely separated from each other by a continuous interface. The gas flows along the upper region of the horizontal tube whereas the liquid travels along the bottom with relatively smooth interface. Gravity plays a dominant role in this type of flow which occurs at relatively low velocities. This flow is sometimes referred to as "stratified smooth" flow pattern. It is seen in Fig. 1.2-1 that the stratified flow has the simplest configuration among all of the horizontal flow patterns.

(b) Wavy flow: By increasing the gas velocity in a stratified flow, the shear forces of the gas flow over the liquid cause ripples on the interface, resulting in a formation of waves. The waves climb up the sides of the tube, but usually do not touch the top side of the tube wall and the liquid layer at the bottom of the channel starts to stretch thin [Fig. 1(b)]. This flow is sometime referred to as "stratified wavy" flow pattern.

(c) Plug flow: Elongated gas bubbles (gas plugs) in bullet-shaped and liquid plugs appear alternatively on the top of the tube [Fig. 1(c)]. The diameters of the gas plugs are smaller than the tube dimeter which allows for a continuous liquid phase to appear on the bottom of the tube. This flow is sometimes referred to as "elongated bubble" flow pattern [50].

(d) Slug flow: This flow is recognized with a sequence of liquid slugs, each followed by an elongate gas bubble over a thin layer of liquid film. These liquid slugs are then transported at higher velocity of the gas than that of the liquid [see Fig. 1(d)]. Unlike the plug flow, in which the elongated bubbles are transported by the liquid phase, in the slug flow, the liquid slugs are carried by faster moving gas flow. Slug

flow regime is highly undesirable in practical application. The fast moving liquid slugs are usually associated with sudden pressure pulses and severe pressure oscillations that can cause damage to downstream components [51].

(e) Annular flow: The liquid forms a continuous film around the perimeter of the tube wall and gas flows as a central core and entrains small droplets of liquid dispersed in the form of mist [Fig. 1(e)]. Small bubbles of gas may also be entrained in the liquid film. This flow is momentum-dominant and occurs at relatively high gas velocities which is associated with relatively high heat transfer coefficient in condensing or boiling flows.

(f) Bubbly flow: At very high liquid flow rates, gas bubbles are dispersed in a continuous liquid phase [Fig. 1(f)]. The bubbles are small in comparison with the tube diameter and tend to rise to the upper region of the tube due to buoyancy force. However, when the liquid velocity is high enough, shear forces are dominant and uniform distribution of bubbles occur in the tube. This flow regime is really a separate category. (a) to (e) can be obtained by simply increasing J_G at the same J_L, which is just the opposite of how the bubbly flow is obtained.

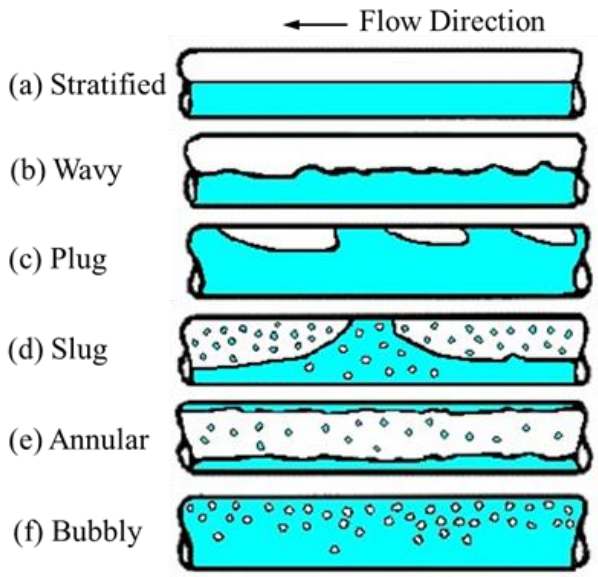

Figure 1.2-1 Representative schematic of horizontal two-phase flow patterns

Due to complexity, theoretical solutions of in-tube two-phase flow are either impossible or based on many assumptions to make them simpler. Therefore, experimental data have been mostly used to produce flow pattern maps. The most common approach to study gas-liquid flow patterns is to visualize the two-phase flows through a transparent flow channel.

Because of relatively high cost and practical limitation associated with experiment in studying two-phase flow characteristics, Computational Fluid Dynamic (CFD) simulation has been growingly used to simulate multi-phase flows [52-54]. The majority of CFD studies of two-phase flow has typically been conducted using commercial software such as ANSYS Fluent and CFX [53, 54]. However, in recent years, OpenFOAM (Open-source Field Operation AND Manipulation) has gained traction as an alternative to the commercial software because of no license cost, automatic parallelization of applications, code customization according to problems and wide range of solvers available [55]. There are few previous studies that used OpenFOAM to simulate gas-liquid flows in a tube [56-

59].

1.2.2 Two-phase flows under reduced gravity

The realization of space colonization may not be far from reality with the growing interests in the space settlement on Moon and Mars. However, this ambitious goal presents a big challenge to scientists who lack a comprehensive knowledge of how reduced gravity influences the two-phase system design and operation. Refrigeration and power systems involving two-phase (gas-liquid mixture) flows are widely used for in the solar colonies such as Moon and Mars under reduced gravities [60]. Due to the large density difference between the gas and liquid phases, the flow hydrodynamic behavior is significantly influenced by gravitational force. Therefore, reliable design of space-based two-phase systems requires a thorough realization and accurate prediction of two-phase flow characteristics under various gravity environments of the solar colonies.

Over the past decades, research on gas-liquid flow for space applications has primarily focused on microgravity environment. Heppner et al. [61] reported for the first time that two-phase hydrodynamics at reduced gravities differs from those at normal gravity. Experimental results of flow patterns and pressure drop for microgravity were achieved aboard in a NASA KC-135 aircraft flying parabolic trajectories. Larger pressure drops were reported for the microgravity compared to those at normal gravity. Later, Dukler et al. [62] under the sponsorship of NASA Lewis Research Center, performed drop tower tests and parabolic flights on a Learjet to captured various air-water flow patterns of bubbly, slug and annular flow at microgravity. Colin et al. [63] reported gas-liquid flow patterns, void fraction, and pressure gradient of bubbly and slug flows at microgravity

during parabolic flights. Zhao and Rezkallah [64] observed bubble, slug, and annular air-water flows at microgravity during a series of parabolic flights.

Zhao and Rezkallah [65] presented experimental results of the pressure drop of vertical upward air-water flows under microgravity during parabolic flights. Since their data was mainly inertia-dominated, the frictional pressure drop values at microgravity were in the same order of magnitude of those at normal gravity. Bousman et al. [66] carried out numerous experiments on parabolic flights and presented a void fraction-based transition model to predict microgravity flow patterns. Choi et al. [67] conducted an experiment using air-water flows in microgravity using parabolic flights. The experimental results of flow patterns, void fraction, and pressure drops, for normal (g), hyper ($2g$), and microgravity were compared with previous empirical models of the researchers.

There are very few experimental works on gas-liquid flow under Moon's (~0.17 g_o) and Mars' (~0.38 g_o) reported in literature. Hamm and Best [68] conducted a visual observation of two-phase flows in a horizontal tube on parabolic flights for Moon's and Mars's gravities. Bubbly, slug, plug, annular, and stratified flows were observed, and flow pattern maps under reduced gravity were generated. Balasubramaniam et al. [69] presented flow pattern maps of water–glycerin, air–water, and air–water-Zonyl 0.5% under Moon's gravity from their experimental data on parabolic flights. Hulbert et al. [70] also reported two-phase flow patterns under the Moon's and Mars' gravities.

Ground-based experiments are inherently limited to the earth's gravity and therefore have to compromise experimental conditions and at best, use tilted orientations to manipulate the vertical component of gravitation force and mimic the reduced gravities

on Moon and Mars. More accurate experiments can employ elaborated facilities such as drop tower and parabolic flights which are often inaccessible due to cost, size and weight constraints. Not to mention, reduced-gravity experiments last only a short period of time (~10 sec.) and cannot achieve a steady-state condition. Not only to overcome the aforementioned challenges but also to gain much deeper insights into the fundamental physics of complex two-phase flows, a computational simulation has been recently used to study two-phase flows at reduced gravity. Numerical investigations are very suitable to gain an insight into the complex hydrodynamics of in-tube gas-liquid flows. Thus, numerical simulations have been increasingly used recently to study two-phase flow behavior at reduced gravity.

Clarke and Rezkallah [71] used a two-dimensional CFD (Computational Fluid Dynamics) model to study the bubble drift velocity in a vertical two-phase flow under microgravity. Gabriel [72] investigated the flow field in a slug flow under normal and microgravity conditions using a two-dimensional axisymmetric CFD model. Yang [73] numerically studied the interfacial shapes of gas-liquid flows at microgravity and compared with the experimental images of air-water interface obtained from a free-fall drop test. Liu et al. [74] performed a numerical simulation to study the horizontal gas-liquid flow regimes and void fraction for four different gravities. The researchers attributed the flow pattern transition to the coalescence of bubbles/plugs and gravity-driven drainage of the liquid film formed by the coalescing bubbles/plugs induced by increasing the gravity level.

While technical advances in computational simulation has been made for the past decades, numerical studies on two-phase flows under different gravities are very limited compared with the experimental counterparts and the detailed impacts of gravity on in-tube

two-phase flows have remained vastly unknown. As a result, two-phase flow research still suffers from a lack of detail understanding and a reliable prediction of complex two-phase flow and heat transfer. The difficulties arise from the fact that two-phase flow is inherently a complex, unsteady process involving interfacial interactions and flow instabilities.

1.3 HEAT TRANSFER ENHANCEMENT

1.3.1 Non-condensing two-phase flows

Heat transfer enhancement has been always a constant endeavor of scientists and engineers aiming to reduce energy consumptions for maximum efficiency. For liquid-phase flows, the addition of a secondary different phase such as solid particles or gas bubbles has been shown to be very effective in enhancing the convective heat transfer due to the increased flow mixing and boundary layer disturbance of the multi-phase flows.

Hassanipour and Lage [75] used a liquid flow laden with phase-change solid particles in a mini-channel for a moderate (20% increase) heat transfer enhancement, as compared to the liquid-only (without particles) flow. The enhancement was attributed to the combination of a flow mixing induced by the solid particles and a phase-change effect. Kiaee and Lage [76] numerically analyzed a liquid flow loaded with a spherical solid particle in a channel to study the role of the particle sweeping the wall boundary layers on the convective heat transfer and reported an increase of 12% in the average Nusselt number. Kiaee et al. [77], using a numerical simulation showed that the presence of solid particles in a liquid flow led to enhancements by 27% and 10% in the average Nusselt number and average heat flux, respectively.

For gas-liquid flows without phase change (i.e. non-boiling/non-condensing), a slug flow can significantly increase the convective heat transfer compared to the conventional liquid flow. A gas-liquid flow in a channel may exist in various flow regimes depending on the velocities of the phases and flow orientation. The slug flow (aka bubble-train flow, Taylor flow, and intermittent flow) is an important flow regime that is characterized by the

appearance of bullet-shape bubbles, separated by liquid slugs. Prothero and Burton [76] from an experimental study found that the heat transfer of air–water slug flows in capillaries were twice of that of a liquid-only flow. Oliver and Hoon [78] reported the two and half times heat transfer enhancement for a gas-liquid slug flow in a channel of diameter 6.4 mm compared to that of a liquid-only flow.

Lakehal et al. [79] performed numerical simulations of air-water flow in a miniature tube of diameter 1 mm and showed that the air-water slug flow increases the convection heat transfer by four times more than that of a liquid-only flow. Gupta et al. [80] numerically simulated air-water slug flows in a channel of diameter 0.5 mm and found that the Nusselt numbers of the slug flow were two and a half times higher than those of liquid-only flow for both constant wall heat flux and constant wall temperature conditions. Mehdizadeh et al. [81] using the VOF method simulated air-water slug flows in a mini-channel of 1.5 mm diameter under a constant wall heat flux and found that the Nusselt number of the slug flow can be 610% higher than that of single-phase flow. They identified two main reasons contributing to the enhanced heat transfer of the slug flow [82]; first, the secondary flow recirculation in the liquid slugs to promote the radial heat transfer; second, higher local velocity of the liquid slugs due to the reduced liquid fraction.

It has been shown in literature that, two immiscible liquids enhance the convective heat transfer in two-phase flows. Gat et al. [83] in an experimental study showed that an induced liquid-liquid phase separation can enhance the convective heat transfer up to 130% as compared to that of a single-phase flow. Xing et al. [84] performed an experimental study in a microchannel and showed that when heated above a critical temperature, the

mixture separated into distinct immiscible liquid phases resulting in an enhancement by 250% in the convective heat transfer coefficient as compared to that of a single liquid-phase flow. Ullmann [85] conducted an experimental study of laminar flows in a small tube diameter of 2 mm and found that the induced liquid-liquid phase separation can substantially enhance the convective heat transfer up to 150%. The heat transfer enhancement was attributed to the increased fluid mixing and the lateral movement of the separating droplets.

In condensing vapor-liquid flows, the heat transfer inherently degrades toward the condenser outlet where more condensate is accumulated, and thus more condenser surface is covered by a thick condensate layer, resulting in a large thermal resistance. To mitigate this problem, Chen et al.[86] utilized a gas-liquid phase separation using a porous tube to promote a thin-film condensation in the condenser. The phase separation is achieved by capillary force at the liquid-vapor interfaces (aka meniscus) formed in the pores of the porous tube. The porous tube blocks the gas bubbles from entering the porous tube, but allows the liquid to freely flow through the porous tube. Consequently, the confined bubbles in the annular gap between the condenser wall and porous tube, which is elongated along the condenser wall, promotes the thin film condensation in the condenser. Chen et al. [86] observed such a phase separation in an adiabatic (no heat transfer) horizontal air-water flow experiment. Also, Chen et al. [87] from the aforementioned research group using a numerical simulation, investigated the hydrodynamics of an adiabatic, vertical upflow, air-water slug flow with the presence of a porous-tube-insert. The numerical results showed a favorable phase separation and ultra-thin liquid film near the tube wall leading

to condensation enhancement. Moreover, secondary liquid circulations in the radial direction were observed over the entire tube length.

In this work, a convective heat transfer enhancement using non-condensing gas-liquid flows and a capillary-assisted phase separation was numerically investigated. Air-water slug flows in a vertical upward flow arrangement was used to study the hydrodynamics of the slug flows and fundamental mechanisms of the convective heat transfer enhancement by the phase separation using a porous-tube-insert. Two designs of the porous tube were considered: a closed frontal end to prevent bubbles from entering the porous tube; and an open front end to allow bubbles to enter and flow through the porous tube. A set of parametric simulations was systematically carried out for an optimization of the annular gap dimension (or porous tube diameter) for the maximum heat transfer

1.3.2 Condensing flows

Condensation is widely used in various applications such as refrigeration and air-conditioning systems, where determination of operating limits for safety conditions is a crucial task and requires the thorough understanding of the complicated condensation mechanism. Due to the limited energy resources and also the environmental issues, designing an efficient condenser have been the subject of significant effort for engineers to reduce the refrigerant charge, heat exchanger volume, and manufacturing cost material saving.

Although the heat transfer coefficient in dropwise condensation is more than ten times larger than the filmwise condensation, the filmwise condensation is difficult to be

maintained in practical condensers. Thus, a hot research area is to investigate how to enhance the filmwise condensation heat transfer. Nusselt [88] was the pioneer to present a theoretical model for the film condensation, where the condensation heat transfer sharply decreases with increasing condensate film thickness or thermal resistance. As such, the reduction of the film thickness has been identified as the governing principle to enhance the condensation heat transfer.

Flow condensation in a tube typically commences with annular flow with the formation of a thin liquid film about the inner tube wall. With the flow development, the intermittent flow patterns (slug, plug flows) thicken the liquid film on the tube wall, deteriorating the condensation heat transfer. Continued axial condensation leads to the formation of dispersed bubbly flow and eventually the flow is converted to pure liquid. In horizontal flows for low mass flux, however, further condensation in the axial direction is accompanied by stratification of liquid toward the bottom of the inner wall resulting in a relatively thick liquid film towards the bottom, compared to a very thin film or no film at the top.

Over the past decades, various passive techniques for flow condensation enhancement have been proposed, such as micro-fin tubes, groove tubes, inserts, etc. [89-91]. However, most of them were mainly focused on extending the heat transfer surface area, intensifying the flow turbulence, destroying the growth of boundary layers and very few of them focused on the film thickness reduction.

Chen et al. [86, 92, 93] proposed a porous-tube insert inside the condenser tube to reduce the condensate film thickness using adiabatic air-water flow experiments in both

horizontal [86, 93] and vertical upward flow [92]. They demonstrated the phase separation due to the surface tension (capillary) action within the pores of the porous tube where the gas bubble flows in the annular gap and only liquid flows into the porous tube. The numerical studies by Chen et al. [87] and Sun [94] from the aforementioned research group also showed that the liquid film thickness can be decreased up to 1/6~1/3 of those in the bare tube for a vertical upward slug flow using a porous-tube insert.

Xie et al. [95] experimentally investigated flow condensation of R123 in a horizontal tube with a porous-tube insert formed by packaging two layers of mesh screen. They focused on stratified and annular flow regimes and shows that the condensation enhanced in the range of 1.18~2.12 using the porous-tube insert. Xie et al. [96] also carried out a set of experiments to study flow condensation enhancement of R245fa using a porous-tube insert covering different mass fluxes, vapor qualities and flow orientations. The porous tube was made by sintering copper powders at high temperature. The reported heat transfer enhancement factor had a range of 1.25~1.85, which were largest for vertical upflow and smallest for horizontal flow.

Although numerical simulations using computational fluid dynamics (CFD) are very suitable to gain an insight into the complex behavior of flow condensation, such studies are very limited compared with their experimental counterparts and research in flow condensation still suffers from a lack of detail understanding to achieve a reliable prediction [97]. This paper presents the numerical simulation results of flow condensation in a vertical upward slug flow and discusses the fundamental mechanism of the flow condensation enhancement using a porous-tube insert (PTI). As such, first, the

computational formulation for phase-change simulation is presented. Next, a two-dimensional axis-symmetric CFD model is developed to investigate flow condensation of isobutene with and without the presence of a porous-tube insert. A vertical upward slug flow is considered as it can be reasonably simplified as a 2-D axisymmetric problem. The condensation heat transfer enhancement by using a porous-tube insert is discussed. Finally, a set of parametric study is performed to study the effect of void fraction and gap dimension on flow condensation enhancement using a porous-tube insert.

2 CHAPTER 2: CAPILLARY FLOW

This chapter discusses the hydrodynamic characteristics of capillary-drive flows in a tube with a small diameter and mainly focuses on the dynamic rise of liquid through a cylindrical tube. This is a classical benchmark problem, which provide a useful insight into the physics of the interfacial phenomena of a two-phase flow system. As such, an experimental investigation into meniscus formation during capillary rise was performed, specifically focusing on dynamic contact angle behavior. Close-up photographs of the meniscus profile were captured at various rise heights and the contact angle (CA) was found through an optical distortion correction to address the problem of image distortion due to light refraction. A computational fluid dynamics (CFD) model based on the volume of fluid-continuum surface force (VOF-CSF) method was also developed to simulate the capillary rise accounting for dynamic contact angle. The numerical model used an empirical correlation for the computation of instantaneous contact angle in each time step. It was shown that by using the dynamic contact angle instead of a constant (equilibrium) angle, the numerical results of capillary heights were significantly improved and match satisfactory with the experimental data. In addition, it was shown that the typical assumption of constant contact angle may predict an unphysical oscillation during capillary rise, which can be eliminated by dynamic contact angle.

2.1 CAPILLARY RISE IN A TUBE

2.1.1 Experimental approach

Figures 2.1-1 shows the schematic of the experimental set-up used to study the capillary rise of water in a capillary tube. In order to capture the capillary height versus

time and also get a clear picture of the meniscus during the liquid rise, an optical tensiometer (Biolin Scentific, Theta Optical Tensiometer) was used. The tensiometer includes a high-speed camera (Firewire digital camera with zoom), which could successfully capture the large field-of-view (FOV) images of the rise height versus time data as the liquid penetrated the capillary tube and also provides a close-up view (small FOV) of the meniscus at various points along the length of the tube. An LED based background light source was used on the back side of the capillary tube to enhance the brightness of the large field-of-view (FOV), whereas another light source was used from the front in order to provide a sharp contrast aiming to improve the observation of the meniscus surface. Therefore, this set-up allowed for clear visualization of the meniscus over the whole length of fluid travel.

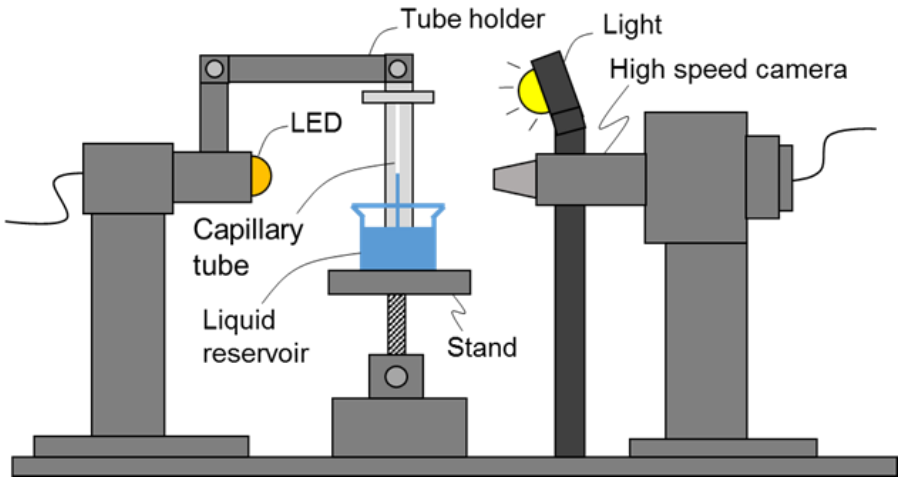

Figure 2.1-1 The schematic of the experimental set-up used to capture capillary rise

Two capillary tubes having different inner diameters of 1.25 ± 0.15 mm and 1.67 ± 0.15 mm were used in this study. For cleaning purpose, the capillary tube was first rinsed using distilled water, alcohol, and acetone. Next, the tubes were dried using compressed Nitrogen gas and then placed in a plasma vacuum chamber (Diener Electronic plasma

system) for three minutes to ensure full removal of impurities and contaminants from the tube surface. The tube was then attached to the tube stand with a removable adhesive tape, such that it was oriented vertically in front of the camera setup. A 50 mL beaker filled with distilled water was then placed on a platform under the tube. By turning a knob on the tube stand, the beaker was raised up to the point where the stationary capillary tube tip just broke the surface of the fluid. As the fluid launched up the capillary tube, the camera recorded the capillary rise data. In addition, the tensiometer provides with measurement of the surface tension of the distilled water using pendant droplet method. The surface tension of σ=71.2 mN/m was measured for the distilled water used in the experiment.

2.1.2 Computational model for two-phase flow

The volume of fluid (VOF) method was employed to model a transient two-phase flow [98]. In this method, each phase is treated as an incompressible immiscible fluid using phase fraction (α) that is a scalar variable for the phase fraction of one phase in a computational cell. It is also assumed that each phase is a Newtonian fluid with constant density and viscosity. The conservations of mass and momentum for a two-phase mixture are respectively given by

$$\frac{\partial}{\partial t}(\rho)+\nabla\cdot(\rho\boldsymbol{u})=0\,, \tag{2-1}$$

$$\frac{\partial}{\partial t}(\rho\boldsymbol{u})+\nabla\cdot(\rho\boldsymbol{u}\boldsymbol{u})=-\nabla p+\nabla\cdot(\mu\nabla\boldsymbol{u})+\rho\boldsymbol{g}+\boldsymbol{F}_{\sigma}\ , \tag{2-2}$$

where the phase fraction (α) within a cell and accordingly the motion of phase interface is calculated by an additional transport equation:

$$\frac{\partial}{\partial t}(\alpha)+\nabla\cdot(\boldsymbol{u}\alpha)+\nabla\cdot\left[\boldsymbol{u}_{r}\alpha(1-\alpha)\right]=0\ . \tag{2-3}$$

In the above equations, $\boldsymbol{u}$ is velocity vector and p is pressure. ρ is the effective density and μ is the effective viscosity of the fluids which are computed by the average property values of the gas and liquid phases, weighted by their respective phase fractions [i.e. $\rho = \alpha_L \rho_L + (1-\alpha_L)\rho_G$]. According to the continuum surface force (CSF) model proposed by Brackbill et al. [99], the surface tension force can be expressed as a volumetric force by the divergence theorem. This force is considered in the momentum equation [Eq. (2-2)] by the source vector $\boldsymbol{F_\sigma}$ that is only applied to the cells containing a gas-liquid interface ($0< \alpha <1$) and is given by

$$\boldsymbol{F}_\sigma = \sigma \kappa \nabla \alpha , \tag{2-4}$$

where σ is surface tension and κ is interface curvature defined by $\kappa = \nabla \cdot \left(\nabla \alpha / |\nabla \alpha| \right)$. In order to mitigate the numerical smearing of the interface, an extra artificial compression term is incorporated in the phase fraction equation [third term in Eq. (2-3)] to sharpen the interface [100]. The compression term applies only in an interface region and includes a compression velocity $\boldsymbol{u_r}$ that is available only in the normal direction to the interface. The $\boldsymbol{u_r}$ is based on the velocity magnitude in the transition region of the thin interface and is determined with a maximum velocity ($u_{\max}$) and an adjustable coefficient (K_c) defining the compression factor and an interface normal and is given by

$$\boldsymbol{u}_r = K_c U_{\max} \frac{\nabla \alpha_k}{|\nabla \alpha_k|} , \tag{2-5}$$

where the adjustable coefficient (K_c) can vary between zero and four. In this study, K_c is set to unity as suggested in literature [101]. The VOF model including the additional artificial compression term (VOF-CSF) was validated with standard two-phase benchmark problems in literature [101-103].

A typical issue in simulating multiphase flows is the generation of non-physical flow at the interface namely “spurious” or “parasitic” current [104-106]. The source of the spurious current has been identified as an imbalance between the discrete surface tension force and the pressure gradient term that is originated from the inaccurate calculation of interface curvature. The issue of spurious current is essentially important in surface-tension-dominated flows in capillary channels (microfluidic systems) and are commonly small in inertia-dominated flows [107, 108]. A method to suppress the spurious current is using the Laplacian filter proposed by Lafaurie et al. [104] to smooth the interface and providing a less steep gradient of phase fraction. The Laplacian filter, which is used in this study, transforms the initially calculated phase fraction (α) into a smoothed one ($\tilde{\alpha}$) by a linear interpolation of the volume fraction in each cell with the volume fractions of its neighbor cells:

$$\tilde{\alpha}_p = \frac{\sum_{f=1}^{n} \alpha_f S_f}{\sum_{f=1}^{n} S_f}, \tag{2-6}$$

where p and f are cell index and surface index , respectively. α_f is linearly-interpolated volume fraction at the center of the cell face, and S_f is cell surface area. The implementation of the Laplacian smoother has been validated with the benchmark problems in previous studies in literature [101, 109].

The governing equations [Eqs. (2-1)-(2-3)] are discretized and numerically solved using OpenFOAM. In order to calculate the pressure-velocity coupling, a PIMPLE algorithm was implemented that combines the Pressure-Implicit Split-Operator (PISO) and the Semi-Implicit Method for Pressure-Linked Equations (SIMPLE) algorithm. The PIMPLE algorithm employs two corrector loops (inner and outer) and interface

compression to yield a sharp interface. All equations are solved in the outer loop whereas only the continuity equation is solved in the inner loop.

2.1.3 Results

Figure 2.1-2 shows a two-dimensional (2-D) axisymmetric domain, which used for the simulation of capillary rise. The model consists of a capillary tube and a liquid reservoir, where the atmospheric pressure was applied on top of the reservoir and capillary tube. Also, the non-slip boundary condition was enforced on the tube wall. As shown in Fig. 2.1-2, the relative coarse mesh is used in the reservoir whereas the finer mesh was incorporated in the capillary tube. In addition, the mesh was further refined towards the tube wall to accurately capture the contact angle.

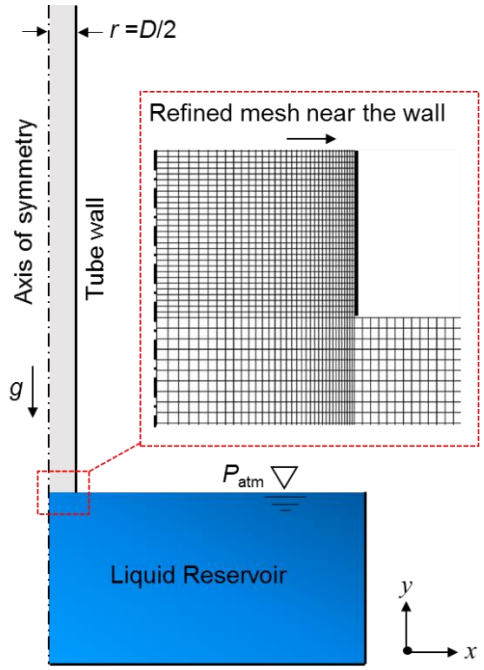

Figure 2.1-2 Model geometry and computational grid system to study the capillary rise in a tube

Table 2.1-1 lists the properties of working fluids as well as the system dimension that were used in the simulation. The equilibrium contact angle between water and borosilicate glass was set to 44° as the, which was directly measured in the experiment. For the simulation, the reservoir and capillary tube were initially filled with water and air, respectively. The Courant number ($C=u\Delta t/\Delta x$) was set to a limit of 0.3 to help the convergence of the solution, where u is the velocity, Δt is the time step, and Δx is the axial spacing of a cell of the computational model. Note that the simulations were performed under an isothermal condition. Therefore, no temperature boundary condition is applied. In order to study the complex hydrodynamics of capillary flow, a transient simulation with a time step of 10^{-5} s was performed. Gravitational field was also applied in the vertical opposite to the flow direction.

Table 2.1-1 Thermophysical properties of working fluids and system dimension

Parameter	Value
Density of air, ρ_G [kg/m^3]	1
Density of water, ρ_L [kg/m^3]	1000
Kinematic viscosity of air, v_G [m^2/s]	1.480×10^{-5}
Kinematic viscosity of water, v_L [m^2/s]	10^{-6}
Surface tension, σ [N/m]	0.071
Tube diameter, D [mm]	1.25, and 1.67
Tube material	Borosilicate glass
Tube length [mm]	40
Equilibrium (static) contact angle, θ_e	44

For the grid dependency analysis, the numerical results for final equilibrium height (h_{eq}) was computed and compared with the theoretical result calculated using the Young–Laplace equation that is given by

$$h_{eq} = \frac{4\sigma \cos\theta_{eq}}{\rho_L g D_i}, \tag{2-7}$$

where σ is surface tension, θ_{eq} is the equilibrium contact angle, ρ_L is the liquid density, and D_i is the tube inner diameter. A mesh dependency analysis was performed in which the mesh count was increased until the computed value of the equilibrium height (h_{eq}) was within less than 1% of the previous mesh case. Figure 2.1-3 presents the effect of mesh number on the computational results for the equilibrium capillary height. It was found that 88,108 mesh for tube with D=1.67 mm and 84,334 mesh for tube with D=1.25 mm are sufficient to ensure a reasonable accuracy for the capillary height calculation [less than 0.5% error with Eq. (2-7)] and by further increase in mesh number, the change in h_{eq} was less than 1% . Therefore, the 88,108 cells for tube with D=1.67mm and 84,334 cells for tube with D=1.25mm was selected for the entire simulations in this study.

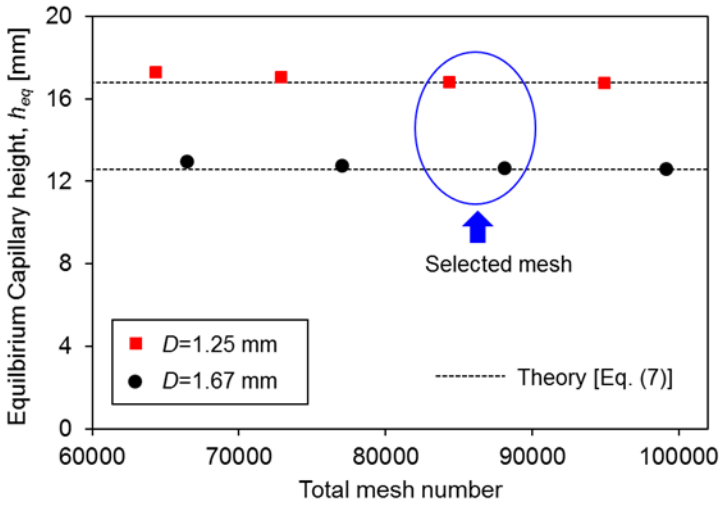

Figure 2.1-3 Effect of mesh number on the computational results for the equilibrium capillary height

For the modeling of dynamic contact angle, an in-house algorithm was implemented as a contact angle boundary condition as illustrated in Fig. 2.1-4. The CFD model allows to implement an implicit function for dynamic contact angle. The method

uses an empirical correlation of Joos's model [21] for the calculation of contact angle in each time step. The correlation is given by

$$\cos(\theta_d) = \cos(\theta_e) - 2\left[1+\cos(\theta_e)\right]Ca^{1/2}, \tag{2-8}$$

where θ_d and θ_e are the dynamic and equilibrium contact angles, respectively, and Ca is the capillary number that is defined by

$$Ca = \frac{\mu u}{\sigma}, \tag{2-9}$$

where μ is the liquid viscosity, σ is the surface tension, and u is the triple-phase-point velocity. Due to the imposed no-slip boundary condition on the tube wall, instead of using the actual triple-point velocity, the proposed numerical method uses the averaged liquid axial velocity in the entire liquid column to approximate the triple-phase contact line velocity. The computed averaged velocity in the current time step, was used in Eq. (2-8) to calculate the instantaneous contact angle in the next time step (Fig. 2.1-4).

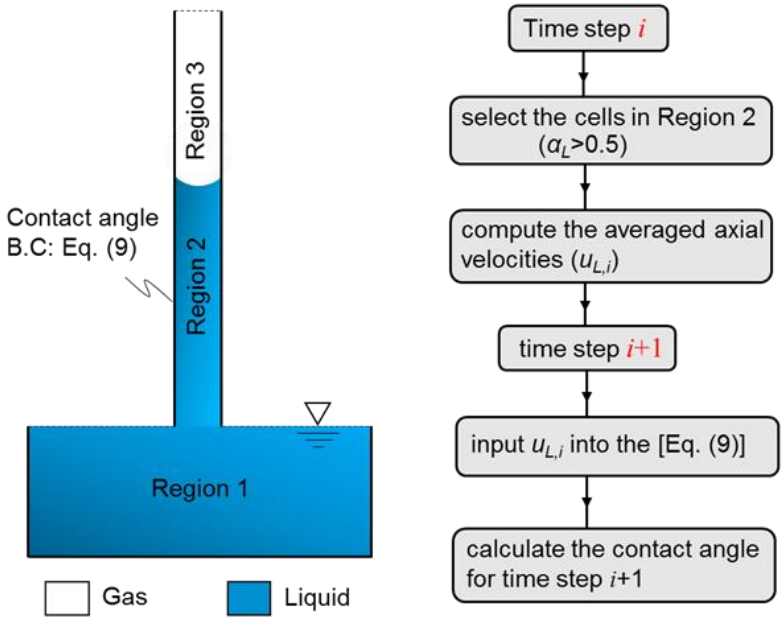

Figure 2.1-4 The algorithm used for the calculation of dynamic contact angle in the CFD model

Experimental results

Figure 2.1-5(a) shows the selected images of the experimentally-observed air-water meniscus during capillary rise of water in glass cylindrical tubes of the two different diameters. It is seen that at the initial penetration of liquid in the capillary tube the meniscus is more flat shape with an instantaneous high contact angle. As the liquid rises, the meniscus becomes more concave shape with a lower contact angle approaching to the equilibrium condition. Figure 2.1-5(b) shows the distortion correction of the observed meniscus shape and corrected contact angle for the capillary tube with D_i=1.25mm at t=1s following the optical distortion correction method described in Section 2.2. It is seen that the apparent (observed) contact angle of θ_a=49.35º is reduced to θ_c=44.26º after optical distortion correction.

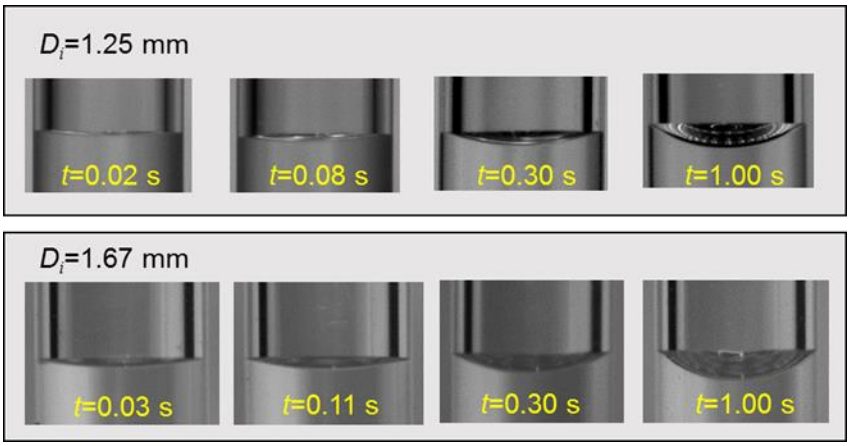

(a)

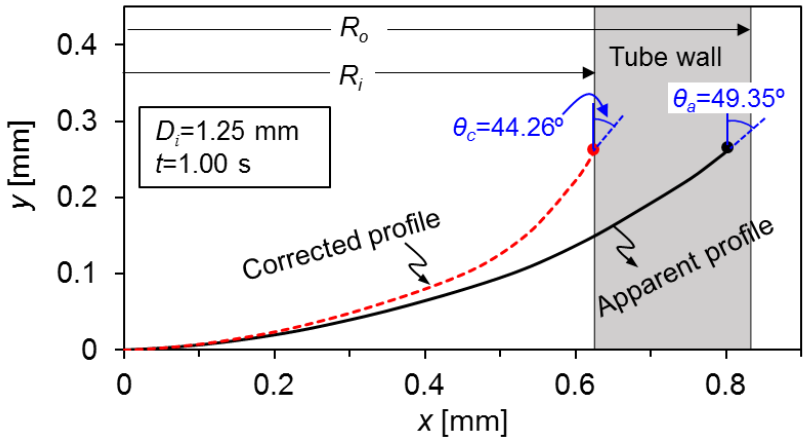

(b)

Figure 2.1-5 (a) Experimentally-observed variation of the meniscus shape during capillary rise of water in the capillary tubes with two different diameters; and (b) the correction of the apparent (observed) meniscus profile and contact angle for the capillary tube with D_i=1.25mm at t=1s following the optical distortion correction method described in Section 2.2

Figure 2.1-6 shows the variation of all of the apparent (observed) θ_a and corrected contact angles θ_c for both capillary tubes with capillary number Ca. The predicted contact angles by Joos's model [Eq. (2-8)] are also shown for the comparison. It is shown that, generally, the contact angle is reduced during the capillary rise as a result of reduced capillary number (or velocity). From the comparison of the predicted values and the experimental data, it is also seen the Joos's model [Eq. (2-8)] slightly underestimates the experimental results of dynamic contact angles, especially at the initial moment of the capillary rise.

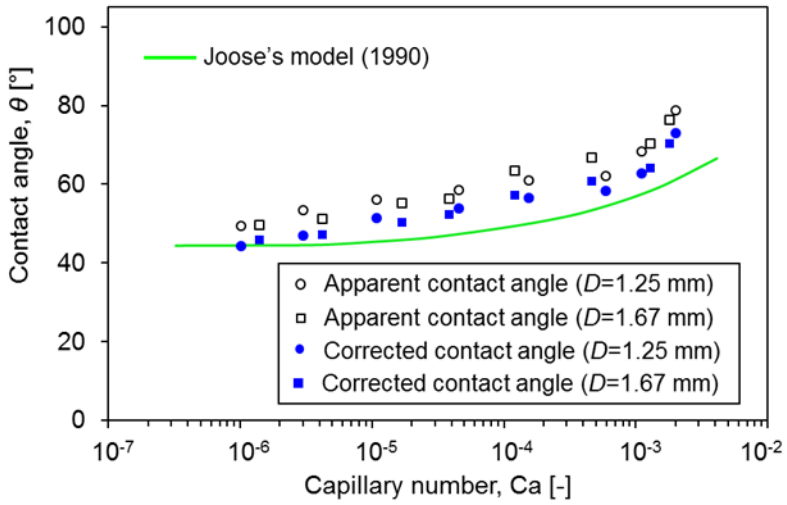

Figure 2.1-6 Comparison of the experimentally-observed (apparent, θ_a) and the corrected θ_a contact angles with Joos's empirical model [21]

Figures 2.1-7(a-b) show a comparison of the experimental result of capillary rise (h) with the theoretical results from the LWR [LWR, Eq. (1-1)] and the modified LWR by replacing the constant (equilibrium) contact angle (θ_e) with dynamic contact angle (θ_d) using Joos's model [Eq. (2-8)]. The governing equation of capillary flow [e.g. Eq. (1-1)] is a second order nonlinear ordinary differential equation (ODE) with no analytical solution, and thus, the equation was solved numerically. Also, in order to remove the singularity at t=0, the initial small non-zero values for $h(0)$ and $u(0)$ was assumed as the initial conditions.

Fig. 2.1-7(a) shows the theoretical results of capillary height versus time together with the experimental data for the smaller capillary tube (D_i=1.25 mm). It is seen that the original LWR equation with constant contact angle (θ_e) (dashed line) predicts an overshoot (oscillation) at the very initial moments (t<0.3 s) while no oscillation was observed in the experiment. This is due to the overestimation of surface tension force in original LWR equation as a result of the constant contact angle. However, the modified LWR equation with the dynamic contact angle (θ_d) (solid line) eliminates the unphysical oscillation and

the transient behavior of the capillary rise approaches to the experimental data. It is also seen that after relatively long time (t>0.5s), the predicted capillary heights from both LWR and the modified LWR converges to each other and the predicted final equilibrium heights match well with the experimental data.

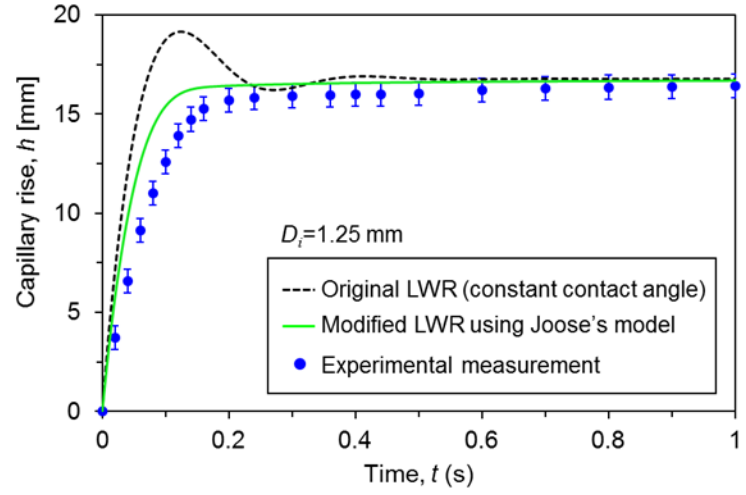

(a)

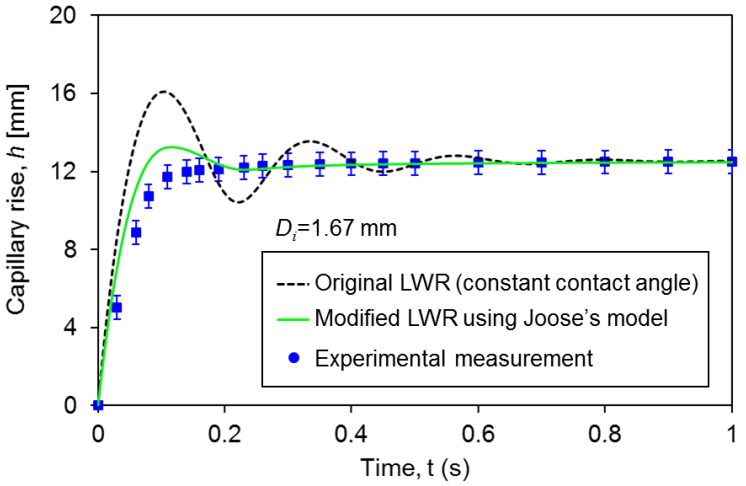

(b)

Figure 2.1-7 Experimental results of capillary height versus time and the comparison with the predicted results obtained by theoretical LWR equation and the modified LWR using Joos's model [21] for the capillary tube with (a) D_i=1.25 mm; and (b) D_i=1.67 mm

It is also shown in from Fig. 2.1-7(b) for the larger capillary tube (D_i=1.67mm) that the LWR model predicts a stronger oscillation as compared to that for the smaller tube diameter (D_i=1.25mm). This is because of the larger inertia caused by the overestimated surface tension force in a larger tube diameter. Again, no oscillation was captured from the experimental observation. However, by applying the dynamic contact angle of Joos's model, the oscillation was significantly damped and a very small overshoot is seen at the initial moment. Overall, the modified LWR shows a reasonable agreement when compared to the experimental data for capillary height versus time.

Numerical results

The CFD simulations were carried out to numerically simulate the capillary rise with the same flow and geometry condition that used in the experiment. Figure 2.1-8 shows the selected instantaneous meniscus shapes and contact angles during capillary rise in a tube with D_i=1.67mm from the experimental observation and computational simulation. It is seen that the simulated variation of contact angle is close to what was observed in the experiment.

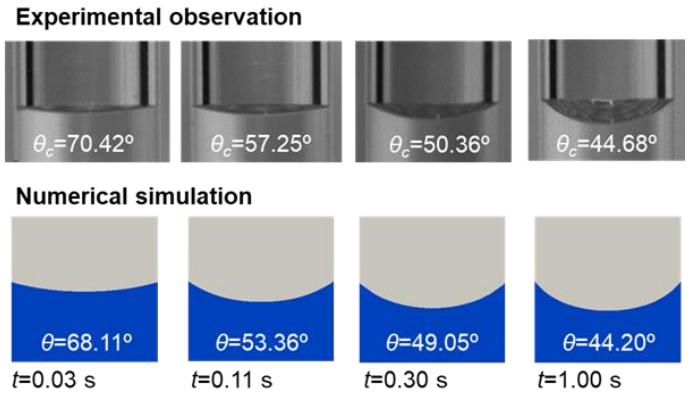

Figure 2.1-8 Instantaneous experimentally-observed and numerically-simulated meniscus shape and contact angle during capillary rise of water in a capillary tube with an inner diameter of D_i=1.67mm

Figures 2.1-9(a-b) show the experimental and CFD results of capillary height (h) for the simulated capillary-driven liquid rise using both constant contact angle (θ_e=44º), and the developed dynamic contact angle (θ_d) model. It is shown in Figs. 2.1-9(a-b) that similar to the theoretical results [Fig. 2.1-7], the computed results of the capillary rise (h) were significantly improved by using the dynamic contact angle model. While the numerical results of the constant contact angle show a substantial discrepancy with the experimental data at the early stage of the capillary rise, the dynamic contact angle model greatly enhances the results as its closer to those obtained by the experiment. In addition, the dynamic contact angle model eliminates the unphysical overshoot that was captured by using the constant contact angle for both tube diameters. It is also seen from Fig. 2.1-9 that the computed final equilibrium heights in both constant and dynamic contact angle models were match with those obtained by the experimental observation.

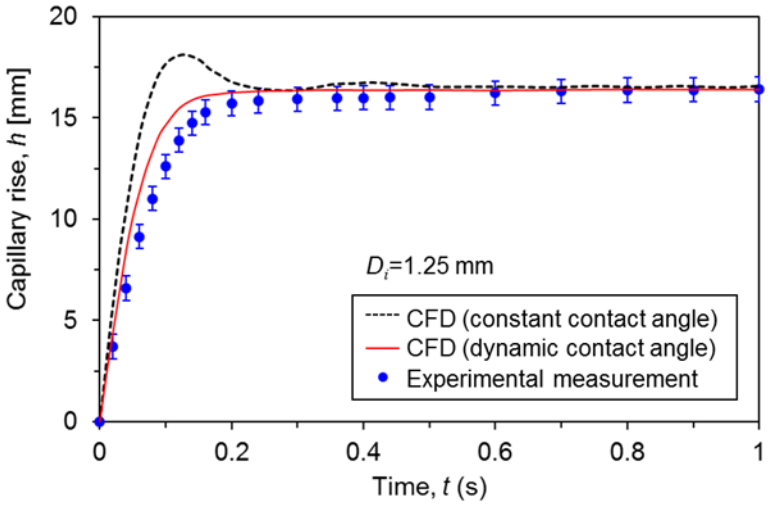

(a)

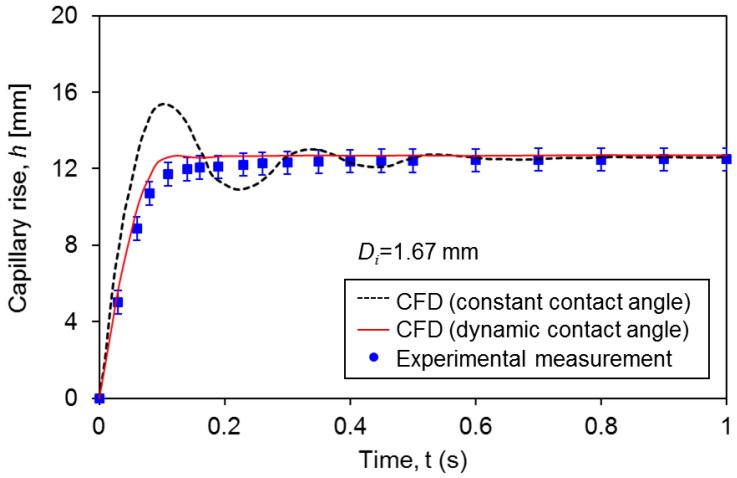

(b)

Figure 2.1-9 Numerical results of the capillary rise (*h*) versus time using constant and dynamic contact angle model for the capillary tube with (a) D_i=1.25 mm; and (b) D_i=1.67 mm

Although the oscillations in Figs. 2.1-7 and 2.1-9 were attributed to the numerical issue caused by constant contact angle, it is reported in literature that at some certain flow and geometry condition, the oscillation may occur during capillary rise. Quere [110] performed an experimental work and presented the oscillations of the liquid column during capillary rise of Ethanol in a glass tube with an inner diameter of D_i=1.30 mm. In this study,

a numerical simulation was performed to resemble the flow condition used in Quere [110]. Figure 2.1-10 shows the comparison of the CFD results of capillary height (h) using the proposed dynamic contact angle model and the experimental results in Quere's work [110]. It is seen that the experimentally-observed oscillation was successfully captured by the numerical simulation.

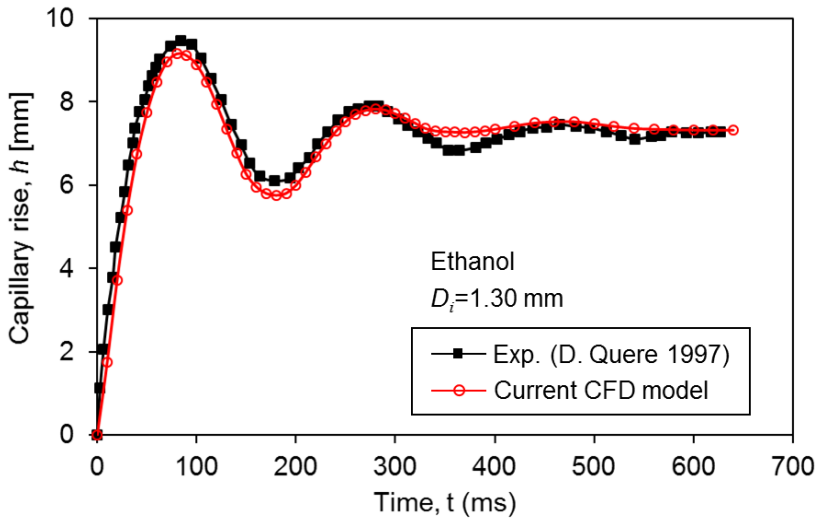

Figure 2.1-10 Numerical results of the oscillation during capillary rise for Ethanol in a glass capillary tube with an inner diameter of D_i=1.30mm and the comparison with experimental data [110]

Figure 2.1-11 illustrates the numerical simulation results of the streamlines in liquid column during capillary rise for the moments around the oscillation presented in Fig. 2.1-10. It is interesting to see that at the initial liquid rise, a small vortex appears near the tube wall at the reservoir entrance. As the liquid rises further, the vortex getting larger near the tube wall until the moment that the liquid column stops instantaneously, where the very large vortex occupies almost the entire liquid column. From that moment, the liquid start to moves down and the vortex shifts toward the tube centerline. As the liquid further moves downward, the vortex getting smaller and finally disappears.

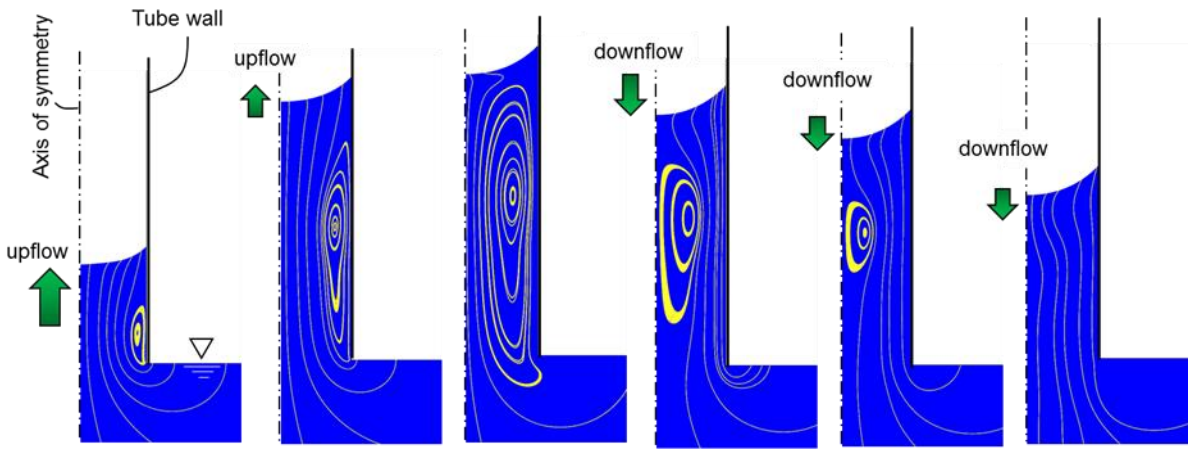

Figure 2.1-11 The numerical simulation of the streamlines in liquid for the moments around the oscillation

2.1.4 Summary

The hydrodynamic characteristics of liquid rise in a vertical capillary tube and the dynamic contact angle was studied experimentally and numerically. An experimental study has been performed to capture the capillary rise of water in glass cylindrical tubes of two different diameters. The experimentally-observed contact angles were corrected accounting for optical distortion. Then, a computational fluid dynamics (CFD) model based on the volume of fluid-continuum surface force (VOF-CSF) method was developed to simulate the dynamic changes of the contact angle during a capillary rise. It was found that using the dynamic contact angle, the numerical and theoretical results for the dynamic capillary rise agreed well with those observed in the experimental observation and eliminates the unphysical oscillations caused by the assumption of constant contact angle. It was also shown that the proposed model successfully simulated the realistic oscillation under certain flow condition.

2.2 OPTICAL DISTORTION

In this research, two problems were experimentally investigated. In the first problem, an experiment was performed to verify the equations presented by Lowe and Kutt [43] to calculate the coordinates of the points located inside a cylindrical tube. In the second problem, the result was then extended to correct the observed meniscus profiles inside cylindrical tubes with various tube diameters and wall thicknesses and determine the static contact angles by curvefitting the corrected meniscus profiles.

2.2.1 Analytical and experimental approach

Correction of point position inside a cylindrical tube:

Determining the spatial coordinates of a certain point on the cross-sectional plane of a cylindrical tube requires two images from different viewing directions. Although an image obtained by one camera can sufficiently determine the equation of a "line", another image from a second camera or a mirror is required to determine the coordinate of a "point" on the line [43]. The method proposed by Lowe and Kutt [43] is adopted in the current study to calculate the positions of the points in cylindrical tubes. The point method is briefly described here for an introduction of an extended method for multi-dimensional geometries like liquid-gas interface (meniscus) and contact angles

Consider a point *P* representing a certain point inside a cylindrical tube as shown in Fig. 2.2-1.

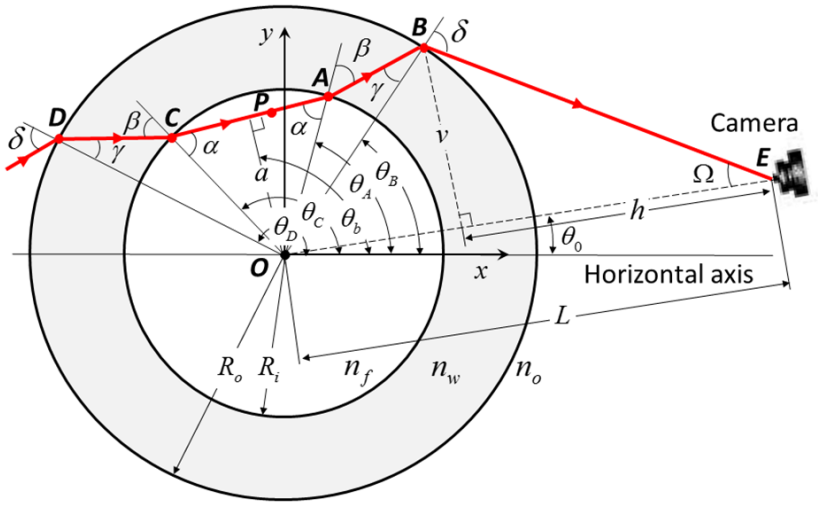

Figure 2.2-1 Refraction of a light ray passing through a point *P* inside a cylindrical tube

To determine the spatial coordinates of the point, one camera is located at a distance *L* from the centerline of the tube to take an image. The light ray passing through the point *P* which enters the camera is designated by the path *PABE*, with respect to angles, α, β, γ and δ. This ray coming at an angle Ω relative to the camera axis can be determined from the height v and base *h* of the triangle *OBE* and using the Pythagorean Theorem (further explanation of the calculation method is provided at the end of this section). Then, the angles α, β, γ and δ can be expressed as a function of the angle Ω.

$$\sin\alpha = \frac{n_o}{n_f}\frac{L}{R_i}\sin\Omega, \tag{2-10}$$

$$\sin\beta = \frac{n_o}{n_w}\frac{L}{R_i}\sin\Omega, \tag{2-11}$$

$$\sin\gamma = \frac{n_o}{n_w}\frac{L}{R_o}\sin\Omega, \tag{2-12}$$

$$\sin\delta = \frac{L}{R_o}\sin\Omega, \tag{2-13}$$

where n_o, n_f, and n_w are the refraction indices of gas (air), liquid (water) and tube wall (glass), respectively. Their values are $n_o = 1$, $n_f = 1.33$, $n_w = 1.49$.

The angles θ_A, θ_B and θ_C are determined by the angle relations as below

$$\theta_A = \delta + \beta - \gamma - \Omega + \theta_0, \tag{2-14}$$

$$\theta_B = \delta - \Omega + \theta_0, \tag{2-15}$$

$$\theta_C = \pi + \delta - 2\alpha + \beta - \gamma - \Omega + \theta_0. \tag{2-16}$$

To facilitate the geometrical analysis, the line *AC* on the light path through the point *P* is expressed in a polar coordinate by

$$r\cos(\theta - \theta_b) = a, \tag{2-17}$$

where r and θ are the variables of a polar coordinate. a represents the length of the perpendicular bisector from the origin *O* to the line *AC* and θ_b is the angle of the bisector with respect to the horizontal axis. a and θ_b are given by

$$a = R_i \sin\alpha, \tag{2-18}$$

$$\theta_b = \frac{1}{2}(\theta_c + \theta_A) = \theta_0 + \frac{\pi}{2} - \alpha + \beta - \gamma + \delta - \Omega. \tag{2-19}$$

Figure 2.2-2 illustrates a two-image method using two photo images taken in two different viewing angles.

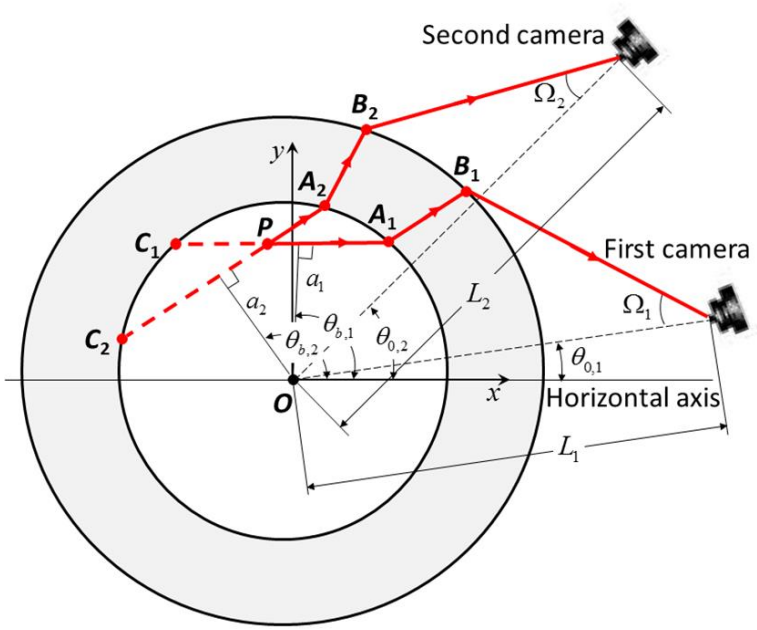

Figure 2.2-2 Two-camera setup to observe a point P inside a cylindrical tube from two different viewing angles

The polar equations of two independent light rays intersecting at the point *P* inside the tube can be determined by $r\cos(\theta-\theta_{b,1})=a_1$ and $r\cos(\theta-\theta_{b,2})=a_2$ which represent the lines A_1C_1 and A_2C_2 respectively. With further mathematical derivations, the position of the point *P* in a cartesian coordinate are given by

$$x_p=\frac{a_1\sin\theta_{b,2}-a_2\sin\theta_{b,1}}{\sin(\theta_{b,2}-\theta_{b,1})}, \tag{2-20}$$

$$y_p=\frac{a_2\cos\theta_{b,1}-a_1\cos\theta_{b,2}}{\sin(\theta_{b,2}-\theta_{b,1})}. \tag{2-21}$$

Figure 2.2-3 depicts a two-image method used for an experimental validation of Eqs. (2-20) and (2-21) using the point *P* with pre-known spatial coordinates.

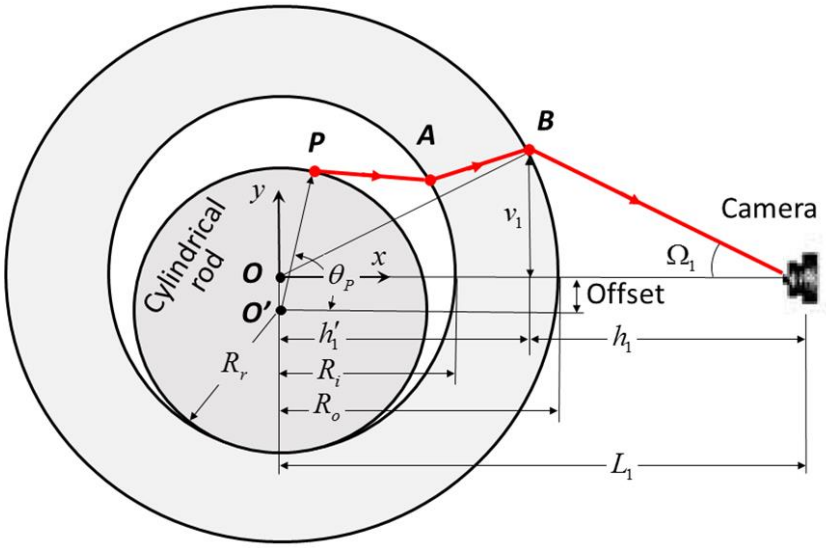

Figure 2.2-3 Single-camera setup to determine the coordinate of a point *P* on a cylindrical rod inside a cylindrical tube

In the experiment, the point *P* was marked on a strip of paper with a graduated scale wrapped around a cylindrical rod which was inserted to a glass tube on a horizontal surface (refer Fig. 2.2-5). The scaled rod in the diameter of 16.0 ± 0.3 mm was placed in the glass tube in the outer diameter of 25.4 ± 0.4 mm. The exact coordinates of the tracer points on the rod were obtained directly using the scales on the rod. A camera was placed in front of the glass tube to acquire a first image of the tracer points and then the camera was moved by an angle of 90° about the centerline on the plane of the tracer points on the tube to take a second image.

In order to obtain the coordinates of a certain point *P* (Fig. 2.2-3), the quantities L_1 and Ω_1 must be determined. L_1, the distance from the center of the tube to the camera at the first angle, was directly measured by a laser distance measurer (BOSCH, GLM80) with

an accuracy of ± 1.5 mm. Using the photo acquired by the camera, the angle Ω_1 can be calculated using the scale on the rod by

$$h_1' = \sqrt{R_o^{\,2} - v_1^{\,2}}, \tag{2-22}$$

$$h_1 = L_1 - h_1', \tag{2-23}$$

$$\Omega_1 = \tan^{-1}\left(\frac{v_1}{h_1}\right). \tag{2-24}$$

Then, the camera is placed in the second angle to obtain the second image and the same approach was repeated to determine L_2, and Ω_2. Finally, the polar coordinate of the point *P* relative to the center (*O'*) of the rod is determined by

$$r_p = \sqrt{x_p'^{\,2} + y_p'^{\,2}}, \tag{2-25}$$

$$r\theta_p = \tan^{-1}\left(\frac{y_p'}{x_p'}\right), \tag{2-26}$$

$$x_p' = x_p, \quad y_p' = y_p + offset, \tag{2-27}$$

where, the "*offset*" is the vertical distance between the centers of the rod and tube.

Correction of meniscus profile and contact angle:

An accurate geometrical measurement of a liquid-gas interface (meniscus) formed in a vertical tube without optical correction is crucial to determine the true contact angle between liquid and tube wall. Note that since the meniscus formed in a vertical tube has an axisymmetric profile varying in the functions of the radial and axial coordinates and there is no curvature in the axial direction of the tube, the images are optically distorted in the radial direction only, which requires one photo image for optical correction.

Figure 2.2-4 illustrates a situation where a point *A* on the inner tube wall appears to be at the point *B* on the outer tube wall, if viewed from a camera. The triangle *OAB* and another triangle *AMB* (in the inset of Fig. 2.2-4) are used to determine the location of the actual point *A* from the apparent point *B*. The line *BM* is the distance between the actual point *A* and the apparent point *B* and is determined by

$$BM = AB\sin(\theta_A - \beta), \tag{2-28}$$

where,

$$AB = R_o \frac{\sin(\theta_A - \theta_B)}{\sin(180 - \beta)}. \tag{2-29}$$

Note that the shift distance (the line *BM*) is increased with the distance from the tube centerline.

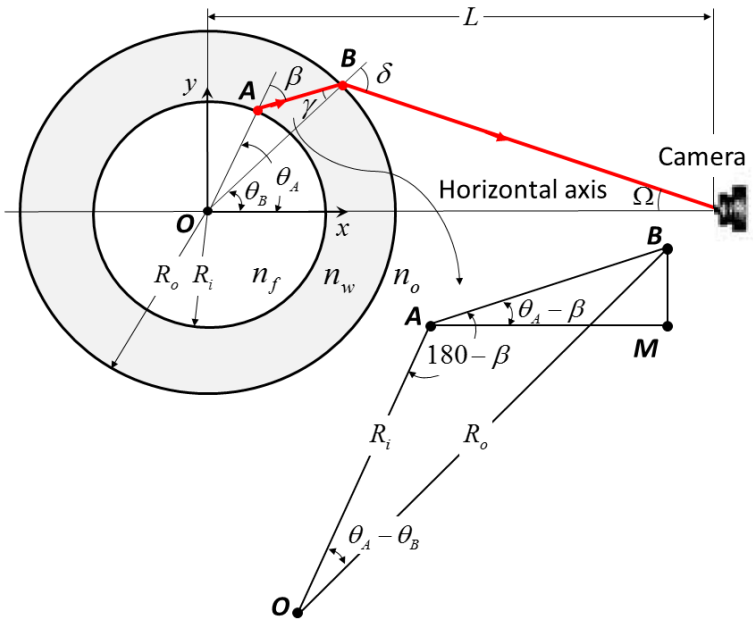

Figure 2.2-4 Single-camera setup to determine the coordinate of a point A on the inner wall of a cylindrical tube

A long-distance microscope was used to take magnified photographs of the menisci in the cylindrical tubes dipped into deionized water in a beaker. The tubes were vertically

installed in the beaker. The point-by-point correction method discussed in previous section can be used to find the corrected meniscus profiles. The photographs of the menisci from the microscope were first converted from RGB to gray scale images using MATLAB and then, all the pixels in the gray-scale images were designated to be either Black or White using a threshold value of 0.06 and saved in BW binary images. Using the built-in function for edge detection available in MATLAB, the meniscus curves were detected and marked in white with their spatial coordinates in a pixel unit. Then, a MATLAB script was used to compute the true spatial coordinates of the meniscus curve by the point-by-point correction method. Finally, curvefit equations of the true meniscus curves were used to calculate their contact angles.

2.2.2 Results

Figure 2.2-5(a) depicts a cylindrical rod (16 mm in diameter) located in a glass tube (25 mm in dimeter) showing five tracer points marked around the rod. Those points represent arbitrary points in the tube so that their known spatial coordinates are used to validate their computed positions. Figure 2.2-5(b-c) shows the two different images acquired by a camera in two different viewing directions (front and top views). As described earlier in Fig. 2.2-2, the two angled photos of the tracer points with the measured distances (L_1, L_2) and angles (Ω_1, Ω_2) of the camera from the tube center are used to compute the real coordinates of the specified points.

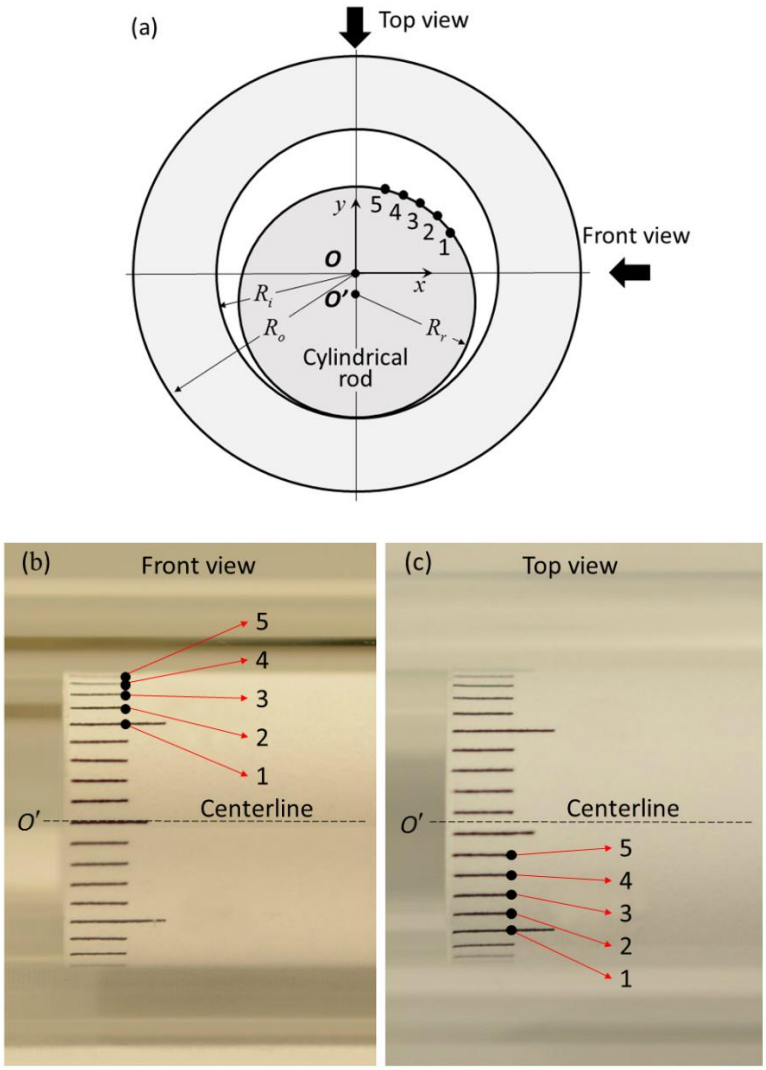

Figure 2.2-5 (a) Observation of the points on a cylindrical rod in a cylindrical tube. Photos of the five test points acquired by a camera: (b) front and (c) top views

The results of the computed positions of the points with the corresponding actual positions are shown in Fig. 2.2-6. The computed and actual coordinates and the associated errors are listed in Table 2.2-1.

Table 2.2-1 Comparison of the actual and computed spatial coordinates of five different points inside a cylindrical tube and corresponding errors

No. of Point	$r^*_{p,e}$ [mm]	$r_{p,c}$ [mm]	ε_{r_p} [%]	$\theta_{p,e}$ [deg]	$\theta_{p,c}$ [deg]	ε_{θ_p} [%]
1	8.0	9.0	12.5	35.8	37.7	5.2
2	8.0	9.2	15.0	43.0	44.5	3.6
3	8.0	9.4	17.5	50.7	50.1	-1.1
4	8.0	9.7	21.2	57.3	56.3	-1.7
5	8.0	9.5	18.7	64.5	62.1	-3.6

* This value has an uncertainty of 0.3 mm.

According to the uncertainty analysis using Engineering Equation Solver (EES), the uncertainties in the computed radial (r_p) and angular (θ_p) coordinates did not exceed 8.5% and 6.3%, respectively. As seen in Fig. 6, the angular positions were predicted better than their radial positions. This biased results might be caused by a bigger uncertainty for the radial coordinate calculation due to the dimensional tolerance of the tube diameters.

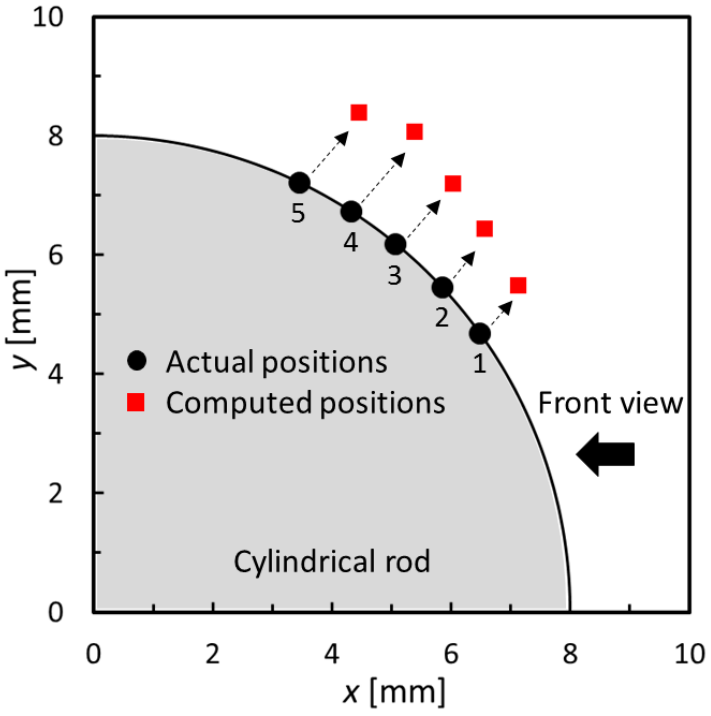

Figure 2.2-6 Exact and computed locations of the five test points on a cylindrical rod in a cylindrical tube while viewed outside the tube

Correction of meniscus profile and contact angle in a vertical cylindrical tube

Five cylindrical tubes (ACCU-Glass company) with different inner tube diameters (0.175 ~ 1.674 mm) and wall thicknesses (0.212 ~ 0.912 mm) were used to study the effect of the tube diameter and wall thickness on the optical distortion of liquid-gas interface (meniscus). The dimensions of the tubes and corresponding Bond numbers are listed in Table 2.2-2.

Table 2.2-2 Dimensions of the cylindrical tubes used in the current study and the corresponding bond numbers

No. of Tube	D_i [mm]	D_o [mm]	t [mm]	Bo [-]
1	1.245	1.670	0.212	0.210
2	1.120	1.520	0.200	0.170
3	0.576	1.330	0.377	0.045
4	1.674	2.250	0.288	0.375
5	0.175	2.000	0.912	0.004

The Bond number is a dimensionless number representing the ratio of gravitational force to surface tension force. A high value of the Bond number indicates that the fluid in the tube is relatively unaffected by surface tension effects; a low value (typically less than one) indicates that surface tension dominates. The images of the meniscus profile of the cylindrical tubes in a vertical position shown are shown in Fig. 2.2-7, which are corrected by the correction method discussed in previous section.

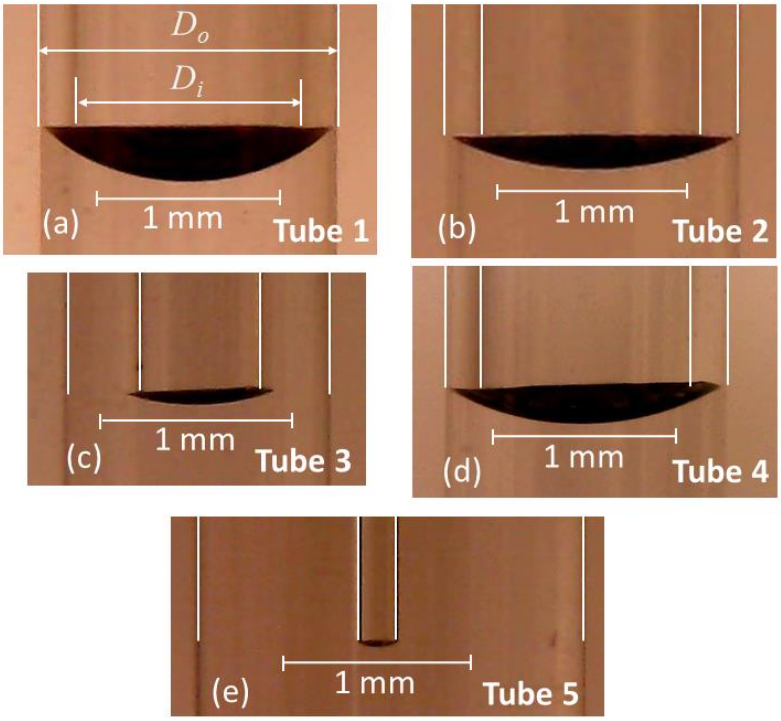

Figure 2.2-7 Observation of the water-air interfaces (menisci) in cylindrical tubes with different tube diameters and wall thicknesses.: (a) Tube #1, (b) Tube #2, (c) Tube #3, (d) Tube #4, and (e) Tube #5. The inner and outer walls of the tubes are highlighted in white lines

Figure 2.2-8(a) shows the original photo of the meniscus in a cylindrical tube of D_o = 1.670 ± 0.05 mm and D_i = 1.245 ± 0.05 mm ["Tube 1" in Figure 2.2-7(a) and Table 2.2-2] which was captured by a long-distance microscope. The meniscus in the tube has a concave shape (hydrophilic, $\theta_c < 90^\circ$) due to the affinity of water to glass. Figure 2.2-8(b) depicts a conventional way to determine the apparent contact angle of the meniscus by a tangent line at the intersection between a horizontal line and a circle passing of the meniscus. This method could reasonably determine the contact angle (46.7°), but the optical distortion prevents accurate measurement.

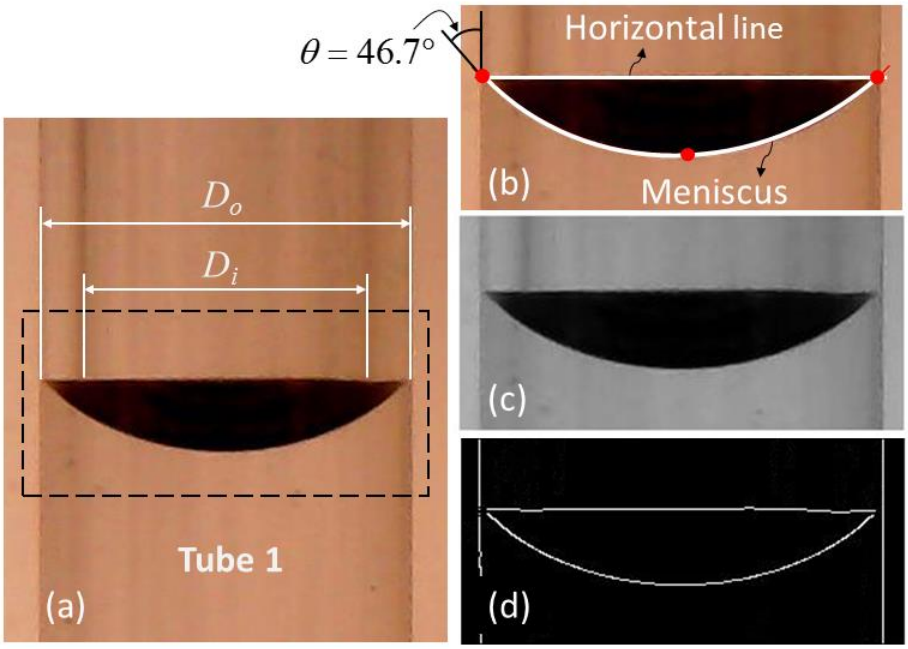

Figure 2.2-8 Original and processed photo images of the water-air interface (meniscus) in a cylindrical tube (Tube 1): (a) original photograph, (b) measurement of the contact angle of the meniscus by a conventional method (apparent angle), (c) conversion of the original RGB image into a gray-style image using MATLAB and (d) detection of edges of the gray-style image using threshold = 0.06

Figures 2.2-8(c-d) show the processed images [gray image in Fig. 2.2-8(c) and black/white image in Fig. 2.2-8(d)] of the original RGB image [Fig. 2.2-8(a)] using MATLAB. By using an edge detection function in MATLAB, the meniscus profile as a concave surface was marked as a white curve [Fig. 2.2-8(d)] along with the vertical lines for the outer tube wall.

In Fig. 2.2-9, the dashed curve represents the half portion of the observed meniscus profile whereas the corrected profile is shown as the solid curve. Applying the correction method described earlier, every single point on the observed curve was shifted toward the

tube center by a certain distance called as “Distortion”. As shown in Fig. 2.2-9, the distortion is increased proportionally with the radial distance from the tube centerline and therefore the bottom of the meniscus on the tube centerline is unchanged. Interestingly, the observed meniscus profile seemingly penetrates into the tube wall showing the triple-phase contact point (point *S* in Fig. 2.2-9). It is found that the end point (point S') of the corrected profile is on the inner wall of the tube.

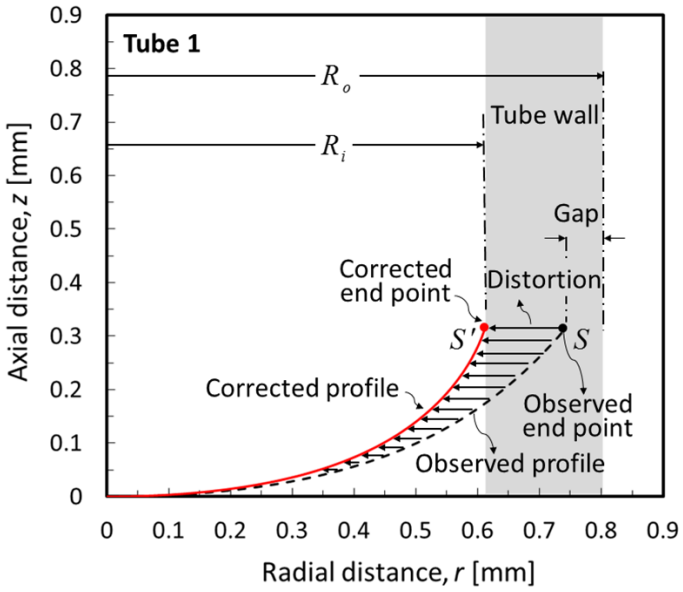

Figure 2.2-9 Corrected profile of the half portion of the water-air interface (meniscus) in a cylindrical tube (Tube 1)

In order to further investigate the disputable results on the end point of the observed meniscus curve and quantify the accuracy of the optical correction used in Figs. 2.2-8 and 2.2-9, another experiment was performed using a plug gauge as solid object with a known diameter under the same light refraction condition used in Figs. 2.2-8 and 2.2-9. As shown in Fig. 2.2-10, a plug gauge (metric, class Z) with the diameter of 1.21 mm and painted in black was inserted into a cylindrical tube (Tube 2.2-1) located in a horizontal position and

filled with water. As shown in Fig. 2.2-10, the plug gauge in the cylindrical tube was optically distorted (D_d) as compared to the actual diameter (D_a). Using the same correction method used in Fig. 2.2-9, the differences between the actual and the corrected diameters of the plug gauge from three measurements were found to be less than 3%.

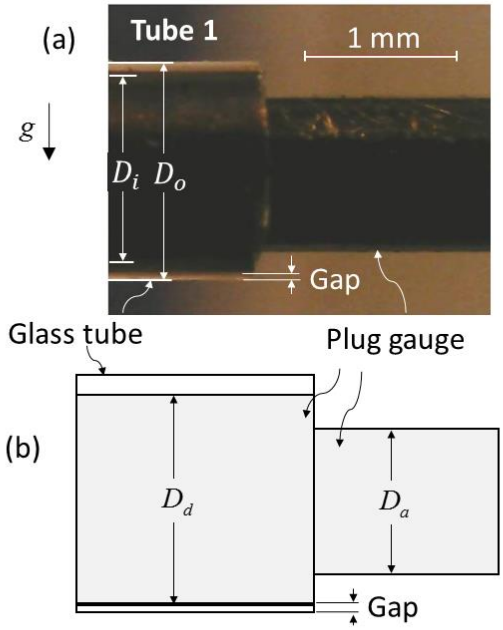

Figure 2.2-10 Observation of a plug gauge with the diameter of 1.21 mm in a cylindrical tube (Tube 1) filled with water: (a) original photograph of the plug gauge in the tube and (b) schematic of the plug gauge showing the distorted diameter (D_d) and actual diameter (D_a)

The optical distortions of the five cylindrical tubes (Fig. 2.2-7) are shown together in a normalized radial coordinate (r/R_i) as shown in Fig. 2.2-11. For all the images, the distance of the camera to the tube center was kept at 50 mm. The optical distortion is affected by both the tube diameter and wall thickness but becomes bigger for the tubes with smaller inner diameter.

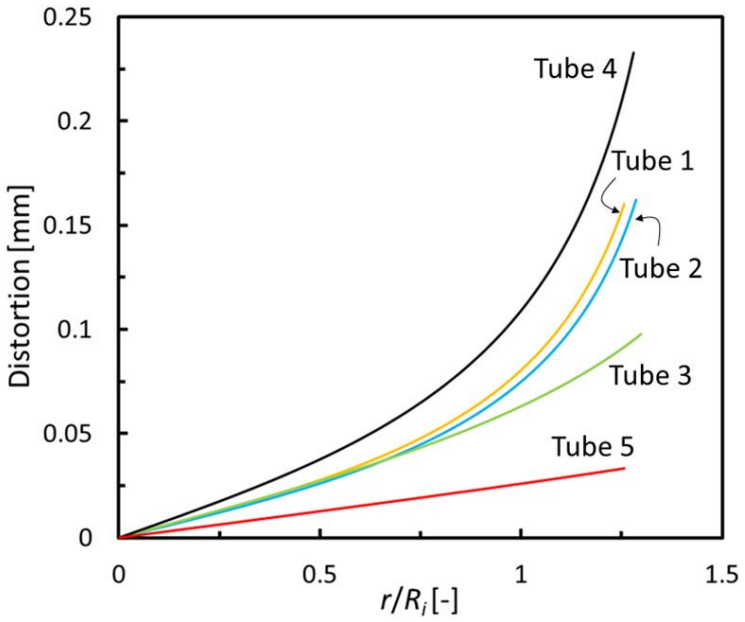

Figure 2.2-11 Optical distortion of the water-air interfaces (menisci) in cylindrical tubes in a non-dimensional radial coordinate

Using the corrected meniscus profiles, the contact angle of the meniscus with the tube wall can be accurately determined. The methods and results of the contact angle measurement are discussed in Figs. 2.2-12 and 2.2-13. Figure 2.2-12(a) shows the MATLAB-processed image of the original photo for the cylindrical tube (Tube 2.2-1) in a scale of 0.007 mm/pixel which was also shown in Fig. 2.2-8(d).

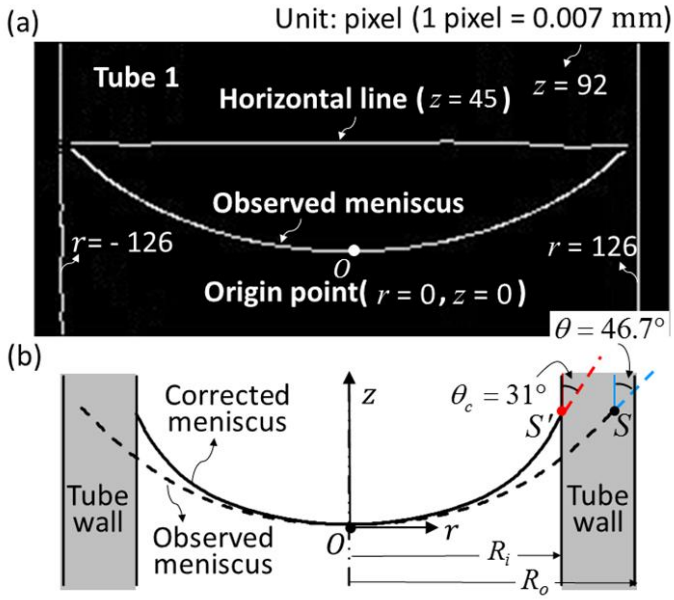

Figure 2.2-12 (a) MATLAB-processed BW image of the water-air interface (meniscus) in a cylindrical tube (#1) used to obtain (b) the corrected profile of the observed meniscus and the corrected contact angle

Figure 2.2-12(b) shows the profiles of the observed and corrected menisci and their respective contact angles. The contact angles are measured at the intersections of the horizontal line and meniscus curves. The end region of the original meniscus unrealistically appears to be extended into the wall due to the optical distortion as discussed in Figs. 2.2-9 and 2.2-10. A 6th-order polynomial was used to curvefit the original meniscus profile [Eq. (2-30)] and then the corrected meniscus profile [Eq. (2-31)] was obtained using the correction method described earlier.

$$z = c_1 r^6 + c_2 r^5 + c_3 r^4 + c_4 r^3 + c_5 r^2 + c_6 r + c_7 \,, \tag{2-30}$$

$$z_c = c_1' r^6 + c_2' r^5 + c_3' r^4 + c_4' r^3 + c_5' r^2 + c_6' r + c_7' . \tag{2-31}$$

Then, the corrected contact angle was calculated using the formula of the tangent line of the corrected meniscus at its end point as below

$$\frac{dz_c}{dr} = 6c_1'r^5 + 5c_2'r^4 + 4c_3'r^3 + 3c_4'r^2 + 2c_5'r + c_6', \quad (2\text{-}32)$$

$$\theta_c = 90 - \tan^{-1}\left(\frac{dz_c}{dr}\right)_{r=R_i}. \quad (2\text{-}33)$$

Table 2.2-3 lists the curvefit equations of the observed and corrected meniscus profiles as well as respective contact angles of the five cylindrical tubes.

Table 2.2-3 Dimensions of the cylindrical tubes used in the current study and the corresponding bond numbers

No. of Tube	z [mm]	θ[deg]	z_c [mm]	θ_c [deg]
1	$-0.2052\,r^6 + 0.4066\,r^4 + 0.2843\,r^2$	46.7	$2.5473\,r^6 - 0.286\,r^4 + 0.4106\,r^2$	31.0
2	$0.5689\,r^6 - 0.2337\,r^4 + 0.2839\,r^2$	54.2	$4.8607\,r^6 - 1.3027\,r^4 + 0.4002\,r^2$	41.3
3	$22.375\,r^6 - 3.0089\,r^4 + 0.4463\,r^2$	56.9	$167.7\,r^6 - 11.672\,r^4 + 0.7386\,r^2$	37.5
4	$0.0338\,r^6 - 0.0326\,r^4 + 0.2695\,r^2$	58.5	$0.7292\,r^6 - 0.4658\,r^4 + 0.3915\,r^2$	36.3
5	$-15376\,r^6 + 460.2\,r^4 + 0.2374\,r^2$	44.5	$-108887\,r^6 + 1797\,r^4 + 0.491\,r^2$	32.8

* r has a unit of mm.

For a validation purpose, the contact angles of the cylindrical tube was compared with the reference value of the static contact angle of water on untreated borosilicate glass which is 32 ± 2° [111]. In Fig. 2.2-13, the corrected static contact angles for the cylindrical tubes are compared with the reference contact angle in an excellent agreement. The optical correction could be directly applicable for the measurement of the dynamic contact angle of the capillary flow in a cylindrical tube which is prone to more inaccurate measurement because of the fast moving meniscus.

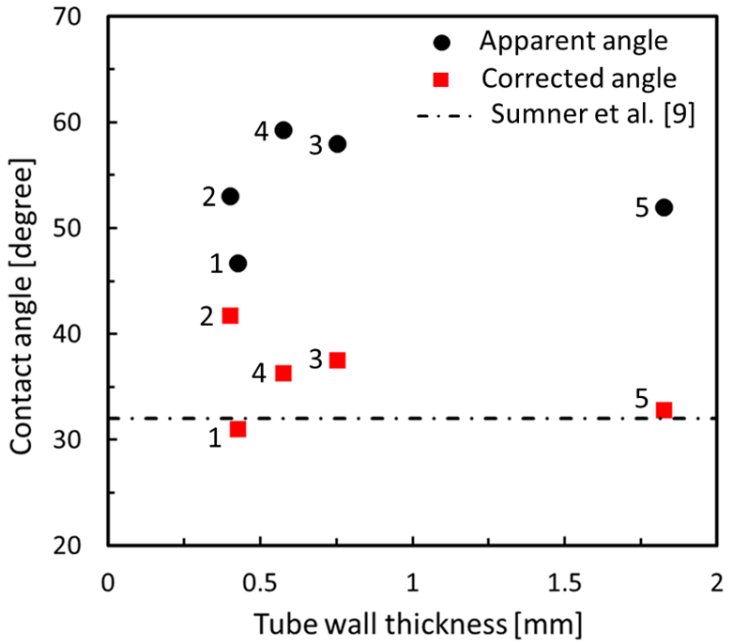

Figure 2.2-13 Comparison of the apparent and corrected contact angles of the water-air interfaces (menisci) in cylindrical tubes. (The numbers near the markers denote the kind of the cylindrical tubes listed in Table 2.)

2.2.3 Summary

An analytical method for the geometrical correction of the optically-distorted geometries of the objects in cylindrical capillary tubes was developed and experimentally validated. Close-up photographs of the stationary menisci in the cylindrical tubes were processed using MATLAB to extract the original meniscus profiles and obtain the corrected meniscus profiles by removing the optical distortion due to light refractions. It was found that the original images show the meniscus unrealistically extended into the tube wall and the convectional method using the optically-distorted images overestimates the contact angles. The corrected contact angles of the cylindrical tubes at different diameters and wall thicknesses are compared with the reference value of the static contact angle in an excellent agreement.

3 CHAPTER 3: ADIABATIC TWO-PHASE FLOW

In this research, the hydrodynamic characteristics of gas-liquid two-phase flow in a circular tube were investigated. Heat transfer is neglected in this section aiming to focus on the hydrodynamic features of in-tube two-phase flow. First in Section 3.1, a set of visualization experiments was performed to observe different two-phase flow regimes. Then, a computational fluid dynamic (CFD) model is presented to simulate two-phase flows. The comparison between the experimentally-observed and numerically-simulated two-phase flow regimes showed that the presented numerical model can reasonably simulate two-phase flows. Next in Section 3.2, the hydrodynamics of two-phase flow were studied under reduced gravity conditions. A horizontal plug flow and a vertical upward slug flow was selected as the baseline condition for gravitational influence.

3.1 TWO-PHASE FLOW REGIMES IN A TUBE

In this work, firstly, a visualization experiment using air-water flows is performed. The air and water flow rates were systematically varied to observe and record images of various flow patterns. The collected data of flow patterns were coordinated based on gas and liquid superficial velocities to compare with classical Baker's [46], Mandhane's [47], and Taitel-Dukler's [48] flow maps. The second part is to develop a computational tool which is validated with experimental results. There, for twenty pre-defined flow conditions, flow patterns were numerically computed, employing volume of fluid (VOF)-continuum surface force (CSF) method. The simulated flow patterns were compared with the experimental results. The accuracy of the CFD simulation results is discussed by

comparison of the computed void fraction and pressure drop against the results from empirical correlations in literature.

3.1.1 Experimentally-observed two-phase flows

Figure 3.1-1 shows a schematic diagram of the overall setup used for the visualization experiments. The transparent test section is a cylindrical glass tube with an internal diameter (D=2R) of 12±0.2 mm and a length (L) of 1000 mm, in a horizontal orientation. Various flow rates of water were provided by a centrifugal pump with a maximum flow rate up to 9.7 GPM and the volumetric flow rate of water was measured with a rotameter with a range of 0.2 ~ 2 GPM and an accuracy of ± 2% of the full scale. Compressed air was mixed with deionized water in a mixer to create two-phase mixture flows at various flow rates in the test section. Two air flow-meters connected in parallel having different flow rate ranges of 2 ~ 25 LPM and 10 ~ 100 LPM with an accuracy of ± 2% of the full scale, were installed in the compressed air line. Water and air flow rates as key experimental parameters were controlled independently to create desirable combinations of flow rates and the experiments were performed at an isothermal and atmospheric condition.

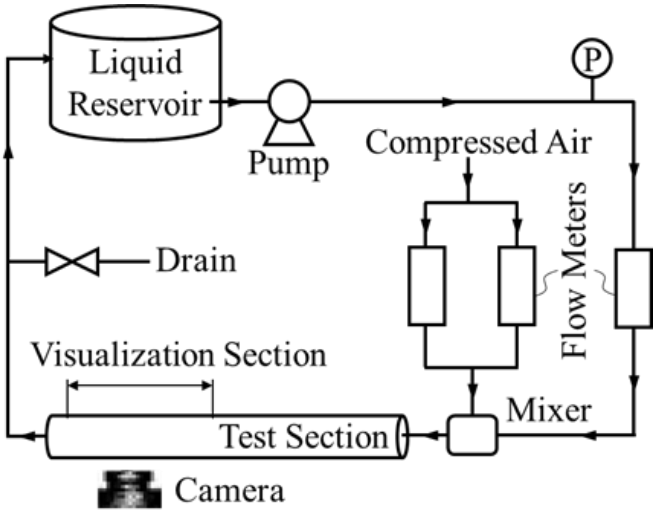

Figure 3.1-1 Schematic of the visualization experimental setup

Visualization experiment was performed downstream near the exit of the test section to capture fully-developed two-phase flows. The visualization zone of the test section is150 mm long ($67 < z/D < 79$). Images of the two-phase flows were recorded by a Nikon D7100 digital camera with a Nikkor 67mm lens at 1,000 fps. A white diffusion screen was placed behind the glass tube as background with an indirect lighting system consisting of two ultra-bright LED (light emitting diode) strips with diffuser covers.

Wide ranges of superficial velocities of liquid (J_L=0.1 ~ 1.2 m/s) and gas (J_G=0.3 ~ 12.5 m/s) were used to create various two-phase flow patterns. The superficial velocities of liquid and gas phases are defined as:

$$J_L = \frac{Q_L}{A}, \tag{3-1}$$

$$J_G = \frac{Q_G}{A}. \tag{3-2}$$

where Q_L and Q_G are the volumetric flow rates of liquid and gas, respectively. A is the tube cross-sectional area. According to the uncertainty analysis using Engineering

Equation Solver (EES), the uncertainties of J_L and J_G did not exceed 7.2% and 9.5%, respectively.

Figure 3.1-2 illustrates the images from the visualization experiments showing various flow patterns such as stratified, wavy, plug, slug and annular flows which were created with different combination of air and water flow rates. Bubbly flow, however, were not observed as this flow pattern occurs at very high liquid flow rates and was out of the operating range of the liquid pump used in this experiment.

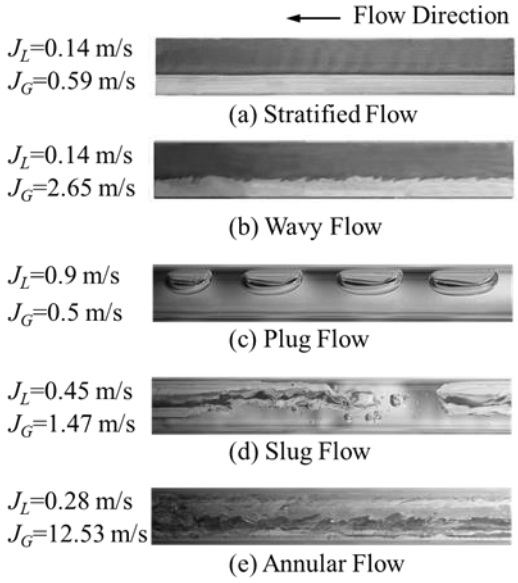

Figure 3.1-2 Experimentally-observed two-phase flows

Figures 3.1-3[(a)-(c)] illustrate the experimental result of 330 observed flow patterns plotted in Baker's [46], Mandhane's [47], and Taitel-Dukler's [48] flow maps, respectively. It can be seen that as expected, none of the flow maps are satisfactory in predicting all the present experimental results. Possible reasons for such a deviation are: (a) the flow transition from one pattern to another is rather gradual. Thus, the transitional line between different flow patterns should be considered as a zone and not a distinct line.

(b) Any flow map differs more or less from one another. The difference between flow maps could be attributed to any dissimilarities in experimental setups, and conditions used by researchers. For example, the data in Baker's flow map were obtained using 25.4 mm I.D. tube, and in Mandhane's flow map the tubes with the diameters ranging from 12.7 to 155 mm were used. However, the present study used a glass tube with a diameter of 12 mm. (c) The characterization of flow patterns and categorization into flow maps are subjective rather than objective. Particularly, those data points close to the transition regions may be interpreted as different flow patterns from one researcher another.

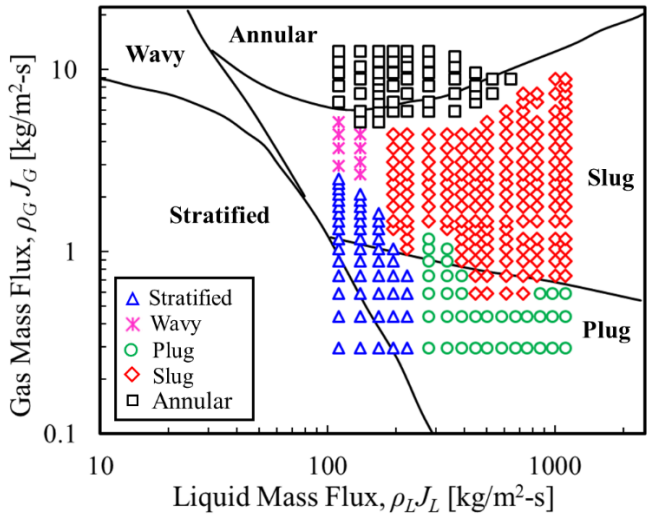

(a)

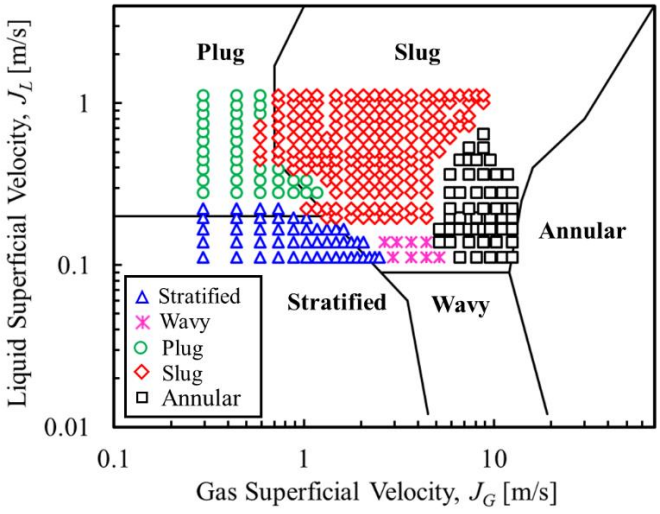

(b)

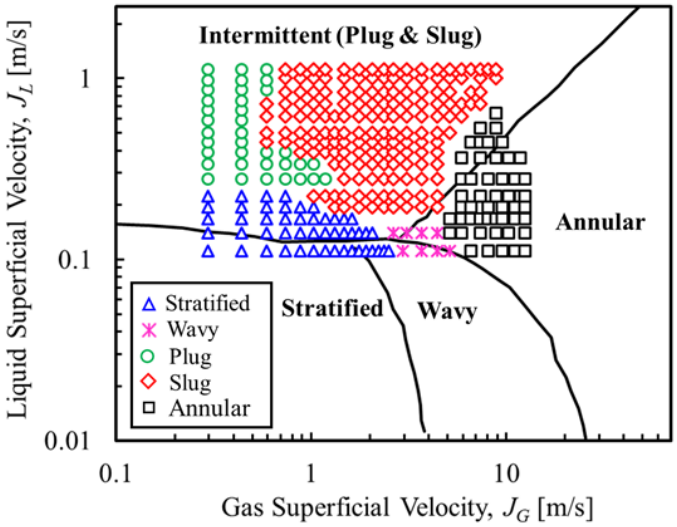

(c)

Figure 3.1-3 Comparison of the present experimental results with three different flow maps: (a) Baker's [46], Mandhane's [47], and Taitel-Dukler's [48]

The present experimental results show reasonable agreement with Taitel-Dukler's flow map [Fig. 3.1-3(c)]. However, in this flow map, there is no transition line between plug and slug flow regimes. Also, this map is based on a simplified theoretical model and some of their assumptions has received a great deal of criticism from other researchers [51]. For example, for the transition between annular flow and intermittent flow (plug and

slug flows), they simply assumed that when the equilibrium liquid level occupies more than half of the tube, intermittent flow will happen; otherwise annular flow will develop. However, Lin and Hanratty [112] believe that annular flow is the result of combined effects of entrainment and deposition.

The present experiment results fit in Mandhane's flow map [Fig. 3.1-3(b)] except that the annular flow was captured at relatively lower gas superficial velocities and also the wavy flow patterns were obtained at relatively higher water flow rates. Perhaps Mandhane's flow map is the most commonly accepted for horizontal flows since the wide range of parameter values were used to produce the map.

3.1.2 Numerically-simulated two-phase flows

The VOF-CSF method described in Section 2.1 was employed here to simulate two-phase flows in a tube. Figure 3.1-4 shows a computational grid system of a semi-circular tube (half-tube) used in the CFD simulation comprising of 691,200 hexahedral elements with each cubic cell size of 0.5 mm. Near the tube wall, a locally refined grid was applied which assist in capturing thin liquid films. The half-tube geometry was considered assuming a symmetry of the flow with respect to the central vertical plane of a horizontal tube with a diameter (D) of 12 mm and a length (L) of 1600 mm aiming to reduce the computational time, while still capturing the physics of two-phase flows.

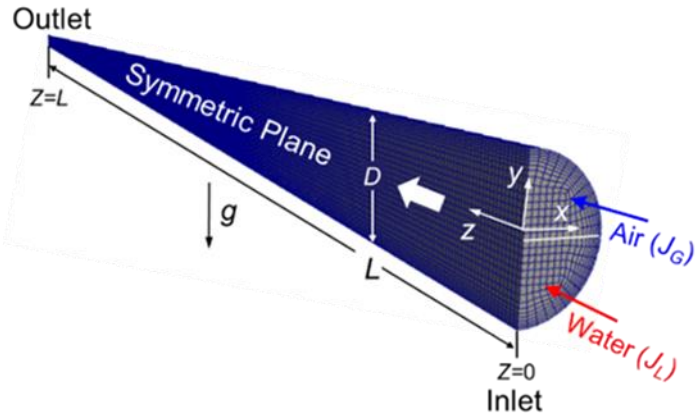

Figure 3.1-4 Computational grid system of a half-tube geometry

Table 3.1-1 lists the thermophysical properties of working fluids and tube dimensions used in the simulations. As shown in Fig. 3.1-4, air and water were introduced with a uniform velocity from the quarters of the inlet, respectively. The two-phase (air-water) mixture flow is fully developed after a certain time and distance from the tube inlet. The uniform inlet velocity of each phase [air (α=0) and water (α=1)], rather than injecting the fully-mixed two-phase flows, allows a direct control of actual inlet velocity of each phase. At the tube wall a no-slip condition was applied and at the tube outlet, pressure was set to atmospheric pressure. Note that the simulations were performed under an isothermal condition [Eqs. (2-1)-(2-3)]. Therefore, no temperature boundary condition is applied. In order to study the complex hydrodynamics of two-phase flows, a transient simulation with a time step of 10^{-4} s was performed. To ensure minimizing the inlet and outlet effects, the data used for post-processing were carried out in a fully-developed region near the outlet (1200 mm < z <1500 mm). Gravitational field was also applied opposite to the flow direction to create an upward flow configuration.

Table 3.1-1 Thermophysical properties of working fluids and tube dimensions used for the simulations

Parameter	Value
Density of air, ρ_G [kg/m^3]	1
Density of water, ρ_L [kg/m^3]	1000
Kinematic viscosity of air, v_G [m^2/s]	1.480×10^{-5}
Kinematic viscosity of water, v_L [m^2/s]	10^{-6}
Surface tension, σ [N/m]	0.072
Tube diameter, D [mm]	12
Bond number, Bo [-]	19.6
Tube length, L [mm]	1600

Despite the single-phase flow, the corresponding required length for multiphase flow to be fully developed is under debate in literature. In this study, to ensure that the two-phase flow is fully-developed, the cross-sectional profiles of the time-averaged void fraction were compared at various axial coordinates (z=60D, 80D, 100D and 120D). It was found that the flow is fully developed after z=100D (1200 mm). Therefore, the data post-processing were performed in a fully-developed region downstream ($100 < z/D < 120$) to minimize the inlet and outlet effects.

In order to employ a suitable turbulence modeling for the entire simulations, five different air-water flows with various superficial velocities were simulated each flow for two different turbulence models of standard k-ε and SST k-ω. The turbulent properties (k, ε and ω) were initialized at the tube inlet using suitable values described in literature [113]. Since the detail comparison of different turbulence models is beyond the objective of the present study, we focused on the predictive accuracy of the turbulence model on main intermittent characteristics of two-phase plug flows which are void fraction (ratio of a volume occupied by gas to a total volume) and pressure gradient.

Figure 3.1-5 compares the two different turbulence models of standard k-ε and SST k-ω for the numerical values of void fraction [Fig. 3.1-5(a)] and pressure gradient [Fig. 3.1-5(b)] from the computational simulations with those predicted by empirical correlations. For the void fraction and pressure gradient, the correlations proposed by Woldesemayat and Ghajar [114] and Muller Steinhagen and Heck [115] were chosen respectively. It is seen from Figs. 3.1-5[(a)-(b)] that both turbulence models predict satisfactory results for void fraction (ε) and pressure gradient (dp/dx) within a deviation of ±15% against those obtained by empirical correlations. The mean absolute error (MAE) values were calculated by summing over the five different simulates cases using Eqs. [(3-3)-(3-4)]

$$\left(\mathrm{MAE}\right)_{\varepsilon} = \frac{1}{N}\sum \frac{\left|\varepsilon_{\mathrm{numerical}} - \varepsilon_{\mathrm{correlation}}\right|}{\varepsilon_{\mathrm{correlation}}} \times 100\%, \tag{3-3}$$

$$\left(\mathrm{MAE}\right)_{\frac{\mathrm{d}p}{\mathrm{d}x}} = \frac{1}{N}\sum \frac{\left|\left(\frac{\mathrm{d}p}{\mathrm{d}x}\right)_{\mathrm{numerical}} - \left(\frac{\mathrm{d}p}{\mathrm{d}x}\right)_{\mathrm{correlation}}\right|}{\left(\frac{\mathrm{d}p}{\mathrm{d}x}\right)_{\mathrm{correlation}}} \times 100\%. \tag{3-4}$$

Figure 3.1-5(c) compares the MAE values of the computed void fraction and pressure gradient from the simulation using the two turbulence models. The MAE values of the SST k-ω model were lower: 5.9% and 6.8% for void fraction and pressure gradient respectively. Therefore, the SST k-ω model was selected for the simulation of turbulent flows (air-water flows) in this study.

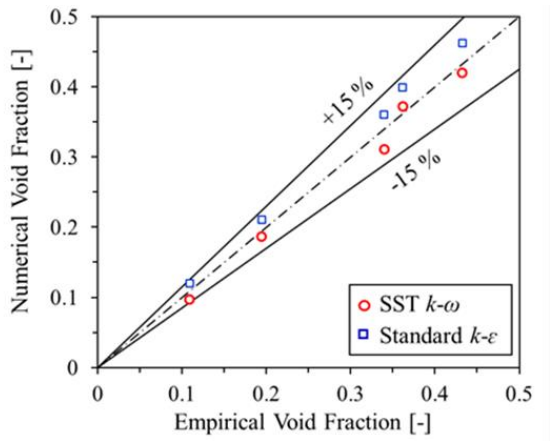

(a)

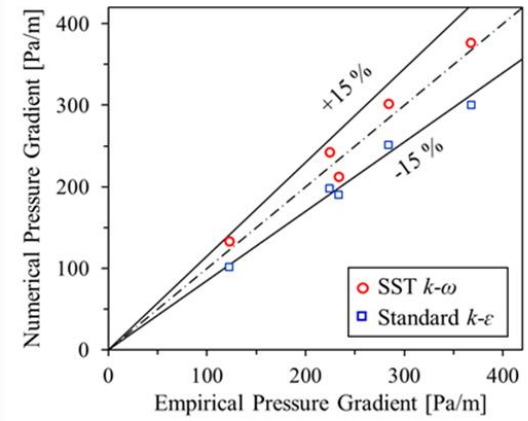

(b)

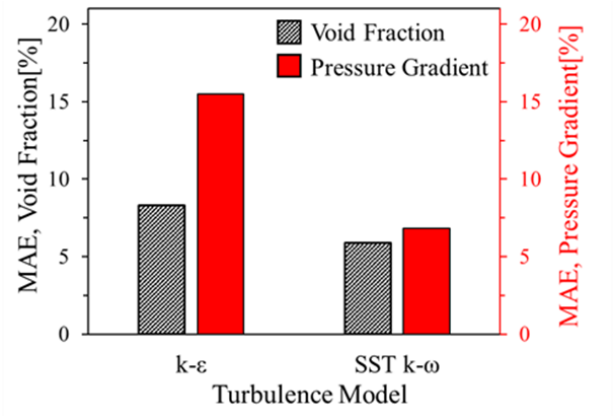

(c)

Figure 3.1-5 Comparison of the numerical results with empirical results of (a) void fraction from Woldesemayat-Ghajar's [114] correlations; (b) pressure gradients from Muller-Heck's [115] correlation; (c) mean absolute errors (MAE) from two different turbulence models

In order to investigate the reasonability of applying a symmetric boundary condition to the symmetric plane, three simulations for plug, wavy and slug flows were run using a full tube with the same length (L) and diameter (D) of 1600 mm and 12 mm, respectively. Figures 3.1-6[(a)-(c)] shows the longitudinal (u_x) and lateral (u_z) velocities versus radial distance for plug, wavy and slug flows, respectively at the axial distance of 1200 mm from the tube inlet along the vertical centerline of the cross section. The lateral velocity (solid blue line) is almost zero for the case of plug and slug flows [see Figs. **3.1-6**(a) and (c)]. However, for a wavy flow [Fig. **3.1-6**(b)], a small lateral velocity exists, but it is still negligible compared to the longitudinal velocity suggesting a negligible flow across the axial mid-plane of the tube compared with the longitudinal mass flow. Therefore, it can be concluded that a symmetric boundary condition at the mid-plane of the tube which was used in this study is a reasonable approximation to reduce the computational time.

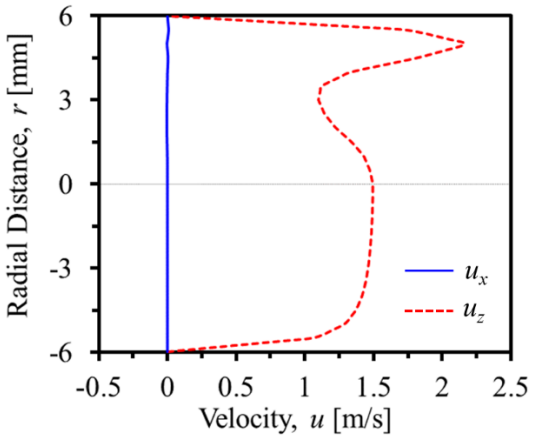

(a)

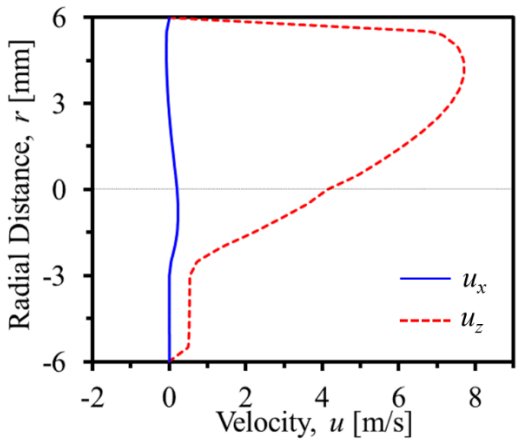

(b)

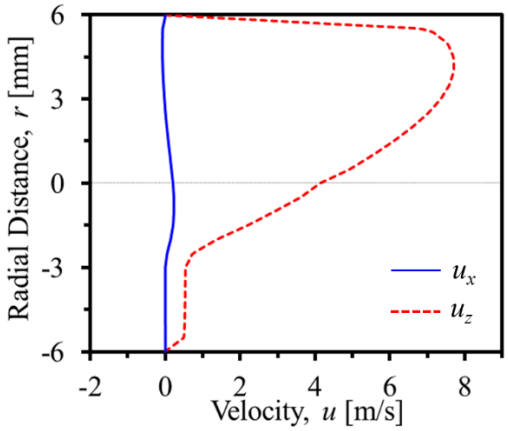

(c)

Figure 3.1-6 Longitudinal (u_z) and lateral (u_x) velocity profiles along the vertical centerline of the cross-section of the tube for (a) plug flow (J_L=0.9, J_G=0.5), (b) wavy flow (J_L=0.14, J_G=2.65) and (c) slug flow (J_L=1, J_G=5)

In order to ensure the simulation results independent of mesh size, a change in pressure gradient was calculated while increasing the number of meshes. The mesh count was increased until the computed value of the current case was within less than 3% of the previous case. Figure 3.1-7 shows a converging trend of the absolute value of the pressure gradient with the mesh number for air-water plug flows. Since there were no significant changes in the pressure gradient achieved from 691,200 cells to 1,097,600 cells, 691,200 cells was chosen for the entire simulations in this study.

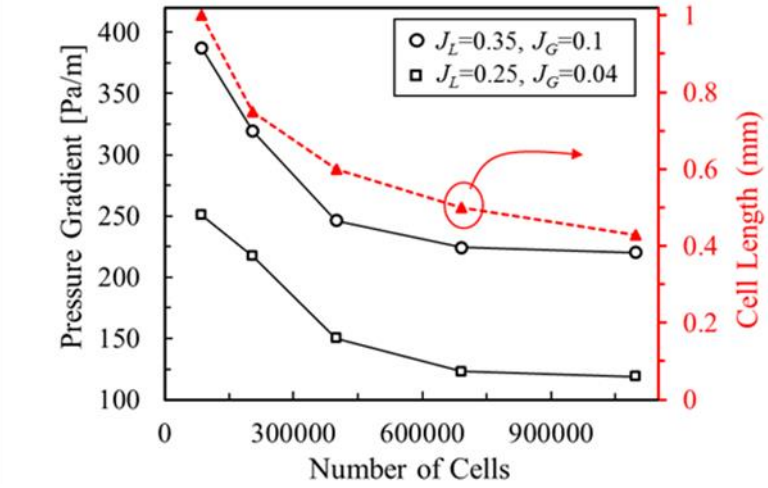

Figure 3.1-7 Grid dependency of the computational results for air-water plug flow

Figure 3.1-8 shows the various computed two-phase flows for the same superficial velocities used in Fig. 3.1-2. The red and blue color represents liquid and gas phases, respectively. It is indicated in Fig. 3.1-8 that the stratified, wavy, plug, slug, and annular flows were well captured in numerical simulation according to their classical definitions described earlier. It is also seen that the experimentally-observed flow patterns (Fig. 3.1-2) are consistent with the computed flow patterns (Fig. 3.1-8) for the same set of superficial velocities.

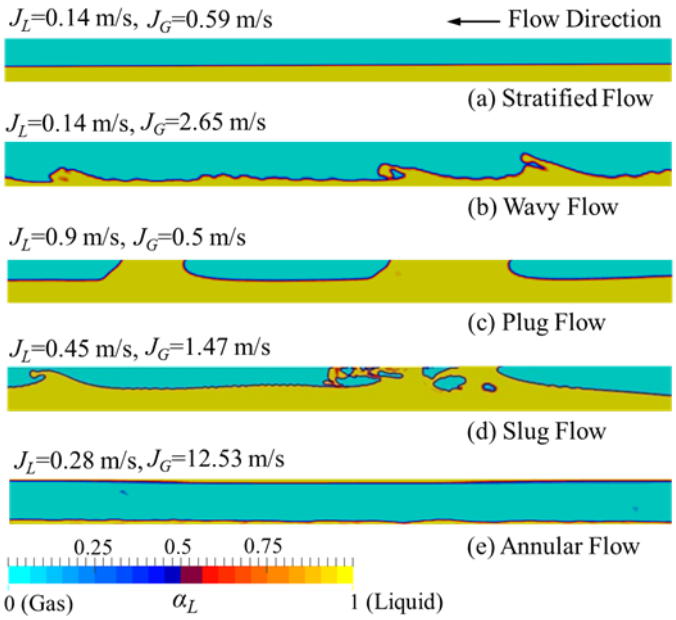

Figure 3.1-8 Computed two-phase flows using the same superficial velocities used in Fig. 3.1-2

It is worth noting that a perfect bubbly flow requires much finer mesh in a larger region of the computational domain to capture tiny bubbles which makes the computational time too long. Therefore, the bubbly flow regime is not considered in the present study.

Table 3.1-2 summarizes the result of nine selected data points from experimental visualization and numerical simulations having the same set of superficial velocities. It is seen that the experimentally-observed flow patterns are in accord with the numerical simulations. The differences only appeared in a case (J_L=0.72, J_G=0.6) near the transition region in which perhaps the length of the tube was not sufficient to develop the expected flow patterns or the cell size, especially near the interface was not fine enough to capture the accurate result. The latter may be improved by applying non-uniform (dynamic) mesh near the interface.

Table 3.1-2 Experimentally-observed and computed flow patterns for the same conditions

J_L	J_G	Exp.	CFD
0.10	0.30	Stratified	Stratified
0.14	0.59	Stratified	Stratified
0.10	3	Wavy	Wavy
0.14	2.65	Wavy	Wavy
0.72	0.60	Slug	Plug
0.90	0.50	Plug	Plug
0.45	1.47	Slug	Slug
1	1.47	Slug	Slug
0.28	12.53	Annular	Annular

In overall, it is concluded that VOF-CSF is capable of capturing the interfacial behavior of two-phase flows and can accurately simulate different two-phase flow patterns. In the following sections, the computed values of void fraction and pressure drop as important parameters of two-phase flows are quantitatively compared with empirical correlations available in literature.

Void fraction (ε) is defined by the ratio of the volume (or area) occupied by gas to the total volume (or area) available for the whole flow. Woldesemayat and Ghajar [114] performed a comprehensive survey to collect void fraction correlations as well as measured void fraction data from literature. They proposed void fraction correlation which could predict all data sets regardless of flow patterns and inclination angles. The void fraction correlation for horizontal flows under atmospheric pressure condition is given by:

$$\varepsilon = \frac{J_G}{J_G\left[1+\left(\frac{J_L}{J_G}\right)^{\left(\frac{\rho_G}{\rho_L}\right)^{0.1}}\right]+7.076\left[\frac{gD\sigma\left(\rho_L-\rho_G\right)}{{\rho_L}^2}\right]^{0.25}}. \tag{3-5}$$

Figure 3.1-9 shows that the time-averaged void fraction of computed two-phase flows are within about ±15% deviation with the correlation proposed by Woldesemayat and Ghajar [114]. The highest void fraction value (about 0.9) is seen for the annular flows. This is expected, since the gas phase occupies most of the tube volume keeping a thin liquid film on the tube wall. On the contrary, low values of void fraction can be seen for plug flows due to an existence of large volume of liquid inside the tube.

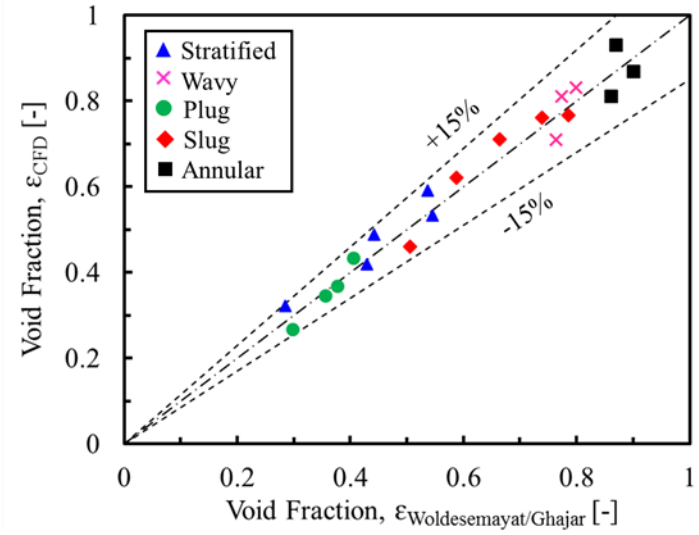

Figure 3.1-9 Comparison of the void fractions of computed two-phase flows with Woldesemayat and Ghajar's [114]

There are plenty of correlations available in open literature to calculate two-phase frictional pressure drop. Tribbe and Muller-Steinhagen [116] compared some of the popular two-phase pressure drop correlations to a large body of data including the combinations of air-water, air-oil, water-steam and many refrigerants. They claimed that the method of Muller-Steinhagen and Heck [115], that is an empirical interpolation between liquid and gas flows, gave the most reliable results among other correlations in literature. The correlation is given by

$$\left(\frac{dp}{dz}\right)_f = C\left(1-x\right)^{1/3} + Bx^3, \tag{3-6}$$

where

$$C = A + 2(B - A)x. \tag{3-7}$$

In the above equation, x is vapor quality and is defined as the ratio of vapor mass flow rate to total mass flow rate. It is normally used for phase change (e.g., boiling and condensation) flows. However, for isothermal (non-boiling or non-condensing) two-phase flows, x is calculated by

$$x = \frac{\rho_G Q_G}{\rho_G Q_G + \rho_L Q_L}. \tag{3-8}$$

A and B in [Eqs. (3-9)-(3-10)] are the frictional pressure gradients assuming all the flow in liquid phase $(dp/dz)_L$ and all the flow in gas phase $(dp/dz)_G$ and are computed as

$$A \equiv \left(\frac{dp}{dz}\right)_L = f_L \frac{2G^2}{D\rho_L}, \tag{3-9}$$

$$B \equiv \left(\frac{dp}{dz}\right)_G = f_G \frac{2G^2}{D\rho_G}, \tag{3-10}$$

where G is mass flux and is calculated as:

$$G = \frac{\rho_L Q_L + \rho_G Q_G}{A}. \tag{3-11}$$

The friction factors (f) is calculated from [Eqs. (3-12)-(3-13)]:

(i) Laminar flow (Re < 2000):

$$f_L = \frac{16}{\mathrm{Re}_L}, \tag{3-12}$$

$$f_G = \frac{16}{\mathrm{Re}_G}, \tag{3-13}$$

(ii) Turbulent flow (Re > 2000):

$$f_L = \frac{0.079}{\mathrm{Re}_L^{0.25}}, \tag{3-14}$$

$$f_G = \frac{0.079}{\mathrm{Re}_G^{0.25}}, \tag{3-15}$$

where Reynolds number is calculated from the superficial velocity and is given by

$$\mathrm{Re} = \frac{\rho JD}{\mu}. \tag{3-16}$$

Note that, the respective densities, superficial velocities and dynamic viscosities of the liquid and gas phases should be used in Eq. (3-16).

Figure 3.1-10 indicates that the Muller-Steinhagen and Heck's [115] correlation predicts the pressure gradients for computed two-phase flows within a deviation of ±20%. It is apparent that the annular flows have the largest pressure gradients. This is due to an extremely high velocity of the gas flow which cause high shear stresses on gas-liquid interface. However, as it appears in Fig. 3.1-10, slug flows also could cause a large pressure gradient when the velocity is relatively high. Generally, slug flow happens at combinations of a wide range of the gas and liquid superficial velocities as compared to other flow regimes. This can be confirmed in flow pattern maps where slug flow occupies a relatively larger zone (Fig. 3.1-3). Moreover, in stratified flows, a low velocity of gas and liquid phases leads to a relatively lower pressure gradient as seen in Fig. 3.1-10.

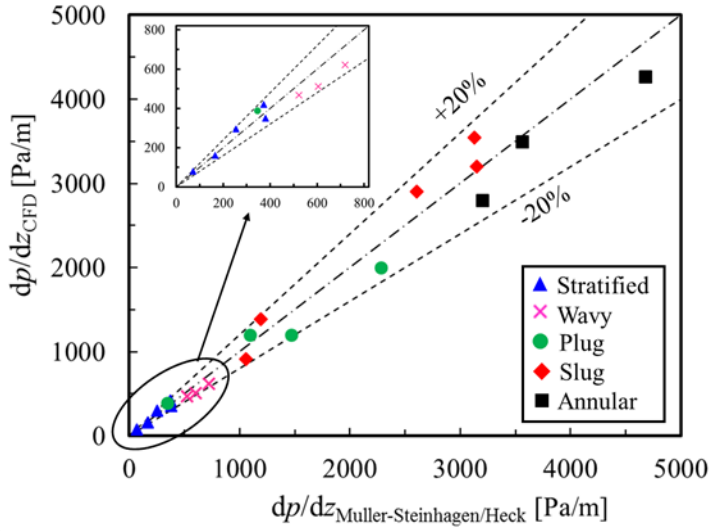

Figure 3.1-10 Comparison of the computed pressure drops with Muller Steinhagen and Heck's [115] correlation

3.1.3 Summary

Experimental visualization of adiabatic two-phase (air-water) flow in a horizontal tube was carried out. The observed flow patterns of stratified, wavy, plug and slug flows were found to be generally consistent with Mandhane's [47] flow map except annular flow which was observed at relatively lower gas superficial velocities and also wavy flows were obtained for relatively higher water superficial velocities in the experiment. The differences can be attributed to different experimental conditions (e.g., tube diameter), complex behavior of two-phase flow near the transition zone and subjective classification of observed flow regimes by researchers. Computational fluid dynamic (CFD) simulations were also performed based on the VOF-CSF method using OpenFOAM to capture different two-phase flow regimes in a horizontal tube. Experimental and numerical results were generally consistent in the qualitative prediction of flow regimes. In addition, the comparison of the hydrodynamic features (e.g. void fraction, pressure drop) of the simulated cases showed acceptable agreement with the selected empirical correlations in literature.

3.2 HORIZONTAL PLUG/BUBBLE FLOWS UNDER REDUCED GRAVITIES

In this work, a computational approach was conducted to analyze intermittent features of gas-liquid plug/bubble flows under various gravity levels ranging from $10^{-4}g_o$ (micro) to $2g_o$ (hyper). The predictive accuracy of the computational model was validated at normal gravity with our previous experimental observations and available correlations in literature. Then, the gravitational influence on flow pattern, void fraction, bubble translational velocity, slip ratio and pressure drop is discussed. It is worth noting that, a plug flow regime was selected as baseline conditions at normal gravity. Since an annular flow is highly inertia-dominated, the influence of gravity might be trivial as compared to any other flow regimes. Moreover, a stratified flow does not occur at reduced gravity (e.g. microgravity). Intermittent flows (plug and slug) may be best suited to this study because bubbles exist at all gravity conditions. However, a horizontal slug flow regime inherently contains distorted gas slugs in random shapes with tiny dispersed bubbles or droplets which make the data reduction somewhat difficult and also gravity might dramatically change the flow pattern. Therefore, a plug flow at normal gravity was chosen for the baseline condition and comparisons.

3.2.1 Computational model

Table 3.2-1 provides the system dimensions and ranges of the operational conditions used for the CFD simulations. The two-phase flows require enough time or length to fully develop. Due to the inherent transient nature of plug/bubble flow, the two-phase hydrodynamic features (e.g. void fraction, pressure drop) are fluctuating with time. Therefore, the reported data in this study are the time-averaged values over an adequate

time period. As listed in Table 3.2-1, the water flow is turbulent (Re >2000), while the oil and air flows are laminar (Re <2000). The computational grid system is the same as shown in Figure 3.1-4. The tube diameter of 12 mm (Bo=19.6) rather than mini/micro scales helps to investigate the strong effect of body force (gravity) on the two-phase flows.

Table 3.2-1 System dimensions and operational conditions

Parameter	Value
Diameter, D [mm]	12
Length, L [mm]	1600
Water superficial velocity, J_L [m/s]	0.25~1.2
Oil superficial velocity, J_L [m/s]	0.25~0.35
Air superficial velocity, J_G [m/s]	0.04~0.6
Mixture superficial velocity, J_m [m/s]	0.29~1.47
Volumetric fraction of gas, β_G [-]	0.14~0.68
Superficial Reynolds number of water, Re_{sL} [-]	3,067~10,613
Superficial Reynolds number of oil, Re_{sL} [-]	75~105
Superficial Reynolds number of air, Re_{sG} [-]	26~394

A plug flow is characterized by a periodic appearance of elongated bubbles (gas plug) moving on the top of the liquid film separated by a liquid bridge (liquid plug) [Fig. 3.2-1(a)]. Figure 3.2-1[(b)-(c)] show favorable qualitative agreement between experimentally-observed and numerically-obtained plug flows at different superficial velocities in terms of the visible distribution of the phases and the shape and size of the elongated bubbles (gas plugs).

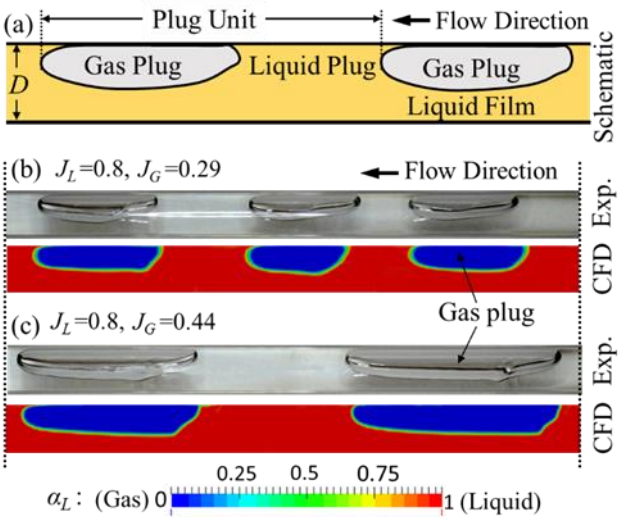

Figure 3.2-1 (a) Schematic of plug flow structure and [(b)-(c)] comparison of the experimentally-observed and numerically-simulated air-water plug flows at normal gravity in a horizontal tube of *D*=12 mm

Furthermore, translational velocity of bubbles (gas plugs) were computed for seventeen simulated air-water flows with various mixture superficial velocities (sum of the liquid and gas superficial velocities) and were compared with an empirical correlation proposed by Thaker and Banerjee [117] The correlation is a linear function of the mixture superficial velocity and is given by

$$u_t = C_o J_m + u_d , \tag{3.17}$$

where u_t is a bubble translational velocity, u_d is a drift velocity of bubble in a stagnant liquid, J_m is a mixture superficial velocity, and C_o refers to a weighted velocity/liquid fraction distribution parameter. Thaker and Banerjee [117] suggested the following for plug flow:

$$C_o = 1.005,\ u_d = 0.19 \quad \text{for } \mathrm{Fr}_m \le 3.5, \tag{3-18}$$

$$C_o = 1.192,\ u_d = 0 \quad \text{for } \mathrm{Fr}_m > 3.5, \tag{3-19}$$

where Froude number (Fr_m) is defined as

$$Fr_m = \frac{J_m}{\sqrt{gD}} \cdot \tag{3-20}$$

Figure 3.2-2 shows that the above correlation slightly overestimates most of the present CFD results of the bubble translational velocities within an MAE value of 5.1%.

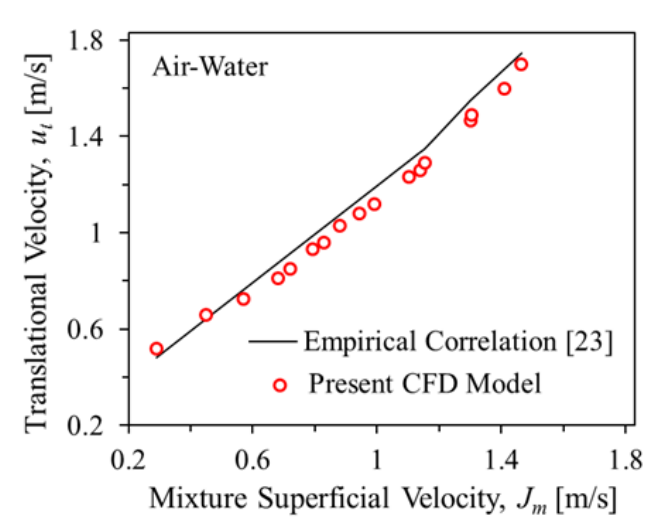

Figure 3.2-2 Comparison of the simulated translational velocity of bubble with an empirical correlation [117]

To understand the effect of a gravitational field on two-phase flow, CFD simulations were performed for an air-water and air-oil flow under eleven different gravitational field strengths: $10^{-4}g_o$ (microgravity), $0.17g_o$ (Moon), $0.38g_o$ (Mars), $0.6g_o$, $0.8g_o$, $0.9g_o$, g_o (=9.81 m/s^2, earth), $1.1g_o$, $1.2g_o$, $1.5g_o$, $2g_o$ (hyper). For each gravity condition, two different sets of superficial velocities of J_L=0.35, J_G=0.1 (β_G=0.22) and J_L=0.25, J_G=0.04 (β_G=0.14) were used. The selected velocities create a plug flow at normal gravity. The effect of gravitational strength on flow pattern, void fraction, bubble translational velocity, slip ratio and pressure drop were investigated and are discussed below.

3.2.2 Results

Figure 3.2-3 shows the flow patterns (side and cross-sectional views) of air-water [Fig. 3.2-3(a)] and air-oil [Fig. 3.2-3(b)] flows under five selected gravities for a case of J_L=0.35, J_G=0.1 (β_G=0.22). It is seen that gravity plays a substantial role on the bubble size, shape and distributions. As gravity is increased, resulting in augmented buoyancy force, the less dense fluid (gas) migrates to the upper region of the tube such that bubbles attach to the top wall forming gas plugs. In such cases, bubbles tend to be flattened and elongated. On the other hand, at microgravity, axisymmetric bubbles exist at almost the center of the tube. In this case, the buoyancy force is small enough to detach bubbles from the tube wall creating thin liquid film at the top and bottom of the tube.

Comparing Figs. 3.2-3(a) and (b) at low gravities (e.g. $0.17g_o$ and $10^{-4}g_o$) shows that the bubbles in an air-water flow are more spherical than those in air-oil flow where the bubbles are more stretched. This is due to the larger surface tension of water (σ =0.072 N/m) in comparison with oil (σ =0.034 N/m) which tends to keep the minimum surface area (spherical shape). This is more apparent at microgravity where the buoyancy is almost gone and surface tension become dominant.

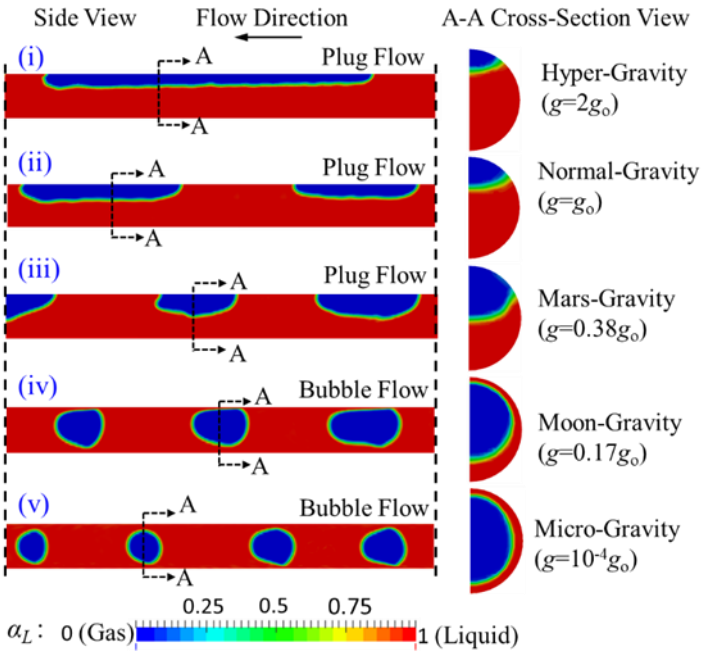

(a)

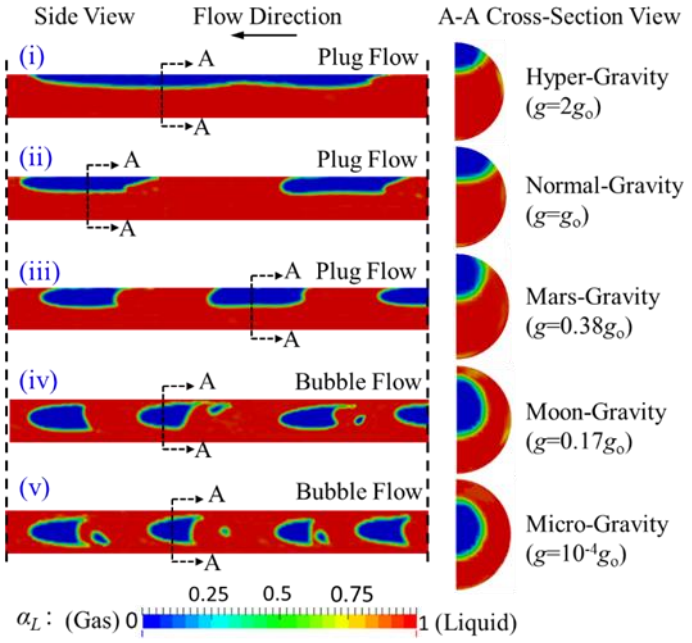

(b)

Figure 3.2-3 Instantaneous flow patterns of (a) air-water and (b) air-oil flows under different gravity levels for J_L=0.35 and J_G=0.1 (β_G=0.22)

To explain the bubble detachment from the tube wall which leads to flow pattern transition from plug to bubble flow under reduced gravities, a simplified theoretical analysis is performed at a tube cross section. The analysis assumes that the momentum effect of radial velocity distribution on the bubble shape is negligible as compared to capillary and buoyancy forces. Figure 3.2-4 renders a tube cross-sectional view under various bubble conditions. Figure 3.2-4(a) shows a deformed bubble which is attached to the top wall (plug flow); Fig. 3.2-4(b) shows the critical condition where a bubble is about to detach from the tube wall; and Fig.3.2-4(c) also shows a detached bubble which is located at the center of the tube (bubble flow). Buoyancy force (F_b) pushes the bubble against the top wall and deform the bubble while capillary force (F_c) tends to maintain the bubble shape to have a minimum surface area (spherical shape).

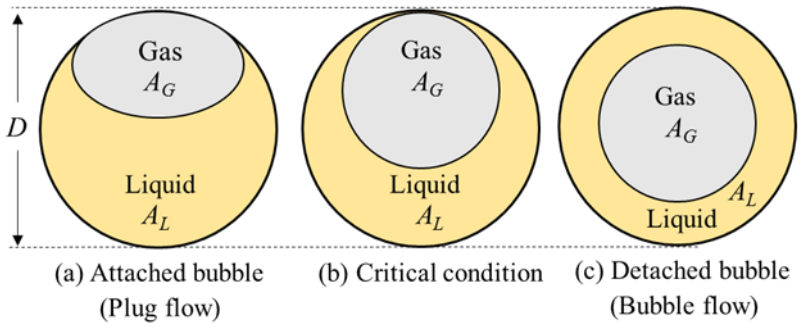

Figure 3.2-4 Simplified cross-sectional views of (a) attached bubble and (b) critical and (c) detached bubble

Buoyancy force (F_b) pushes the bubble against the top wall and deforms the bubble while capillary force (F_c) tends to maintain the bubble shape to have a minimum surface area (spherical shape). Buoyancy force per length (at a cross-section) is expressed by

$$F_b = \left(\rho_L - \rho_G\right) g A_G = \left(\rho_L - \rho_G\right) g \varepsilon A = \left(\rho_L - \rho_G\right) g \varepsilon \left(\frac{\pi}{4}\right) D^2, \qquad (3\text{-}21)$$

where A_G is the cross-sectional area occupied by gas phase and is calculated using void

fraction (i.e. $A_G=\varepsilon A$). The volumetric void fraction (ε) is calculated as an area-average value over a cross-sectional area. The capillary force per length is also given by

$$F_c = \sigma\left(1-\varepsilon\right)^{\frac{1}{2}}. \tag{3-22}$$

The term $(1-\varepsilon)^{1/2}$ is introduced to determine the effective surface tension force over the wetted perimeter using the separated two-phase models described by Tabatabai and Faghri [118]. Bubble detaches from the wall if the capillary force overcomes the buoyancy force as below

$$F_c > F_b. \tag{3-23}$$

Using Eqs. (3-21) and (3-22) in Eqn. (3-23), we have

$$\sigma\left(1-\varepsilon\right)^{\frac{1}{2}} > \left(\rho_L-\rho_G\right)g\varepsilon\left(\frac{\pi}{4}\right)D^2. \tag{3-24}$$

Rearranging Eq. (3-24) yields the following criteria to determine the critical gravity as a condition for bubble detachment (flow pattern transition from plug to bubble flow) as below

$$g < \frac{4\sigma}{\left(\rho_L-\rho_G\right)\pi D^2}\frac{\left(1-\varepsilon\right)^{\frac{1}{2}}}{\varepsilon}\left(=g_d\right). \tag{3-25}$$

Equation (3-25) implies that the critical gravity [right hand side of Eq. (3-25) that is g_d] is a function of fluid properties (ρ_L, ρ_G and σ), tube diameter (D) and void fraction (ε). The choice of a void fraction correlation is sorely important. Woldesemayat and Ghajar [114] provided a comprehensive summary and comparison of the available void fraction correlations. They ultimately proposed an improved drift-flux correlation that is suggested to be applicable to all flow conditions regardless of flow patterns and inclination angles. Their suggested correlation is used in this study which for a horizontal flow under

atmospheric condition is given by

$$\varepsilon = \frac{J_G}{J_G\left[1+\left(\frac{J_L}{J_G}\right)^{\left(\frac{\rho_G}{\rho_L}\right)^{0.1}}\right]+4.21\left[\frac{gD\sigma\left(\rho_L-\rho_G\right)}{\rho_L{}^2}\right]^{0.25}}. \tag{3-26}$$

Note that the present CFD results for the void fraction were satisfactorily compared with those predicted by the above correlation [Eq. (3-25)] in Fig. 3.1-5 (a). Table 3.2-2 lists the calculated critical gravities (g_d) using Eqs. (3-25) and (3-26) for each simulated flow condition in this study.

Table 3.2-2 Calculated critical gravities for bubble detachment using Eqs. (3-31) and (3-32)

Fluids	J_L (m/s)	J_G (m/s)	β_G	g_d (m/s^2)
Air-water	0.35	0.10	0.22	$0.30g_o$
Air-water	0.25	0.04	0.14	$0.47g_o$
Air-oil	0.35	0.10	0.22	$0.17g_o$
Air-oil	0.25	0.04	0.14	$0.25g_o$

It is seen from Fig. 3.2-5(a) for air-water flow at β_G=0.22 that bubbles detached from $0.38g_o$ (Mars) to $0.17g_0$ (Moon), while Eq. (3-25) satisfactory predicts the critical gravity of $0.30g_o$ (see 1st row in Table 3.2-2), which is confirmed by additional CFD simulations in Fig. 3.2-5(a) showing a plug-bubble flow at $0.30g_o$. Figure 3.2-5(b) also shows that for air-oil flow at β_G=0.22, bubbles detached between $0.38g_o$ (Mars) and $0.17g_0$ (Moon), whereas Eq. (3-25) predicts the critical gravity of $0.17g_o$ (see 3rd row in Table 3.2-2) that is further confirmed by additional CFD results in Fig. 3.2-5(b) where a plug-bubble flow exists at $0.20g_o$ which is close to the theoretical prediction ($0.17g_o$).

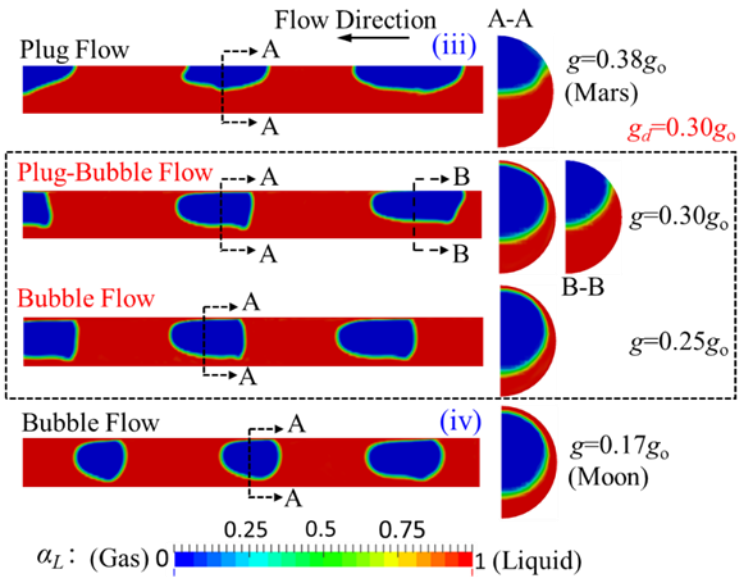

(a)

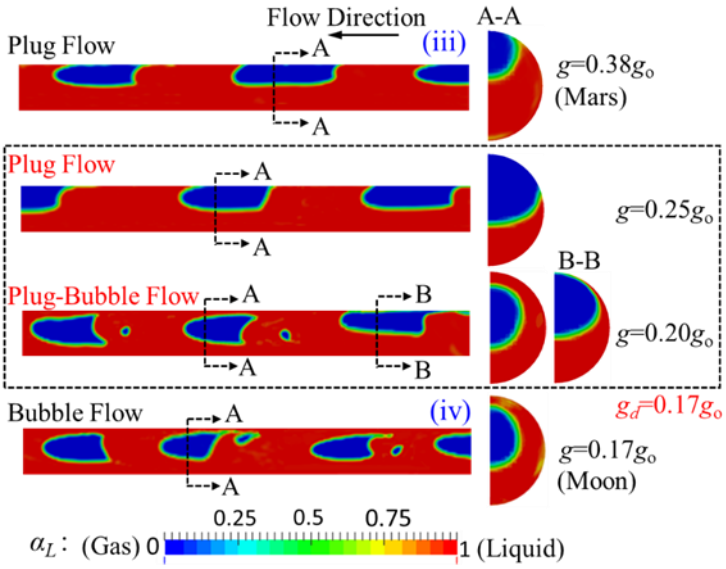

(b)

Figure 3.2-5 CFD results near the flow pattern transition (bubble detachment) at J_L=0.35 m/s and J_G=0.1 m/s (β_G=0.22) for (a) air-water and (b) air-oil flow

Void fraction

Figure 3.2-6(a) shows a radial distribution of a time-averaged void fraction (ε) for an air-water flow at five selected gravity levels for a case of β_G=0.22. It is clearly observed

that the void fraction distribution is axisymmetric under microgravity (g=$10^{-4}g_o$) and a maximum void fraction appears at the middle of the tube that is the gas bubble stays at the center of the tube. The liquid film below the gas plug/bubble gets thicker with increasing gravity, resulting in a larger void fraction at the top region of the tube and an expanded bottom region with zero void fraction. Moreover, for micro ($10^{-4}g_o$) and Moon-gravity ($0.17g_o$), the void fraction is always zero at both the top and bottom regions meaning the bubbles are completely detached at those gravity levels.

Figure 3.2-6(b) demonstrates the fluctuation of the cross-sectional void fraction of an air-water flow under five selected gravities for the case of β_G=0.22 where t and T are the real and total times, respectively. It is seen that the peak value of the void fraction falls down by increasing the gravity level. This is observable from the cross-sectional views in Fig. 3.2-3(a) where the gas plug/bubble expands and occupies larger area of the cross-section by reducing the gravity. It is also evident from Fig. 3.2-6(b) that the cross-sectional void fraction are more frequent at lower gravities. This is explained from the side views of Fig. 3.2-3(a) in which at a certain portion of the tube length, the number of the gas plug/bubble unit increases by decreasing the gravity resulting in more frequent peaks of the void fraction.

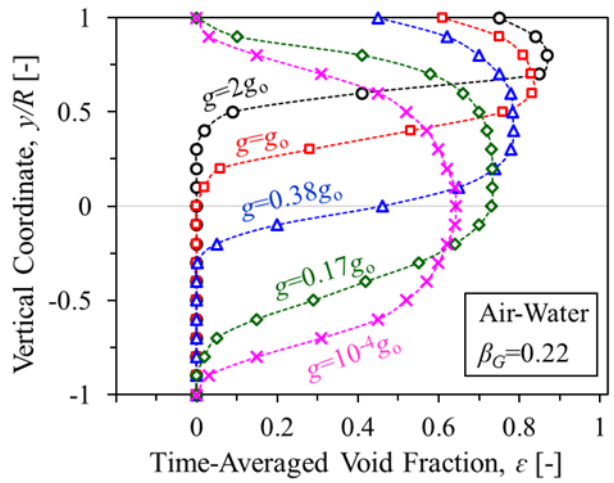

(a)

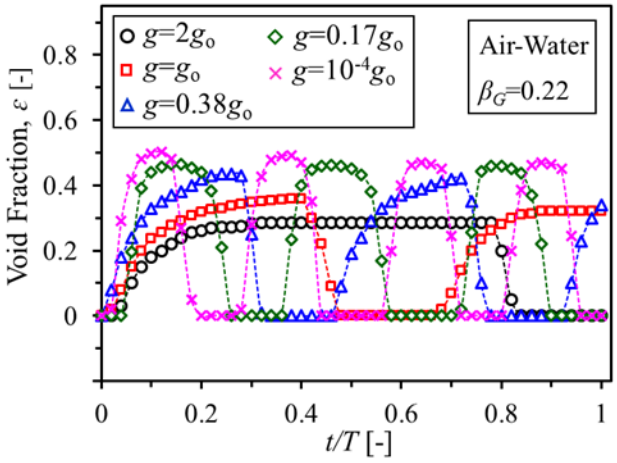

(b)

Figure 3.2-6 (a) Radial distribution of a time-averaged void fraction and (b) fluctuation of cross-sectional void fraction for air-water flow under five selected gravities for J_L=0.35 m/s and J_G=0.1 m/s (β_G=0.22)

Figure 3.2-7 shows the variation of time-averaged cross-sectional void fraction under different gravity levels for all of the simulated cases. It is seen that the time-averaged void fraction slightly decreased as gravity level increases which means the volume occupied by gas phase is slightly expanded when gravity is reduced. Close scrutiny reveals a significant change in the slope of the void fraction near the critical gravity (marked as green bar) because of a bubble detachment (Table 3.2-2 and Fig. 3.2-5). The small vertical marker in

each profile indicates the predicted critical gravity for bubble detachment (g_d) calculated from Eq. (3-31).

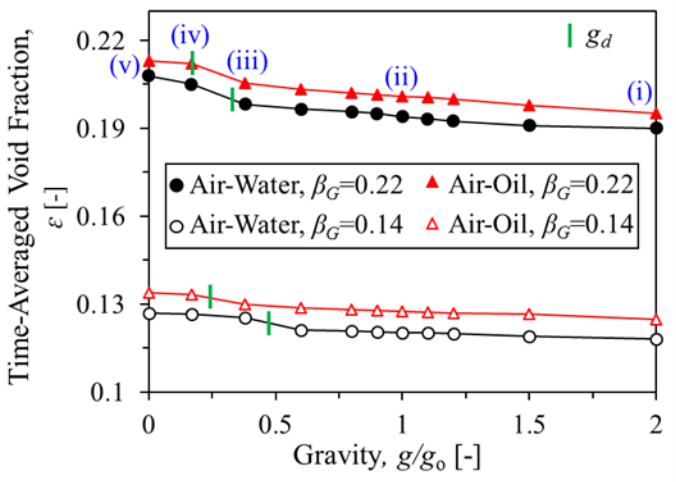

Figure 3.2-7 Time-averaged cross-sectional void fraction under different gravity levels

Translational velocity of bubble

Figure 3.2-8 shows that gravitational magnitude does not substantially affect the bubble translational velocity for a two-phase horizontal flow. The bubble velocity, however, generally increases with increasing gravity except a sudden drop due to the bubble attachment to the wall near the critical gravity (marked as green bar). The overall increasing trend of bubble velocity is attributed to a slight decrease in the void fraction (Fig. 3.2-7) at the same superficial velocity ($J_G=\varepsilon u_G$).

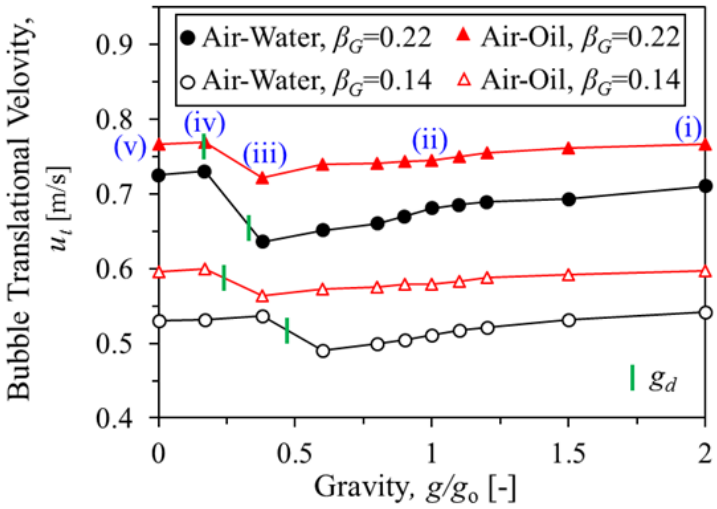

Figure 3.2-8 Effect of gravity on gas plug/bubble translational velocity for air-water and air-oil flows

Slip ratio

An interfacial shear stress (τ_i) in two-phase flow is attributed to a slip ratio (a ratio of a gas velocity to a liquid velocity $\equiv u_G/u_L$) which is computed from a time-averaged void fraction (ε) and a volumetric fraction of the gas flow ($\beta_G=J_G/J_m$):

$$S = \frac{(1-\varepsilon)\beta_G}{\varepsilon(1-\beta_G)}. \tag{3-27}$$

Figure 3.2-9 shows the variation of the slip ratio under different gravity levels. It is shown that the slip ratio is increased by increasing the gravity for all flow conditions and a significant slope change is seen at a critical gravity (marked as green bar) caused by bubble detachment. The increasing trend of the slip ratio by increasing the gravity is due to a decrease in the void fraction or gas volume (Fig. 3.2-7) at the same gas flow rate leading to an increase in overall gas velocity (u_G) i.e. a reduced drag force of the bubble flow exerted by the liquid flow. On the other hand, a decreased void fraction (gas volume) leads to an increase in liquid flow volume resulting in a decrease in the liquid velocity (u_L).

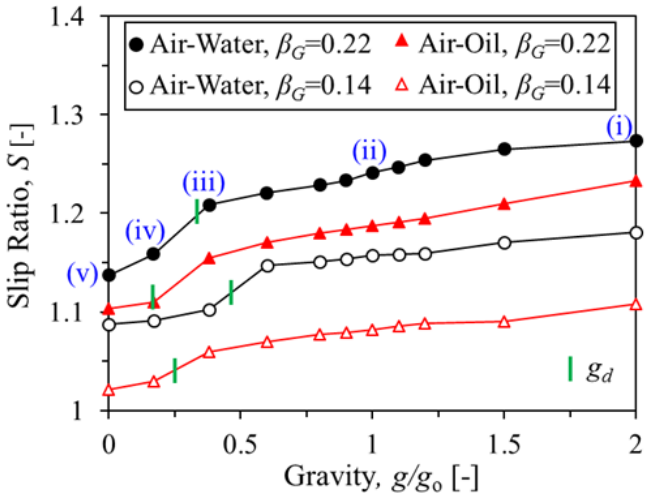

Figure 3.2-9 Influence of gravity on slip ratio for air-water and air-oil flow

Pressure drop

Figure 3.2-10 shows a ratio of the pressure drop of the two-phase flows for various gravity levels to that for normal-gravity (g_o). The pressure drop ratio $\Delta p/(\Delta p)_{go}$ shows a complex trend by changing gravity from microgravity ($10^{-4}g_o$) to hyper ($2g_o$) as a consequence of the complex interactions of the two-phase flows which is greatly affected by a gravitational force However, it is seen that for all the simulated cases, minimum pressure drop occurs at normal or around normal gravity. Choi et al. [67] from their experimental data of air-water horizontal flows, also reported a larger pressure drop for both hyper gravity ($2g_o$) and microgravity than that at normal gravity.

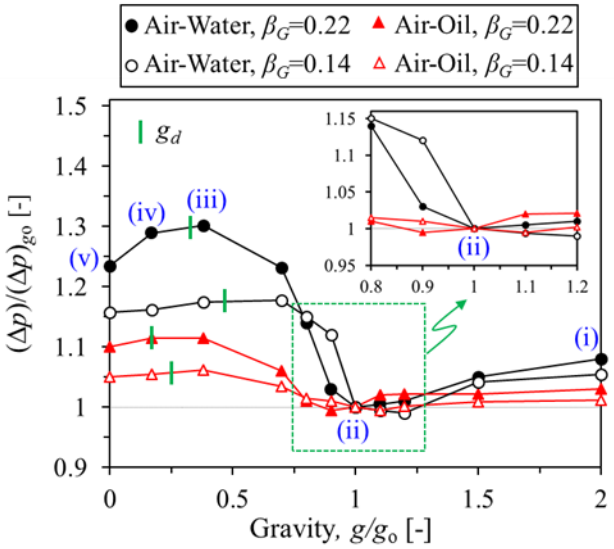

Figure 3.2-10 Ratio of pressure drop at various gravity levels to that at normal gravity

In a horizontal flow, with the absence of phase change (boiling and condensation), the total pressure drop (Δp) is only caused by friction (Δp_f) because the hydrostatic pressure drop (Δp_g) and the momentum (acceleration) pressure drop (Δp_m) are zero. The fluid's friction is governed by shear stress (τ). In a two-phase flow, the shear stress is comprised of two terms: interfacial shear stress (τ_i) and wall shear stress (τ_w). The latter is mainly determined by the liquid phase only due to a much larger viscosity of liquid to that in gas phase. Therefore, the pressure drop is written by

$$\Delta p \approx \tau_{w,L} A_{w,L} + \tau_i A_i . \tag{3-28}$$

where $A_{w,L}$ and A_i are respectively the effective surface area that is contributed to liquid-wall and interfacial shear stress. Equation (3-28) implies that in a horizontal two-phase flow without phase-change, the pressure drop is determined by liquid-wall shear stress (τ_{wL}) and interfacial shear stress (τ_{wi}).

Two major competing effects are attributed to the intriguing behavior of the pressure drop in Fig. 3.2-10: first, as the gravity is reduced, the liquid flow area is decreased

due to the increased void fraction (Fig. 3.2-8) which accelerates the liquid phase, resulting in a higher liquid-wall shear stress (τ_{wL}) leading to a larger pressure drop; Secondly, the interfacial shear stress (τ_{wi}) is decreased due to the reduced slip ratio (Fig. 3.2-9), resulting in a lesser pressure drop. The overall variation of the pressure drop with a maximum and minimum is determined by the relative magnitude of two competing effects of gravity.

Here, we briefly explain the pressure drop variation of the air-water flow for β_G=0.22 (solid circles in Fig. 3.2-10) while the other cases are believed to obey the same physics. Let us consider the five selected gravities shown in Fig. 3.2-5(a) as marked by [(i)-(v)] in Fig. 3.2-10. It is seen that generally the pressure drop is decreased slightly by reducing the gravity (due to the reduction of interfacial shear stress) except from normal (g_o) to mars ($0.38g_o$) where the pressure drop is increased due to the significant increase in the liquid-wall shear stress (τ_{wL}) caused by a liquid acceleration.

Figure 3.2-11 compares the instantaneous vertical distribution of the axial velocity at a mid-cross-section of a bubble for normal (g_o) and Mars ($0.38g_o$) gravities. Note that a wall shear stress is proportional to the velocity gradient near the wall. The magnified velocity profiles near the wall regions clearly shows the larger velocity gradients (local wall shear stress) under Mars gravity ($0.38g_o$) compared to that at normal gravity (g_o) that is attributed to the different shape of gas plugs induced by change in gravity. Under Mars gravity, the gas plugs are less compressed and expanded as compared to that in normal gravity where the gas plugs became more stretched. The expanded bubbles under Mars gravity locally chocks the liquid flow area leading to a significant increase in the liquid velocity (liquid acceleration) as seen in Fig. 3.2-11 and accordingly a larger liquid wall shear stress.

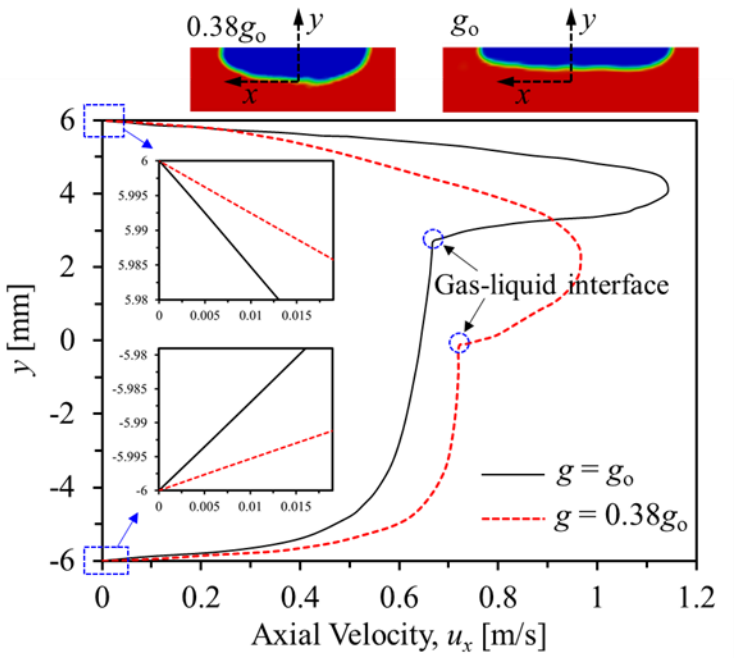

Figure 3.2-11 Vertical distribution of axial velocity at a mid-cross-section of a bubble for normal (g_o) and Mars ($0.38g_o$) gravities for air-water flows at J_L=0.35 m/s and J_G=0.1 m/s (β_G=0.22)

3.2.3 Summary

A systematic computational study was carried out to investigate the effect of gravity on horizontal two-phase plug/bubble flows. Intermittent characteristics of air-water and air-oil mixture flows were analyzed under various gravity levels. The main conclusions are:

- Vertical distribution of a void fraction at a tube cross-section is axisymmetric at microgravity ($10^{-4}g_o$) with a maximum void fraction appears at the tube axis and zero value void fraction (liquid film) at the tube wall. Increasing gravity level pushes gas bubbles toward the upper region of the tube causing the bottom region with zero void fraction (liquid film).
- The time-averaged void fraction is slightly increased by reducing gravity level. That is, the volume occupied by gas phase is slightly expanded at reduced gravity.

- By reducing the gravity, two-phase flow pattern changes from plug to bubble flow as a result of bubble detachment from the tube wall.
- The slip ratio is decreased by reducing the gravity level due to an increase in the void fraction which affects the interfacial momentum transfer between the phases.

The two-phase pressure drop for all of the simulated cases considered in this study is minimum around normal gravity as a result of two major competing effects of reduced slip ratio (decreased interfacial shear stress) and liquid acceleration (increased wall shear stress).

3.3 VERTICAL UPWARD SLUG FLOWS UNDER REDUCED GRAVITIES

The slug flow is characterized by a periodic appearance of slug units. Each slug unit contains an elongated bullet-shaped bubble with a quite similar diameter of the tube, called "Taylor bubble" or "gas slug", and a liquid region that may contains small uniformly dispersed bubbles, called "liquid slug". Such a slug flow is found in many applications such as phase change heat exchangers (condenser and evaporator), gas-lift pumps, oil–gas pipelines, and nuclear reactor cooling. The flow field in the slug flow is complex and the flow field around an individual Taylor bubble is the key to the understanding of the slug flow.

This work investigates the effect of gravitational strength on hydrodynamics of intermediate-scale Taylor bubble in vertical upward slug flow. The computational geometry is the one that is shown in Fig. 3.1-4. However, here the gravitational field was also applied opposite to the flow direction to create an upward flow configuration. Air and water were used as the working fluids and two different sets of superficial velocities (J_L=0.05, J_G=0.15 m/s; and J_L=0.15, J_G=0.15 m/s) were carefully selected to create laminar slug (Taylor bubble) flows. The governing equations were discretized in a three-dimensional computational domain and numerically solved based on the volume of fluid-continuum surface force (VOF-CSF) method presented in Section 2.1. The computational fluid dynamics (CFD) model was validated under normal gravity with existing top performing correlations in literature. To address the space colonization environments, the gravity strength considered in the CFD simulations include $10^{-4}g_o$ (microgravity), $0.17g_o$ (Moon), $0.38g_o$ (Mars), g_o (=9.81 m/s^2, Earth), and $2g_o$ (hyper).

3.3.1 Computational model

While two-dimensional axisymmetric model has been widely used [119, 120] to simulate *vertical* slug flows in *small* diameter tubes (i.e. mini/micro-channels), a symmetric plane (the half-tube model) was considered herein to reduce the computational time, while still capturing the physics of two-phase flow. Table 3.3-1 lists the thermophysical properties of working fluids and tube dimensions used in the simulations.

Table 3.3-1 Thermophysical properties of working fluids and tube dimensions used for the simulations

Parameter	Value
Density of air, ρ_G [kg/m^3]	1
Density of water, ρ_L [kg/m^3]	1000
Kinematic viscosity of air, v_G [m^2/s]	1.480×10^{-5}
Kinematic viscosity of water, v_L [m^2/s]	10^{-6}
Surface tension, σ [N/m]	0.072
Tube diameter, D [mm]	12
Bond number, Bo [-]	19.6
Tube length, L [mm]	1600

In order to assess the computational results for the vertical slug flow, a set of CFD simulations using air and water mixture flows was carried out under normal gravity and the computational results of the bubble rise velocity (u_{TB}) and void fraction (ε) were compared with existing top performing correlations in literature.

In vertical upward con-current slug flow, the bubble rise velocity is an important fundamental parameter affecting two-phase thermo-hydraulic characteristics. A classical model to predict the rising velocity of a Taylor bubble in a vertical slug flow was proposed by Nicklin [121]. The model is a linear function of a mean liquid velocity and is given by

$$u_{TB} = cu_L + u_D, \tag{3-29}$$

where u_{TB} is the rising velocity of a Taylor bubble, u_L is a mean liquid velocity, and u_D is the drift velocity of the bubble due to the buoyancy force in a stagnant liquid. Griffith and Wallis [122] showed that using a mass conservation, the mean velocity of the liquid (averaged over a cross-section of a tube) well ahead of the bubble nose is approximated by the mixture (total) superficial velocity (J). It is worth mentioning that the mixture superficial velocity has been commonly used in Nicklin's model [Eq. (3-29)] for u_L due to its simplicity, particularly in experiments where the mean liquid velocity is very difficult to obtain while the superficial velocities are readily calculated. However, the mean liquid velocity (u_L) used for this study is a mean liquid velocity averaged over the entire liquid volume of a slug unit which produces better agreement between the Nicklin's model and simulation results and the comparison of the results are discussed in Fig. 3.3-10. The coefficient c is a dimensionless coefficient which is approximated by the ratio of a maximum velocity to a mean velocity depending on the liquid velocity profile. It has been accepted as a good approximation for c, 2 for a laminar flow and 1.2 for a turbulent flow [121]. For the drift velocity (u_D) of a Taylor bubble through a stagnant liquid in a vertical tube, Dumitrescu [123] found an expression that is given by

$$u_D = 0.35\sqrt{gD}. \tag{3-30}$$

Bendiksen [124] presented an approximate form for the coefficient c in Eq. (3-29) as a function of Bond number (Bo) that is applicable for a fully-developed laminar flow ahead of the bubble. Rattner and Garimella [125] recently performed experiments on intermediate-scale Taylor flow and proposed an extension of Bendiksen's [124] prediction for c and u_D in Eq. (3-29). In Fig. 3.3-1(a), the numerical results for the rising velocity of

Taylor bubble (u_{TB}) are compared to the predictions of Nicklin et al. [121], Bendiksen [124], and Rattner and Garimella [125]. It is seen that overall, the numerical results agree well with the predictions. The satisfactory mean absolute error (MAE) values of 8.28%, 8.05%, and 7.99% were obtained against the results from Nicklin et al.'s [121], Bendiksen's [124], and Rattner and Garimella's [125] prediction model, respectively.

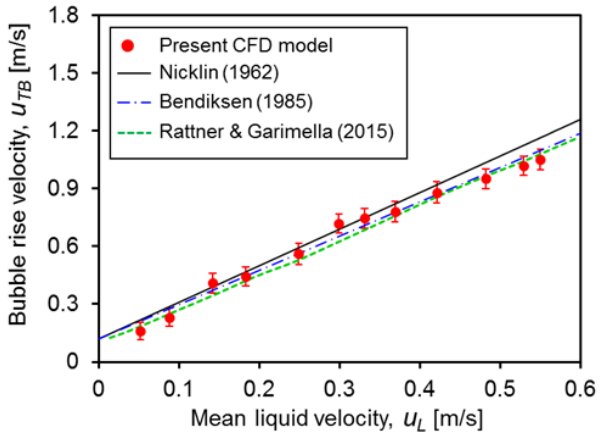

(a)

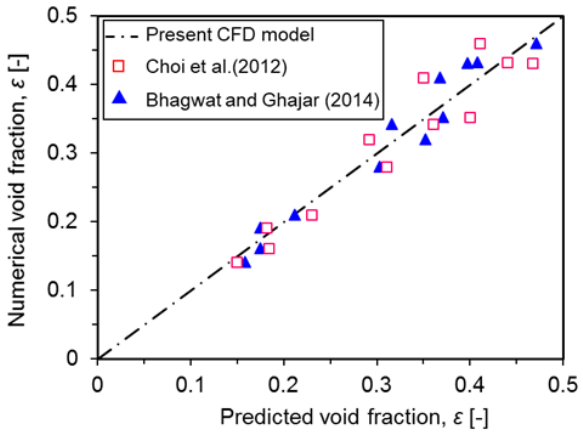

(b)

Figure 3.3-1 Comparison of the numerical results with predicted values under normal gravity: (a) rising velocity of Taylor bubble (u_{TB}); and (b) void fraction (ε)

Void fraction (ε) is the ratio of the volume/area occupied by gas to the total volume/area and is one of the most fundamental and essential parameters for design and

optimization of two phase flow systems. Due to its importance, there exist several void fraction experimental measurements and numerous predictive models for void fraction in literature. Choi et al. [126] proposed an experimentally-validated drift-flux closure model for the prediction of void fraction that is shown to be applicable to a wide range of flow conditions. Bhagwat and Ghajar [127] also proposed a void fraction correlation based on the drift flux model for a wide range of two phase flow conditions and tube diameters. The model was verified using 8255 experimental data from more than 60 sources. Figure 3.3-1(b), shows the comparison of the numerical values of void fraction with those predicted by Choi et al.'s [126] and Bhagwat-and-Ghajar's [127] model. It is indicated that the numerically obtained results are in good agreement with the predicted values. The satisfactory mean absolute error (MAE) values of 8.89% and 7.18% were obtained against the results from Choi et al.'s [126] and Bhagwat-and-Ghajar's [127] correlation.

Two-phase flows are governed by inertia, momentum, friction, gravity (buoyancy force), and interfacial force (surface tension). To understand the effect of gravity on a vertical slug flow, CFD simulations were performed for air-water flows under seven different gravitational strengths with two different sets of inlet superficial velocities as listed in Table 3.3-2.

Table 3.3-2 Gravity and flow conditions used for CFD simulation

Parameter	Values
Normalized gravity, g/g_o (g_o=9.81 m/s^2)	10^{-4}, 0.17, 0.38, 0.80, 1, 1.50, 2
Superficial velocities (m/s)	J_L=J_G=0.15 m/s; J_G=0.15, J_L=0.05 (slug flow)
Bond number	0.00196, 3.332, 7.448, 15.68, 19.6, 29.4, 39.2

The selected superficial velocities created slug flows in the fully-developed region of the vertical tube. Figure 3.3-2 confirms that the selected superficial velocities correspond to the slug flow regime according to the Ansari et al.'s flow map [128]. In this study, the maximum Reynolds number for the liquid and gas flows are 1800 and 122, respectively, implying that the two-phase flows are all laminar.

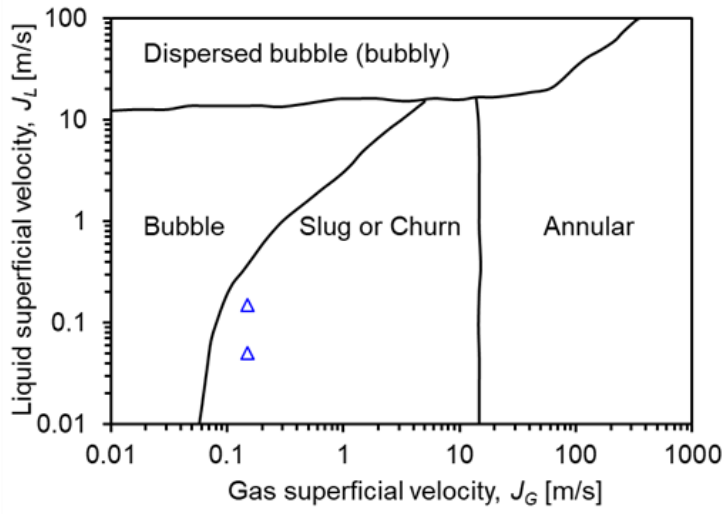

Figure 3.3-2 The selected superficial velocities in Ansari et al.'s [128] flow regime map

3.3.2 Results

Figure 3.3-3 shows the vertical upward air-water flows at J_L=J_G=0.15 m/s under five selected gravities in the fully-developed region ($100 < z/D < 120$). It is shown in Fig. 3.3-3 that the two-phase flows are a slug flow regime characterized by Taylor bubbles and interestingly, the length of the Taylor bubbles are shortened by increasing gravity. This is attributed to a weaker bubble coalescence (easier bubble breakup) at higher gravities where the augmented body force can easily break the long bubble down to smaller ones. The similar results of the shortened bubble at higher gravities was seen at J_L=0.05 m/s and J_G=0.15 m/s.

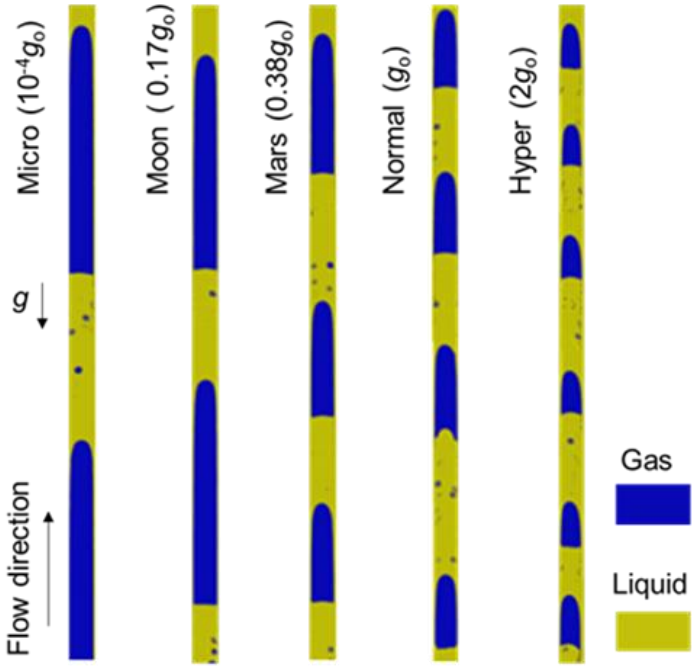

Figure 3.3-3 Computed vertical upward air-water slug flows under five different gravities at J_L=0.15 m/s and J_G=0.15 m/s

Figure 3.3-4 illustrates the liquid streamlines around a single Taylor bubble in the vertical upward slug flows captured in both a fixed frame reference (FFR) and a moving frame reference (MFR, attached to the bubble) under three selected gravities at J_L=0.15 m/s and J_G=0.15 m/s. It is shown in the FFR view that at normal (g_o) and hyper ($2g_o$) gravities, below a certain distance from the bubble nose, the liquid between the Taylor bubble and tube wall flows downward like a falling film in the opposite direction of the bulk flow. This is due to the weaker upward liquid momentum compared to the opposing (downward) body force. Interestingly, at microgravity there exists no falling film that is attributed to the absence of body force. Also, for normal and hyper gravities, as a result of the falling film, strong vortexes (wake region) are observed immediately behind the bubble tail near the tube wall whereas no wake zone is seen at microgravity in the FFR view.

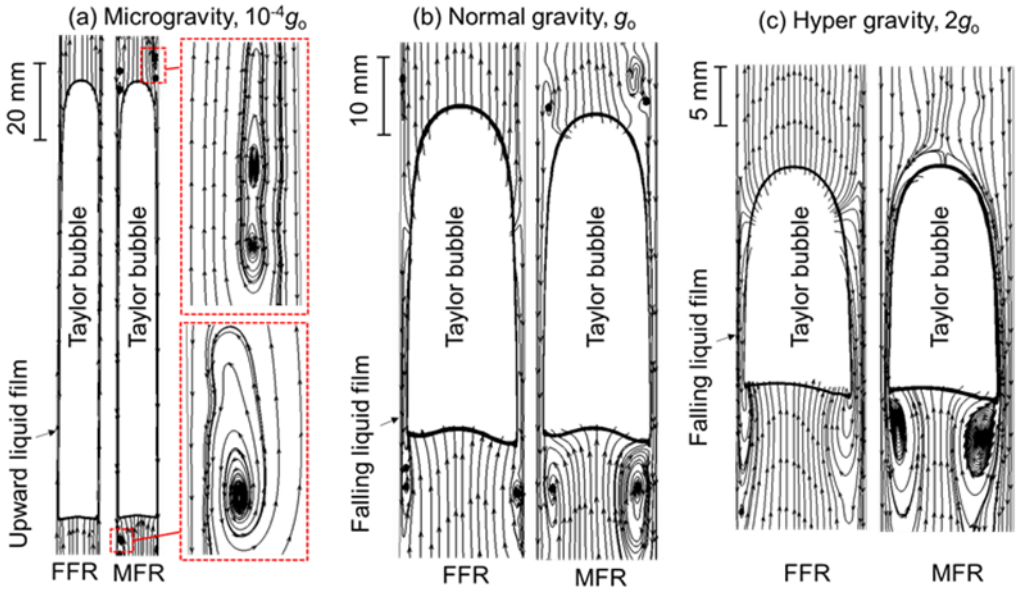

Figure 3.3-4 Streamlines around a single Taylor bubble in a fixed frame reference (FFR) and a moving frame reference (MFR, attached to the bubble) at J_L=0.15 m/s and J_G=0.15 m/s under three selected gravities of (a) micro (10-4go); (b) normal (go); and hyper gravity (2go)

It is also observed in Fig. 3.3-4 that in the MFR view, where the bubble velocity is subtracted from the actual liquid velocity, the liquid film falls down around the Taylor bubbles at all gravities. The primary vortexes in the wake zone of the Taylor bubbles at normal and hyper gravities become more visible in the MFR view. Interestingly, at microgravity, also weak vortexes are observed in front of the nose and behind the tail of the Taylor bubble.

Liquid film around Taylor bubbles is an important key factor to predict the bubble velocity and pressure drop [129, 130]. Figure 3.3-5(a) renders a slug unit with a length of L_{su} consisting of a liquid slug and a Taylor bubble surrounded by a liquid film. Note that the axial distance (z) from the trailing bubble nose is normalized by the total length of the slug unit (L_{su}). Figure 3.3-5(b) shows the variations of the liquid film velocity (u_f) and a dimensionless film thickness (δ/D) of the slug unit under five selected gravities. The liquid

film velocity in the FFR view, was calculated along the horizontal line extended from the mid-point of the thinnest liquid film. The negative velocity means a falling (downward) flow in the direction of gravity. The film thickness (δ) in the liquid slug region and at the tip of the bubble nose is the same as the tube radius.

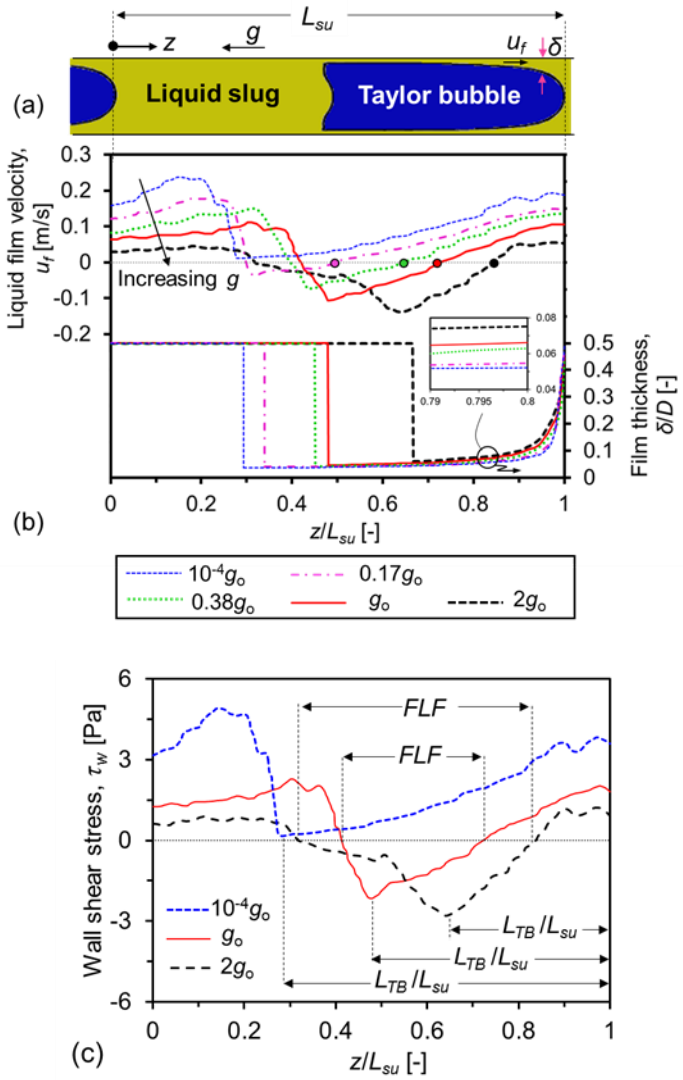

Figure 3.3-5 (a) A slug unit in a vertical upward slug flow; (b) Effect of gravity on liquid film velocity (u_f) and dimensionless film thickness (δ/D) at J_L=0.15 m/s and J_G=0.15 m/s; and (c) instantaneous distribution of wall shear stress along the slug unit three selected gravities

It is also shown in Fig. 3.3-5(b) that in the Taylor bubble region, the stagnation point where the liquid film velocity is zero and which is marked by a dot, moves towards the nose of the bubble as the gravity level increases. The stagnation point does not exist in microgravity case due to the absence of the falling film. It is also seen from Fig. 3.3-5(b) that the dimensionless liquid film thickness (δ/D) increases by increasing gravity, resulting in more falling flow and the relative length of the Taylor bubbles in the slug unit decreases by increasing gravity [Fig. 3.3-5(c)]. This means that the volume of the Taylor bubble decreases by increasing gravity.

Figure 3.3-5(c) shows the instantaneous axial distribution of the wall (liquid-wall) shear stress (τ_w) in the slug unit under three selected gravities at J_L=0.15 m/s and J_G=0.15 m/s. The relative volumetric fraction of the Taylor bubble in the slug unit can be estimated by L_{TB}/L_{su}. The region with negative τ_w is due to the falling liquid film (FLF) that is the negative film velocity (in negative z direction) in Fig. 3.3-5(b), which causes a local reversal in the direction of the wall shear stress (aligned in the bulk flow direction), leading to a locally "positive" frictional pressure gradient, i.e., the pressure is "increased" in the flow direction. Note that a typical flow always creates a wall shear stress acting opposite to the bulk flow (positive shear stress) and, thus a negative pressure gradient.

It is seen that the FLF region starts at a certain distance from the bubble nose and penetrates the liquid slug region behind the tail of the Taylor bubble. It is clear that no negative τ_w exists at microgravity due to the absence of the FLF. Further, the FLF region extends in the slug unit by increasing gravity level, which means that at higher gravities, the falling film starts at a shorter distance from the bubble nose and penetrates to a longer distance into the liquid slug. This, in turn, generates a larger positive frictional pressure

gradient at higher gravities.

The effect of gravity on the length of the Taylor bubbles (L_{TB}) and slug units (L_{su}) and the ratio of them are shown in Fig. 3.3-6. The lengths are the average values of ten slug units for each gravity. It is seen that both the Taylor bubbles and slug units are shortened by increasing gravity, which can also be observed in Fig. 3.3-3. In addition, the ratio of Taylor bubble length to slug unit length decreases with gravity. At higher gravities, due to the increased hydrostatic pressure (body force), a single elongated bubble can breakup easily to the smaller ones resulting in a shorter slug unit.

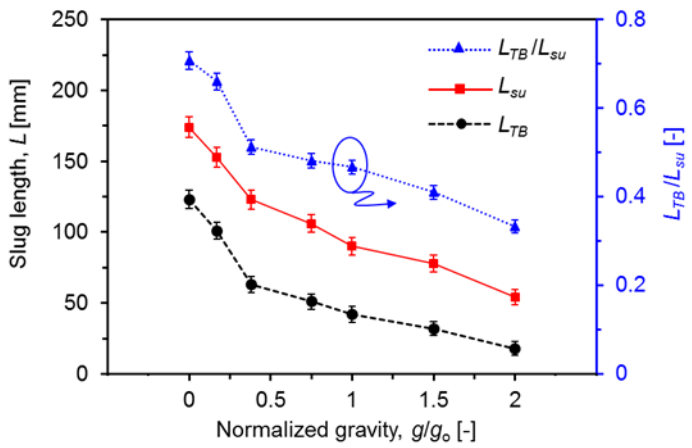

Figure 3.3-6 Effect of gravity on the length of the Taylor bubble (LTB) and slug unit (Lu) at J_L=0.15 m/s and J_G=0.15 m/s

Figure 3.3-7 shows the time-area-averaged, wall shear stress ($\bar{\tau}_w$) of a slug unit for all of the simulation cases in Table 3.3-2. It is shown in Fig. 3.3-7 that as gravity is increased, $\bar{\tau}_w$ decreases and finally becomes negative as a result of the increased FLF region. As mentioned earlier, the negative $\bar{\tau}_w$ physically means that the averaged wall shear stress is in the same direction of the bulk flow, resulting in a positive pressure gradient. It is also seen from Fig. 3.3-7 that by increasing the liquid superficial velocity (J_L), the onset of negative

$\bar{\tau}_w$ is delayed. This is due to the increased upward momentum of the liquid flow resulting in a decreased FLF region.

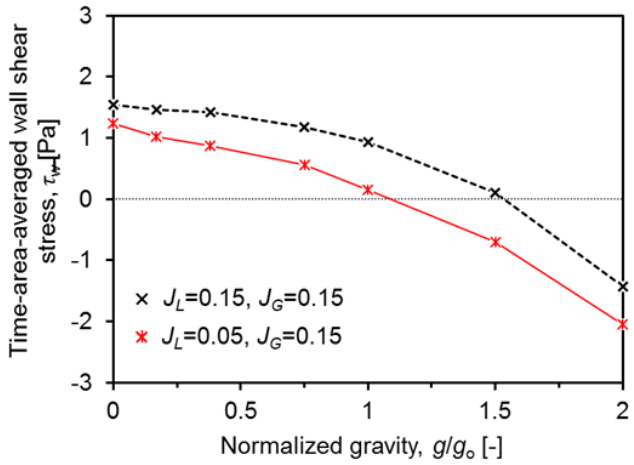

Figure 3.3-7 Variation of time-area-averaged wall shear stress of vertical upward slug flows with respect to gravity

Figures 3.3-8(a-e) show the temporal variations of frictional (circle marker), hydrostatic (diamond marker) and total (square marker) pressure gradients over the entire length (ΔL_{fd}) of the fully-developed region ($100 < z/D < 120$) under five selected gravities at J_L=0.15 m/s and J_G=0.15 m/s. The fluctuations of the pressure gradients are caused by the intermittent natures of a slug flow. The amplitude of the fluctuations increases with gravity. Note that the pressure gradients were calculated with a negative sign to make them positive. The infrequent negative frictional pressure gradients $[-(\Delta p/\Delta L_{fd})_f]$ in Fig. 3.3-8 are caused by the negative wall shear stress of the falling liquid film. However, the total pressure gradient $[-(\Delta p/\Delta L_{fd})_t]$ including the hydrostatic term $[-(\Delta p/\Delta L_{fd})_g]$ are always positive.

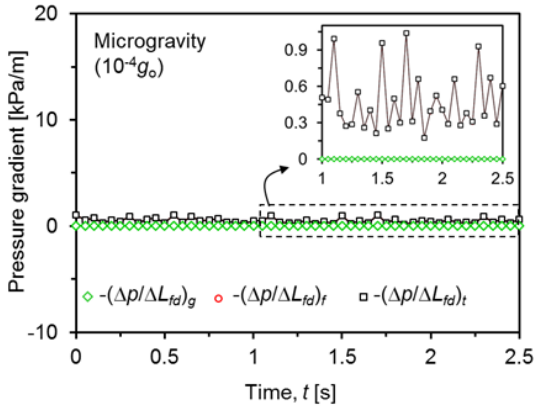
Microgravity
($10^{-4}g_o$)
Pressure gradient [kPa/m]
Time, t [s]
$-(\Delta p/\Delta L_{fd})_g$
$-(\Delta p/\Delta L_{fd})_f$
$-(\Delta p/\Delta L_{fd})_t$

(a)

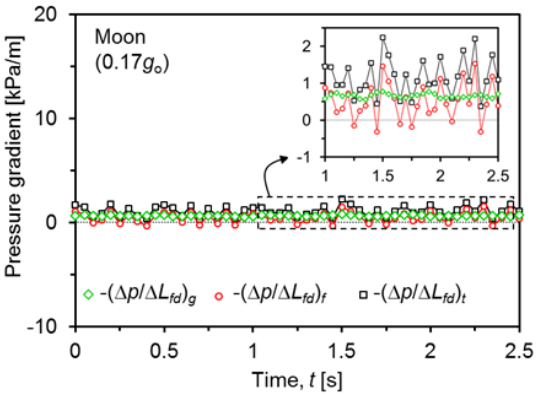
Moon
($0.17g_o$)
Pressure gradient [kPa/m]
Time, t [s]
$-(\Delta p/\Delta L_{fd})_g$
$-(\Delta p/\Delta L_{fd})_f$
$-(\Delta p/\Delta L_{fd})_t$

(b)

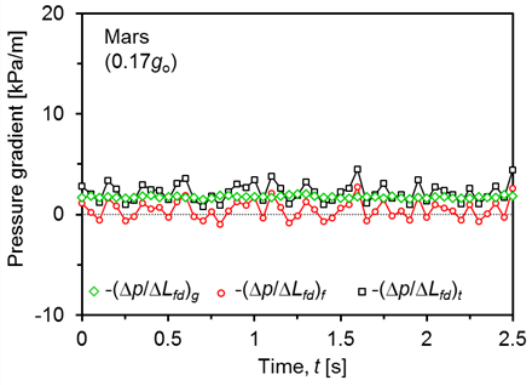
Mars
($0.17g_o$)
Pressure gradient [kPa/m]
Time, t [s]
$-(\Delta p/\Delta L_{fd})_g$
$-(\Delta p/\Delta L_{fd})_f$
$-(\Delta p/\Delta L_{fd})_t$

(c)

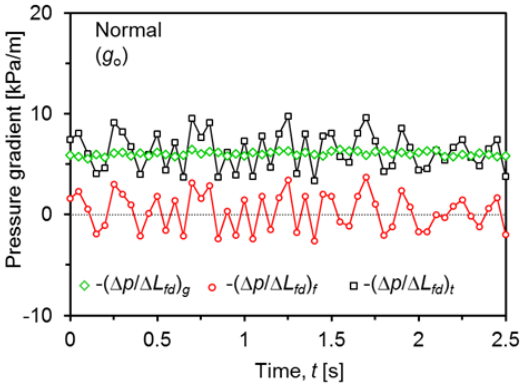

(d)

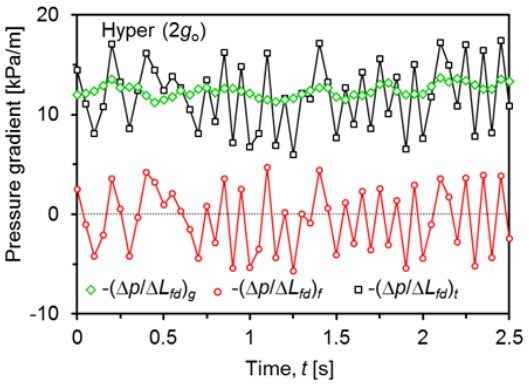

(e)

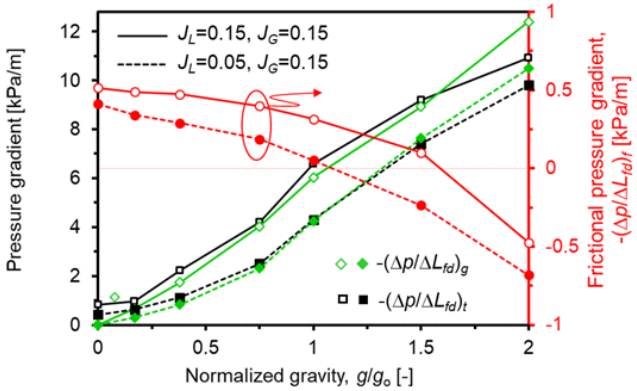

(f)

Figure 3.3-8 Temporal variations of frictional, hydrostatic and total pressure gradients for (a) micro ($10^{-4}g_o$), (b) Moon ($0.17g_o$), (c) Mars ($0.38g_o$), (d) normal (g_o), and (e) hyper ($2g_o$) gravities at J_L=0.15 m/s and J_G=0.15 m/s; and (f) time-averaged pressure gradients for two different sets of superficial velocities at J_L=0.15 m/s and J_G=0.15 m/s; J_L=0.05 m/s and J_G=0.15 m/s

Figure 3.3-8(f) shows the time-averaged frictional, hydrostatic, and total pressure gradients for all the simulation cases. It is seen that the frictional pressure gradient follows the trend of the wall shear stress shown in Fig. 3.3-7. It is also shown in Fig. 3.3-8(f) that as gravity is increased, the hydrostatic pressure drop increases monotonically because of the increased gravity and is a dominant contribution to the total pressure gradient. Note that the pressure drop of an adiabatic two-phase flow due to momentum changes is almost zero [131].

Figure 3.3-9(a) shows a temporal variation of the volumetric void fraction under five selected gravities at J_L=0.15 m/s and J_G=0.15 m/s. The entire volume of the fully-developed region (100< z/D <120) was selected for the void fraction calculations. The fluctuations of the void fraction are caused by the periodic passage of the Taylor bubbles with slightly different volumes in the vertical slug flows (Fig. 3.3-3). Figure 3.3-9(b) presents the time-averaged void fraction ($\bar{\varepsilon}$) and slip ratio (S) for all the simulation cases. It is shown in Fig. 3.3-9(b) that $\bar{\varepsilon}$ is decreased by increasing gravity, which means that the volume occupied by the gas phase is expanded when gravity is reduced. This phenomenon was also observed in Fig. 3.3-3 and Fig. 3.3-6.

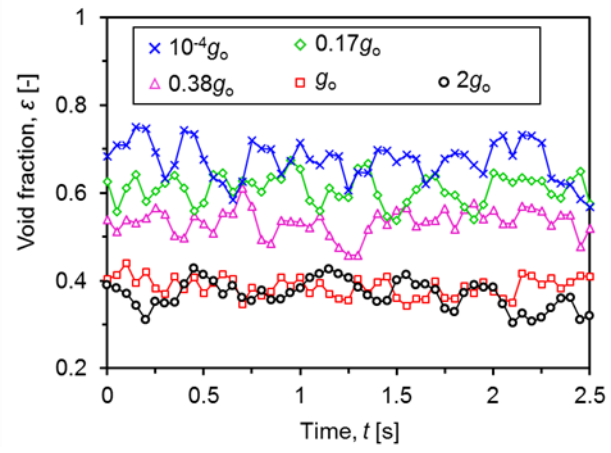

(a)

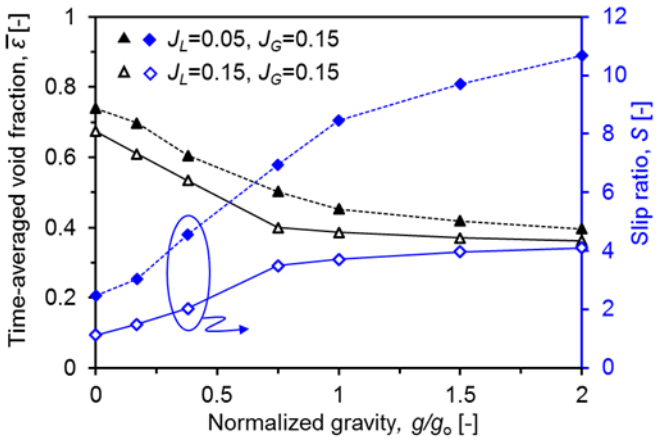

(b)

Figure 3.3-9 The (a) Temporal variation of void fraction (ε) for different gravities at J_L=0.15 m/s and J_G=0.15 m/s; and (b) time-averaged void fractions ($\bar{\varepsilon}$) and slip ratios (S) for two different sets of superficial velocities (J_L=0.15 m/s and J_G=0.15 m/s; J_L=0.05 m/s and J_G=0.15 m/s) under various gravities

The slip ratio (S) is a ratio of a gas velocity to a liquid velocity and is calculated by

$$S = \frac{u_G}{u_L} = \frac{(1-\varepsilon) J_G}{\varepsilon J_L}, \tag{3-31}$$

where u_G and u_L are the actual velocity of gas and liquid phases, respectively, ε is the void fraction, and J_G and J_L are the superficial velocity of gas and liquid phases, respectively. It is shown in Fig. 3.3-9(b) that the slip ratio is increased by increasing gravity, which is due to a decrease in the void fraction at the same gas flow rate leading to an increase in the gas velocity and the liquid velocity is subsequently decreased. The slip ratio is directly related to the magnitude of the drag force exerted by the liquid flow on the Taylor bubbles. This can be clearly observed from Fig. 3.3-4 in the MFR view that the liquid streamlines under hyper-gravity are mostly downward over the Taylor bubble which makes the uni-directional slip between the phases strong. In contrast, for microgravity case, the liquid

streamlines are both upward and downward which makes the bi-directional slip canceled out.

Figure 3.3-10(a) shows the simulation result of the rising velocity of the Taylor bubbles (circle markers) under various gravities and a comparison with the predicted values obtained by Eq. Nicklin's model [Eq. (3-35)] using both mixture superficial velocity (J), and volume-averaged liquid velocity for u_L. It is shown in Fig. 3.3-10(a) that the Nicklin's model using mixture superficial velocity fails to accurately predict the numerically obtained results of bubble rise velocity (u_{TB}) under different gravities. Rather, the predicted values using the volumetric-averaged liquid velocity for u_L in Nicklin's model match reasonably well the numerical results of u_{TB} under various gravities except hyper-gravity ($2g_o$). The underestimation of u_{TB} under hyper-gravity might be attributed to the intensified FLF and wake region which causes more disturbance in the liquid velocity field compared to those at lower gravities.

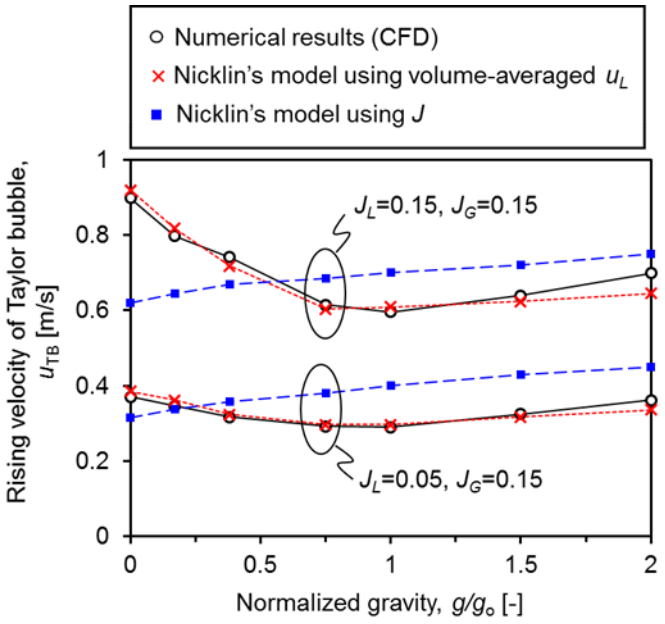

(a)

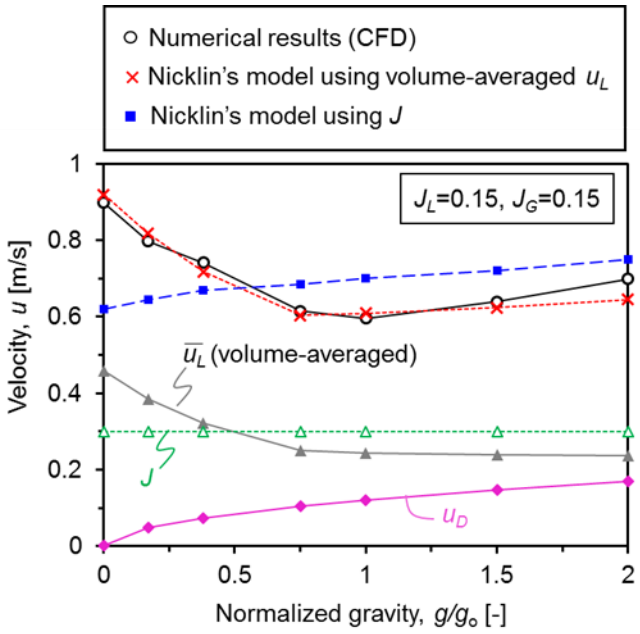

Figure 3.3-10 (a) Effect of gravity on rising velocity of Taylor bubble compared with the predicted values by Nicklin's [121] correlation using both volumetric-averaged liquid velocity and mixture superficial velocity for u_L; and (b) variation of volume-averaged liquid velocity, drift velocity, and rising velocity of a Taylor bubble under various gravities at J_L=J_G=0.15 m/s

It is also seen from Fig. 3.3-10(a) that, by increasing gravity, the rising velocity (u_{TB}) initially decreases until it reaches to a minimum around normal gravity (g_o) and then increases. To further elaborate this intriguing behavior, both the liquid mean velocity (u_L) and drift velocity (u_D) are shown in Fig. 3.3-10(b) under various gravities for the case of J_L=0.15 m/s and J_G=0.15 m/s. The bubble drift velocity (u_D) is increased by increasing the gravity as a result of the augmented buoyancy force exerted on the Taylor bubble. On the other hand, despite of the fixed mixture superficial velocity, the volumetric-averaged liquid velocity (u_L) is deceased by increasing gravity due to the reduced void fraction [$u_L = J_L/(1-\varepsilon)$]. These two competing effects determine the trend of the rising velocity of the Taylor bubble with a maximum around normal gravity.

Figure 3.3-10(a) also suggests that using volumetric-averaged liquid velocity in original Nicklin's model [Eq. (3-29)] is more effective than using mixture superficial velocity. Generally, the approximation of ($\overline{u}_L = J$) may cause errors when the liquid slugs are short, or liquid slugs contain many small droplets, or wake regions behind the bubble tail is relatively large as a result of intensified falling liquid film. In those cases, the bubble rise velocity might be a better function of actual mean liquid velocity (volume-averaged) rather than total superficial velocity.

3.3.3 Summary

A systematic CFD simulation was performed to study the hydrodynamics of a vertical upward slug flow focusing on a Taylor bubble hydrodynamics under various gravities including $10^{-4}g_o$ (microgravity), $0.17g_o$ (Moon), $0.38g_o$ (Mars), g_o (=9.81 m/s^2, Earth), and $2g_o$ (hyper). The results show that the Taylor bubbles are shortened more than the liquid slugs by increasing gravity, resulting in a lower slug unit void fraction. Analysis of the flow field around a Taylor bubble reveals that a reversal of wall shear stress caused by a falling-film flow can create a positive frictional pressure gradient in the vertical slug flow. The falling film flow is intensified by increasing gravity, whereas at microgravity, no falling film exists around a Taylor bubble. The total pressure gradients, however, are always positive and increase monotonically by increasing gravity due to the increased hydrostatic pressure gradient. The rising velocity of a Taylor bubble is minimum around normal gravity.

4 CHAPTER 4: CONVECTIVE HEAT TRANSFER ENHANCEMENT

This work discusses the convective heat transfer enhancement of non-condensing slug flows by using phase separation for local liquid circulations through a porous-tube insert. Numerical simulations were carried out to study the air-water slug flow and heat transfer without phase change (boiling and condensation) in a vertical upward flow. The governing equations of two-phase flow and heat transfer were numerically solved using the Volume of Fluid-Continuum Surface Force (VOF-CSF) method in a two-dimensional axisymmetric computational domain. The rear end (exit) of the porous tube was open to allow discharge of fluid, but two different designs of the frontal end were considered; a porous tube with a closed front that prevents the bubbles from entering the porous tube and keeps the bubbles in the annular gap; a porous tube with an open front allows the bubbles to flow through the porous tube. In addition, a set of parametric simulations was systematically carried out for an optimization of the annular gap dimension (or porous tube diameter) for the maximum heat transfer.

4.1 TWO-PHASE NON-CONDENSING HEAT TRANSFER

4.1.1 Computational model

The VOF-CSF model presented in Section 2.1 is extended to account for heat transfer. No phase change was considered. The model requires the solution of mass, momentum, energy, and phase-fraction (α) equations [Eqs. (1-3)].

Mass:

$$\frac{\partial}{\partial t}(\rho)+\nabla\cdot(\rho\boldsymbol{u})=0\ , \tag{4-1}$$

Momentum:

$$\frac{\partial}{\partial t}(\rho \boldsymbol{u}) + \nabla \cdot (\rho \boldsymbol{u}\boldsymbol{u}) = -\nabla p + \nabla \cdot (\mu \nabla \boldsymbol{u}) + \rho \boldsymbol{g} + \boldsymbol{F} \ , \tag{4-2}$$

Energy:

$$\frac{\partial}{\partial t}(\rho c_p T) + \nabla \cdot (\boldsymbol{u} \rho c_p T) = \nabla \cdot (k \nabla T), \tag{4-3}$$

where $\boldsymbol{u}$ denotes the velocity vector, p the pressure, and T the temperature. The bulk properties such as density ρ, viscosity μ, thermal conductivity k, and heat capacity c_p are calculated using the average values of the two phases, weighted by their respective phase fractions α (i.e. $\rho = \alpha_L \rho_L + \alpha_G \rho_G$).

Numerical simulation of the two-phase flow in a tube including a porous-tube-insert is inherently a three-dimensional (3-D) system. However, for a vertical flow, due to the neutral effect of gravity in the radial direction, it is reasonable to approximate the 3-D system to a two-dimensional (2-D) axisymmetric one. Figure 4.1-2(a) shows the simplified 2-D system using ring-shape pores with a pore width of w' and a wire thickness of δ' to provide an equal flow area and capillary pressure as the corresponding 3-D system with square pores having a pore width of w and a wire thickness of δ'.

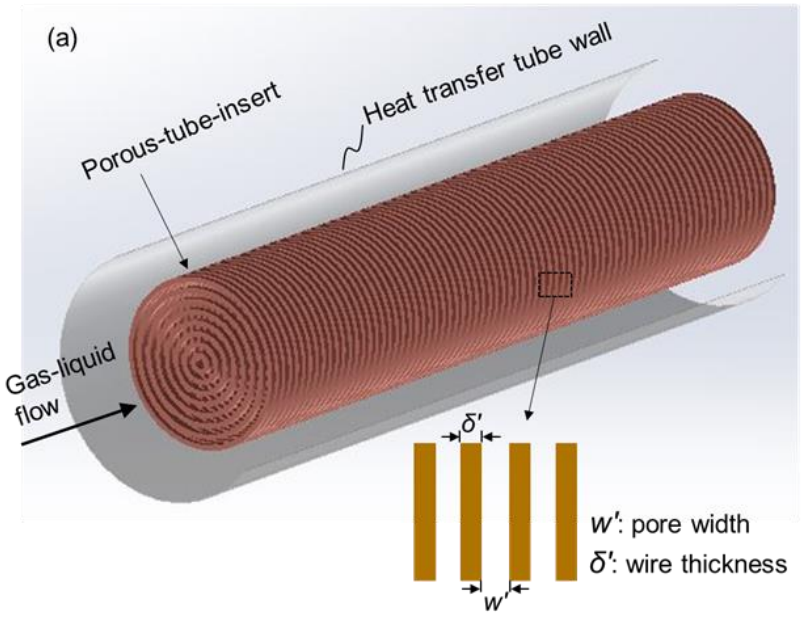

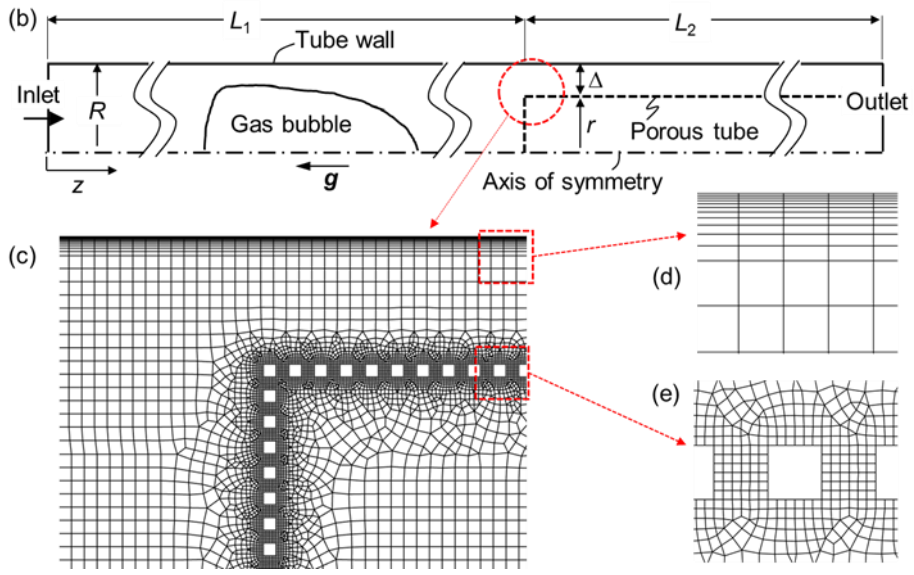

Figure 4.1-1 (a) 2-D axisymmetric system for vertical upflow slug flows in a tube with a porous-tube-insert with closed frontal side; and (b) computational domain of the slug flow; and (c) multiscale grid system used in the computational domain with refined meshes (d) near the tube wall and (e) in the vicinity of the pores

The geometric conversion is required to satisfy the criteria of equal flow area and capillary pressure [87] as below,

$$w' = 0.5w \ , \tag{4-4}$$

$$\delta' = \delta + \frac{\delta^2}{2w} \ . \tag{4-5}$$

In the 2-D system, both the pore width and wire thickness are 100 μm, which corresponds to a pore width of 200 μm and a wire thickness of 82.84 μm in an equivalent 3-D system.

Figure 4.1-2(b) shows the computational domain of the 2-D vertical upward slug flow in a vertical tube with a porous-tube-insert (PTI) with a closed frontal end. The computational domain consists of a multiscale coupled grid system as shown in Figs. 4.1-2 (c-e); A quasi-uniform mesh size of 100 μm is generated in the bulk flow region along the axial direction [Fig. 4.1-2(c)] except near the tube wall [Fig. 4.1-1(d)] and pores [Fig. 4.1-1 (e)]. The significant refined meshes were used near the pores where the fine mesh size of

16.67×16.67 μm corresponds to twenty-eight meshes within a square pore surface [Fig. 4.1-1(b)]. The height of the wall boundary layer mesh was gradually refined along the radial direction toward the tube wall ranging from 100 μm in the bulk region to 5 μm in the first mesh of the boundary layer on the tube wall [Fig. 4.1-2(d)]. T The refined meshes were also created near the pores where the mesh size is 16.67×16.67 μm and twenty-eight meshes are used within a square pore [Fig. 4.1-2(e)]. In order to ensure the simulation results independent of mesh size, a change in average heat flux (q") was calculated while increasing the number of meshes. The mesh count was increased until the computed value of the current case was within less than 3% of the previous case. Figure 4.1-2 shows a converging trend of the average heat flux (q") with the mesh number. Since there were no significant changes in the average heat flux (q") achieved from 429,400 cells to 591,874 cells, 429,400 cells was chosen for the entire simulations in this study.

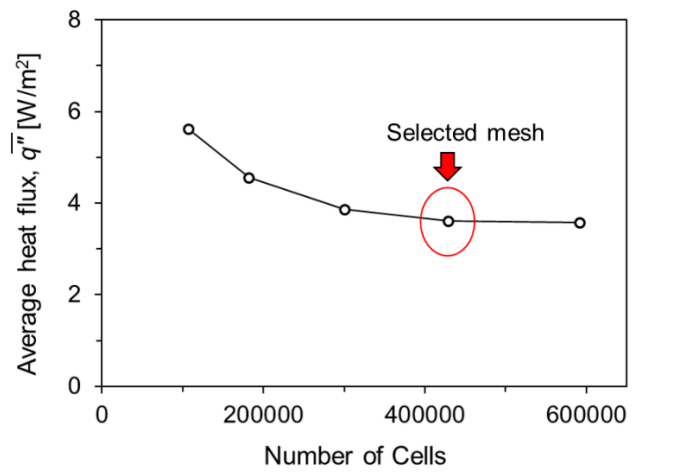

Figure 4.1-2 Grid dependency of the computational results of average heat flux for non-condensing air–water slug flow in a PTI

Table 4.1-1 lists the thermophysical properties of working fluids at 20°C and Table 4.1-2 lists the major parameters used for the numerical simulations.

Table 4.1-1 Thermophysical properties of working fluids used in the simulations

Fluid	Density, ρ [kg/m^3]	Kinematic viscosity, v [m^2/s]	Specific heat, c_p [J/kgK]	Thermal conductivity, k [W/mK]	Surface tension, σ N/m]
Water	998	10^{-6}	4182	0.600	0.072
Air	1.2	1.480×10^{-5}	1006	0.024	-

Table 4.1-2 Major parameters used in the numerical simulations

Parameter	Value
Tube length, L [mm]	900
Length of bare tube section, L_1 [mm]	500
Length of porous-insert-tube section, L_2 [mm]	400
Tube radius, R [mm]	3.150
Porous tube radius, r [mm]	1.650
Wire thickness, δ' [mm]	0.100
Pore width, w' [mm]	0.100
Tube wall temperature, T_w [°C]	10
Inlet temperature, T_i [°C]	20
Inlet void fraction of the homogenous two-phase flows, ε_i [-]	0.400
Inlet velocity of the homogenous two-phase flows, u_i [m/s]	0.068

The air-water mixture flow was introduced at the tube inlet at a constant temperature (T_i) of 20°C. A uniform velocity (u_i) and a homogenous void fraction (α_i) was used at the tube inlet, which allows small gas bubbles to grow into slug bubbles, and actual void fraction to be determined during the numerical simulation. The no-slip condition was applied on each pore surface and the tube wall. It is worth mentioning that due to the absence of actual triple-phase (gas-liquid-solid) point, the wall contact angle is not important in this study. The liquid film thicknesses around the gas bubbles were in the range of 20μm ~ 800 μm,

where the van der Waal attraction between the liquid and solid phases is negligible for such a thick liquid film [81, 87]. The atmospheric pressure was set at the tube outlet. This study used a constant wall temperature of 10°C, which was 10°C colder than the inlet fluid's temperature, so that the air-water mixture flow is cooled by the tube wall.

In order to simulate the complex hydrodynamics of the two-phase flows, a transient simulation with a time step of 10^{-5} s was used. Gravitational field was also applied opposite to the flow direction to create an upward flow configuration.

4.2 HEAT TRANSFER ENHANCEMENT USING CAPILLARY PHASE SEPARATION

Five different cases were considered in this study as shown in Fig. 4.2-1. A liquid-only (single-phase) flow was selected as a baseline (Case 1), and a two-phase slug flow in a bare tube was considered as another baseline for two-phase slug flows (Case 2). Three cases using either a porous (Cases 3, 5) or solid (Case 4) insert with the same diameter and length were used to study the hydrodynamic characteristics and heat transfer enhancement mechanisms:

- Case 3: A porous-tube-insert (PTI) with a closed front suspended in a tube is used to create elongated ring-shaped slug bubbles in the annular gap between the PTI and tube wall.
- Case 4: A solid-insert (SI) suspended in a tube is used to create elongated ring-shaped slug bubbles in the annular gap between the SI and tube wall. Note that the liquid flow can't freely flow through the SI for Case 4 but can freely flow through the PTI for Case 3.
- Case 5: A porous-tube-insert (PTI) with an open front suspended in a tube is used to capture the slug bubbles stay inside the porous tube.

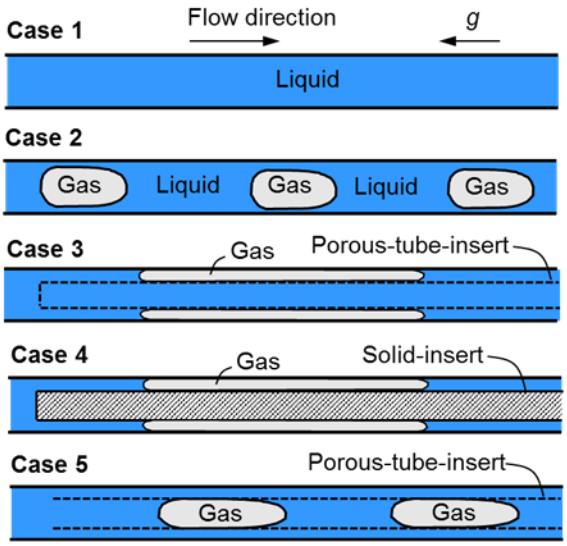

Figure 4.2-1 Five different cases used for comparison of the convective heat transfer performance

4.2.1 Two-phase slug flows in bare tube (Case 2)

Two-dimensional axisymmetric simulations of two-phase flows of water and air in a tube with a diameter of 6.3 mm and a length of 900 mm (~143D) were carried out. A mixture velocity (u_i) of 0.068 m/s and a void fraction (ε_i) of 0.4 at the inlet were used to create a slug flow in the tube (Case 2 in Fig. 4.2-1). The calculated liquid and gas Reynolds numbers are 257 and 12, respectively and therefore the two-phase flow is laminar. The inlet temperature of the flow of 20 °C and a constant tube wall temperature of 10 °C were used to cool the fluid by the tube. The baseline case for a single-phase (liquid-only) flow (Case 1 in Fig. 4.2-1) with the same conditions was also simulated for comparison.

Figure 4.2-2(a) shows the streamlines of the liquid flow around a gas bubble in a fully-developed flow region. The streamlines of the liquid flow were drawn in a fixed frame of reference (FFR). It is apparent that the falling liquid film through the gap between the tube wall and bubble creates a vortex behind the bubble tail. The temperature contour [Fig. 4.2-2(b)] indicates that the temperature inside the bubble is relatively lower than that of the

liquid slugs. Because of the vortex pushing the hot liquid toward the wall, the temperature in the liquid slug behind the bubble tail is high and uniform. Similar qualitative temperature distributions were reported in the previous studies in literature for slug (Taylor) flow in microchannels [79, 80, 103].

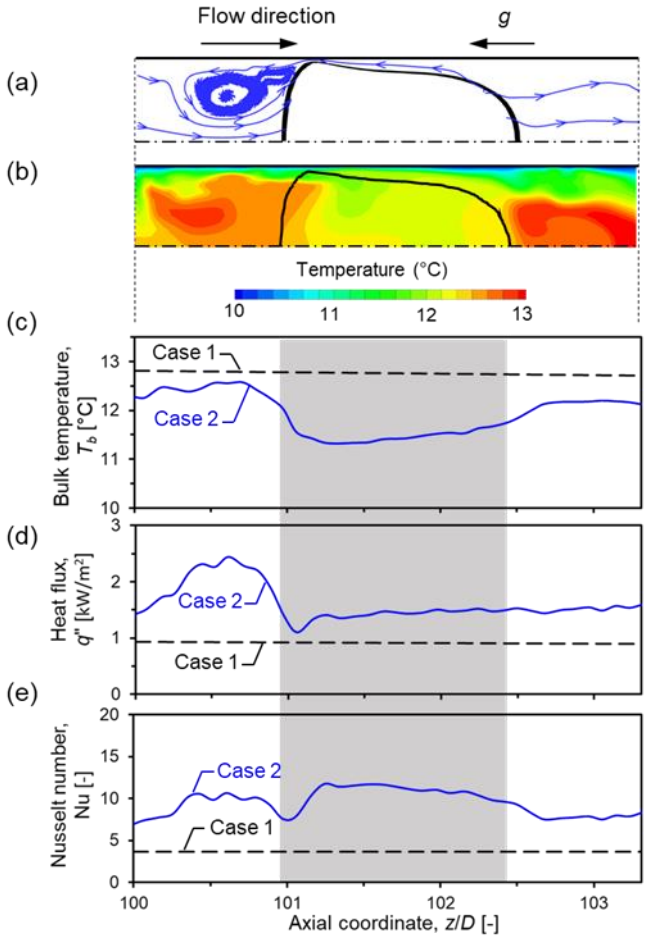

Figure 4.2-2 (a) Streamlines of liquid flow. (b) Temperature contour around a gas bubble. Axial variations of (c) the bulk temperature, (d) local wall heat flux, and (e) local Nusselt number in the fully-developed flow region along the axial distance (z) from the inlet

Figure 4.2-2(c) shows the calculated local bulk temperature (T_b) of the two-phase flow in the fully-developed region. The bulk (mean) temperature at a certain axial location is defined as

$$T_b = \frac{\int_0^R \rho |u| c_p T (2\pi r) dr}{\int_0^R \rho |u| c_p (2\pi r) dr}. \quad (4\text{-}6)$$

where R is the tube radius and r is the radial coordinate. In order to properly account the contributions of the falling film and vortex region, the absolute value of the axial velocity (u) was used for the bulk temperature calculation [132]. It is worthwhile to mention that that the radial velocity is ignored in Eq. (10), because the magnitude of the axial velocity dominates the radial component. Fig. 4.2-2(c) shows a higher bulk temperature in the liquid regions than that of the bubble (shared area) as seen in Fig. 4.2-2(b) and the bulk temperature of the baseline liquid-only flow (Case 1) is higher than that of the two-phase flow because of the inferior heat transfer of the liquid-only flow upstream of the region shown in the figure. Details of the results of the heat transfer are discussed below.

Figure 4.2-2(d) shows the variation of the local wall heat flux (q''). The wall heat flux was calculated by the conduction through the first liquid layer (5 μm thick) fixed on the tube wall as below

$$q'' = -k \left. \frac{\partial T}{\partial r} \right|_{r=R}, \quad (4\text{-}7)$$

where r is the radial coordinate and k is the liquid thermal conductivity.

It is seen from Fig. 4.2-2(d) that the heat flux in the liquid behind the bubble tail is relatively high due to the strong mixing by the vortex. The heat flux decreases toward the bubble region but is still higher than that of the liquid-only flow.

The local Nusselt number (Nu) shown in Fig. 4.2-2(e) is calculated by

$$Nu = \frac{q'' D}{k_L (T_b - T_w)}. \quad (4\text{-}8)$$

The Nusselt number is higher in the entire region than that of the liquid-only flow (Nu=3.66

for Case 1). The strong mixing in the vortex region and the thin liquid film in the bubble region increases the local Nusselt number. The heat flux in the bubble region is, however, relatively low because of the lower bulk temperature [Fig. 4.2-2(c)]. The high bulk temperature and convective heat transfer coefficient in the vortex region greatly enhances the convection heat transfer.

For a quantitative comparison of the heat transfer, the average Nusselt number was calculated using the averaged heat flux and bulk temperature over the entire slug unit consisting of a bubble and a liquid slug as below

$$\mathrm{Nu}_{\mathrm{ave}} = \frac{q''_{\mathrm{ave}}}{\left(T_{b,\mathrm{ave}} - T_w\right)} \frac{D}{k_L}, \tag{4-9}$$

$$q''_{\mathrm{ave}} = \frac{1}{L_u} \int_0^{L_u} q''\, dz, \tag{4-10}$$

$$T_{b,\mathrm{ave}} = \frac{1}{L_u} \int_0^{L_u} T_b\, dz, \tag{4-11}$$

where L_u is the total length of slug unit. The averaged Nusselt number of the slug flow was 9.37 that is 156% higher than that of the equivalent liquid-only flow.

For the heat transfer of two-phase slug flows in vertical tubes, Dong and Hibiki [133] identified more than 200 experimental data through a comprehensive literature survey. Using the experimental data bank and the theoretical Reynolds and Chilton–Colburn analogies, they presented a correlation to predict the heat transfer coefficient (or Nusselt number) for the slug flows in vertical tubes, which successfully predicted 95.1% of the data within ± 30% error. The correlation for laminar flow (Re_L<2300) is given by

$$\frac{Nu_{2\varphi}}{Nu_{1\varphi}} = \left(1-\varepsilon\right)^{0.339} \left(1 + \frac{4.65}{X^{0.409}}\right), \tag{4-12}$$

$$Nu_{1\varphi} = 1.86\left(\mathrm{Re}_L \,\mathrm{Pr}_L \frac{D}{L}\right)^{1/3}\left(\frac{\mu_B}{\mu_w}\right)^{0.14}, \tag{4-13}$$

where $\mathrm{Nu}_{2\varphi}$ and $\mathrm{Nu}_{1\varphi}$ are the two-phase and single phase Nusselt number respectively; μ_w and μ_B are the liquid viscosity calculated based on the temperature of the tube wall and the bulk fluid, respectively. ε is the void fraction and X is the Martinelli parameter and is defined as

$$X = \frac{\dot{m}_L}{\dot{m}_G}\sqrt{\frac{\rho_G}{\rho_L}} = \left(\frac{1-x}{x}\right)^{0.9}\left(\frac{\rho_G}{\rho_L}\right)^{0.5}\left(\frac{\mu_L}{\mu_G}\right)^{0.1}, \tag{4-14}$$

where x is gas (vapor) quality; and $\dot{m}_L$ and $\dot{m}_G$ are the mass flow rate of liquid and gas phases, respectively.

Fifteen different laminar air-water slug flow cases with various inlet conditions (inlet mixture velocity and homogenous void fraction) were numerically simulated for model validation purpose. The average Nusselt numbers were calculated using Eq. (4-9) in the numerical simulation and compared with the values predicted by the Dong and Hibiki's correlation [Eq. (4-12)] within an error band of ±15% as shown in Fig. 4.2-3

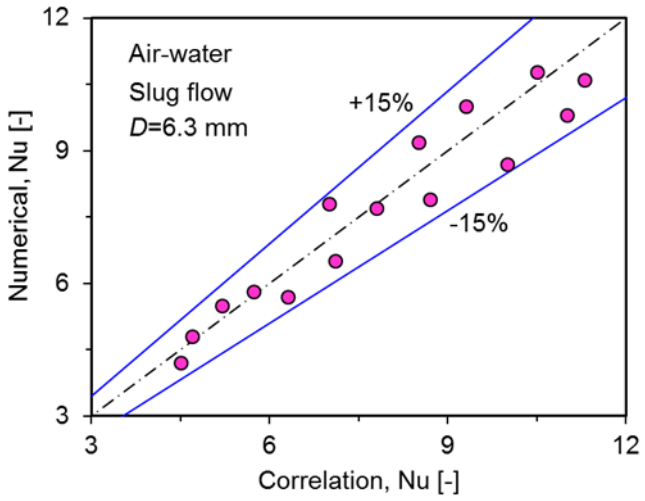

Figure 4.2-3 Comparison of the computed average Nusselt number of two-phase slug flows with those predicted by Dong and Hibiki's correlation [133]

4.2.2 Convective heat transfer enhancement of slug flows using suspended tube inserts (Cases 3-5)

Hydrodynamic characteristics

Figure 4.2-4 shows the slug bubble flow in a bare tube [Fig. 4.2-4(a), Case 2] and the modulated flows using tube inserts [Fig. 4.2-4(b-d)]. Because of the axisymmetric nature of the vertical flows, only the computational domains shown in Fig. 4.2-4 were used for the simulation. It is noteworthy that the bubble could not penetrate through the small pores (200 μm) of the porous tube (Cases 3 and 5) for the conditions used for this study, resulting in a capillary-assisted phase separation. Therefore, in Case 3, the gas bubble is forced to flow through the narrow annular gap, elongating the bubble in a ring shape. The same shape change of the bubble occurs in Case 4 using a solid insert [Fig. 4.2-4(c), Case 4]. To deal with all possible designs using a tube insert, Case 5 using a porous tube with an open front was considered to keep the bubble inside the porous tube instead of the annular gap (Case 3).

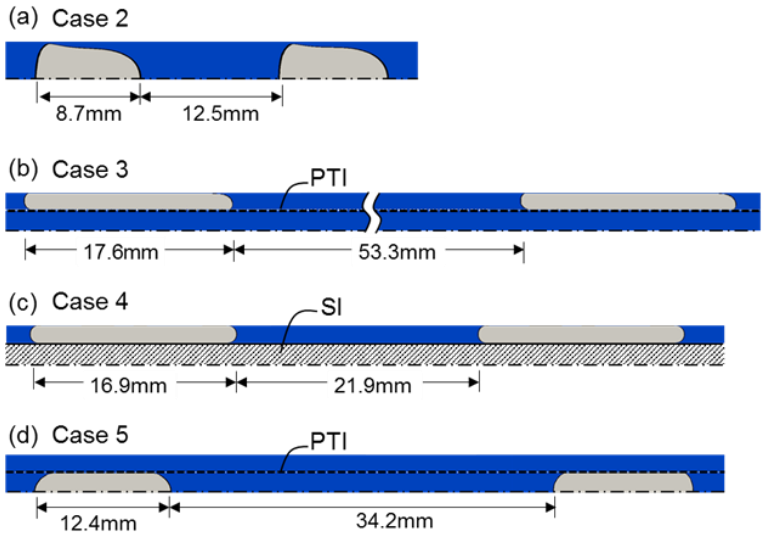

Figure 4.2-4 Four different designs considered for computational simulation: (a) bare tube (Case 2); (b) porous-tube-insert with a closed front (Case 3); (c) solid-insert (Case 4); and (b) porous-tube-insert with an open front (Case 5)

The elongated bubble in Cases 3 and 4 is almost twice longer than that of Case 2 because of the bubble confinement in the annular gap and the bubble in Case 5 is about 1.4 times of that of Case 2. The liquid slug is also extended for all the cases. The liquid slug in Case 3 is maximum (53.3mm) and is more than four times of that in Case 2. It is also true for the liquid slugs in Cases 3-5 which are much longer than that of Case 2. The elongation of the liquid slugs in the cases using the PTI (Cases 3 and 5) are due to the liquid circulation through the porous-insert as discussed below.

Figure 4.2-5 shows the streamlines of the liquid flow around the bubble for Case 3 in a fixed frame of reference. The large difference in the densities of the liquid and gas phases and the resulting buoyancy force create a counterflow of the bubble moving upward in the annular gap and liquid moving downward inside the porous tube as shown in Fig. 4.2-5(a), resulting in an internal circulation of the liquid flow through the porous insert.

Figures 4.2-5(b-e): show the magnified views of the flow patterns at the different locations around the bubble. In Fig. 4.2-5(c) (region 2), the bubble stays outside the porous tube because the gas pressure in the bubble is too low to break the gas-vapor interface (meniscus) formed in the micropores of the porous tube, while the liquid can freely flow through the pores. The liquid film thickness is about 17 μm between the pore surface and the bubble.

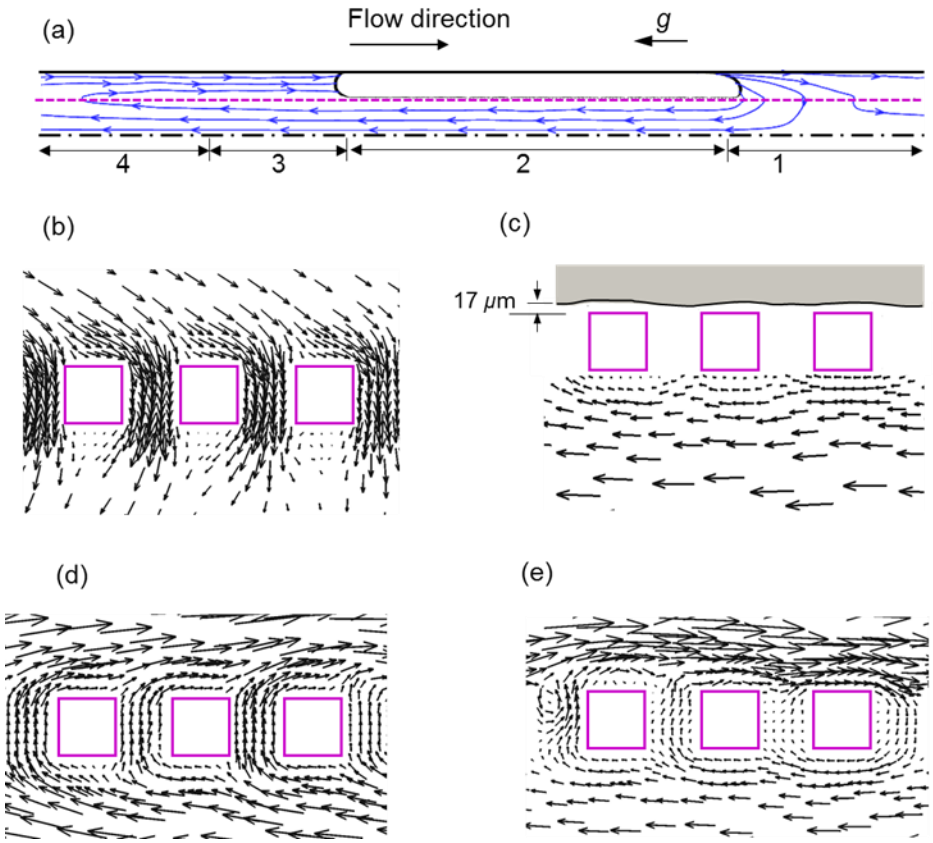

Figure 4.2-5 (a) Streamlines of the liquid flow around a gas bubble outside the porous-tube-insert with a closed front (Case 3); and enlarged flow vectors near the pores of the porous tube in (b) region 1; (c) region 2; (d) region 3; and (e) region 4

Figure 4.2-6 shows the streamlines of the liquid flow around the bubble for Case 5 in a fixed frame of reference. Case 5 has the bubble flowing inside the porous tube, which was introduced through the open front of the porous tube. Similar to Case 3, Case 5 also has a liquid circulation but through the annular gap.

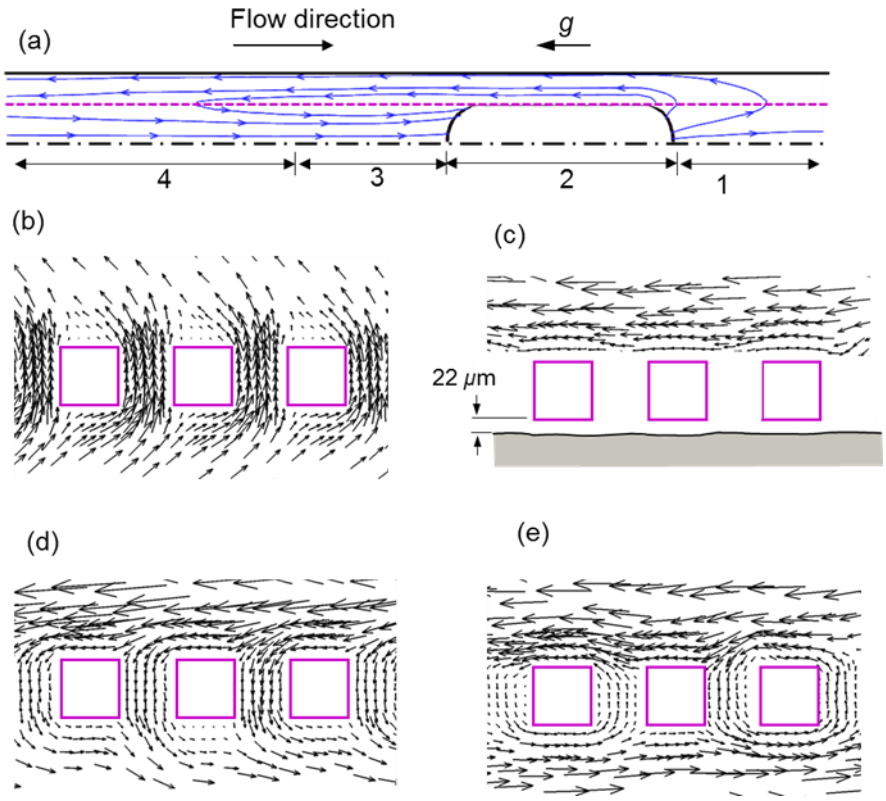

Figure 4.2-6 (a) Streamlines of the liquid flow around a gas bubble inside the porous-tube-insert with an open front (Case 5); and enlarged flow vectors near the pores of the porous tube in (b) region 1; (c) region 2; (d) region 3; and (e) region 4

To study the effects of the inserts on the flow modulation, two locations [A and B in Fig. 4.2-7(a)] were selected for comparison of the cross-sectional velocity profile in the middle of the bubble and liquid slug for each case, respectively.

Figures 4.2-7(b-c) compare the cross-sectional axial velocity profiles for different cases in the middle of the bubble. As shown in Fig. 4.2-7(b), the bubble travels faster in the cases with PTI (Cases 3 and 5) than the other cases (Cases 1, 2 and 4). This is because of the fast liquid flowing backward through either the porous tube (Case 3) or the annular gap (Case 5), which results in the fast bubble moving forward. In contrast, in Case 4 with a solid insert, the bubble and liquid slug flow slowly in the confined annular gap without a substantial liquid flowing backward. The similar results are also observed in the bare tube

(Case 2).

In Fig. 4.2-7(c)], the cross-sectional axial velocity profiles in the liquid slug for different cases are compared. It is obvious that the velocity profiles of Cases 3 and 5 using a PTI, because of the liquid flow and phase separation, are dramatically different from the typical parabolic profile of a developed flow in a bare tube (Cases 1 and 2). The maximum velocities in Cases 3 and 5 with a PTI are now shifted toward the tube wall from the tube center of the bare tube (Cases 1 and 2), and the velocity profiles have both positive (forward) and negative (downward) velocity regions unlike Cases 1, 2 and 4.

In Case 4 with a solid insert, although the maximum velocity is increased due to the reduced flow area compared to that of the bare tube, it is much less than those in the PTI cases. This attributes to the existence of significant downward liquid flow in the PTI cases as explained above. Note that the velocities at the porous tube wall are zero because of the no-slip boundary condition.

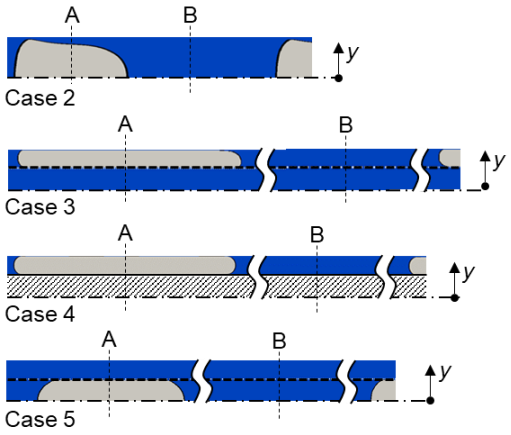

(a)

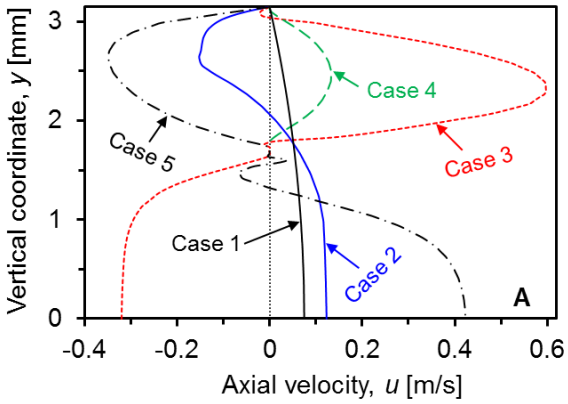

(b)

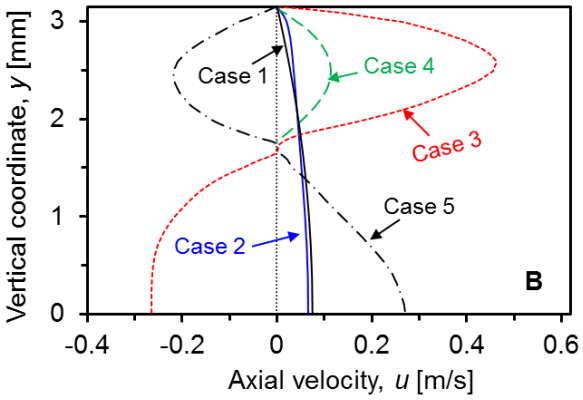

(c)

Figure 4.2-7 (a) Selected tube cross-sections in different cases. The axial velocity profiles at (a) the cross section "A" in the bubble; and (b) the cross section "B" in the liquid slug

The convective heat transfer is greatly affected to the fluid's velocity gradient on the wall as stated by the Reynolds analogy [134]. Figure 4.2-8 shows the comparison of the averaged axial velocities of the liquid slugs between two consecutive bubbles, specifically in the annular gaps for Cases 3-5. The average velocity of the fully developed single phase flow (Case 1) is also shown as the baseline. Note that the negative values indicate a downward flow for Case 5. It is obvious that the liquid velocity for Case 4 with a solid insert is higher than that of Case 2 using a bare tube due to the reduced flow area.

For Cases 3 and 5 using a PTI, however, the matter is more complicated. In Case 3, the

axial velocity decreases in a short region close to the nose of the following bubble because of the radial flow leaking from annular gap to the porous tube [Fig. 4.2-5(b)] but gradually increases due to the liquid infiltration from the porous tube [Fig. 4.2-5(c-d)]. In Case 5, the opposite results to Case 3 are observed and therefore the liquid flows downward in the entire annular gap. Although the flow directions in the annular gap for Cases 3 and 5 are opposite each other, the velocities are higher than that in the bare tube (Case 2), especially behind the bubble tail.

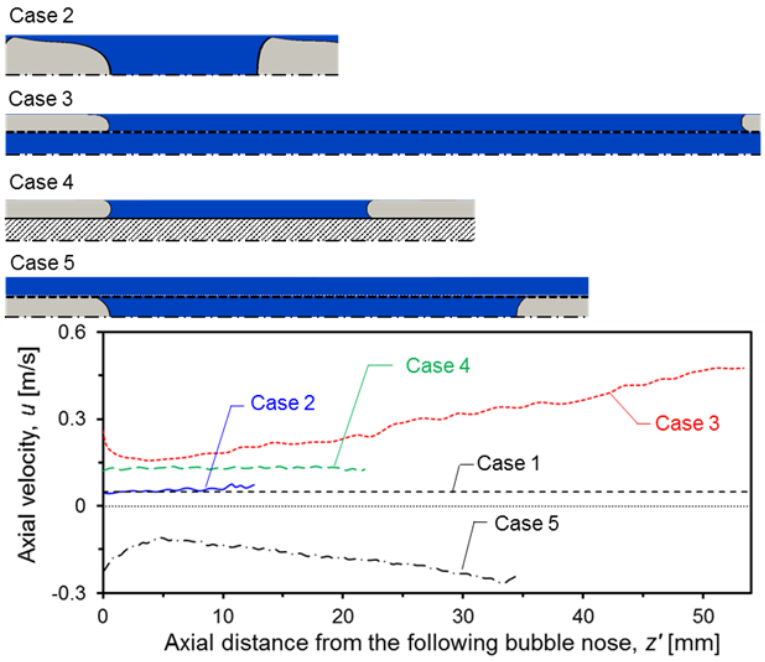

Figure 4.2-8 Axial velocity variation in the liquid slug between two consecutive bubbles for the different cases

Figure 4.2-9(a) shows the trace of the gas-liquid interface of a fully-developed bubble in the bare tube (Case 2). The interface of the bubble is defined by a line with a phase fraction (α) of 0.5. The local liquid film thicknesses along the axial distance (z') [Fig. 4.2-9(a)] from the bubble tail are shown in Fig. 4.2-9(b). Note that the film thicknesses are shown in a logarithmic scale. It is seen that the confined bubbles in Cases 3 and 4 have longer length and much thinner film thickness than those in the bare tube (Case 2). For

Case 5, the bubble is slightly elongated as compared to that in Case 2 and the film thickness equals to the thickness of the annular gap.

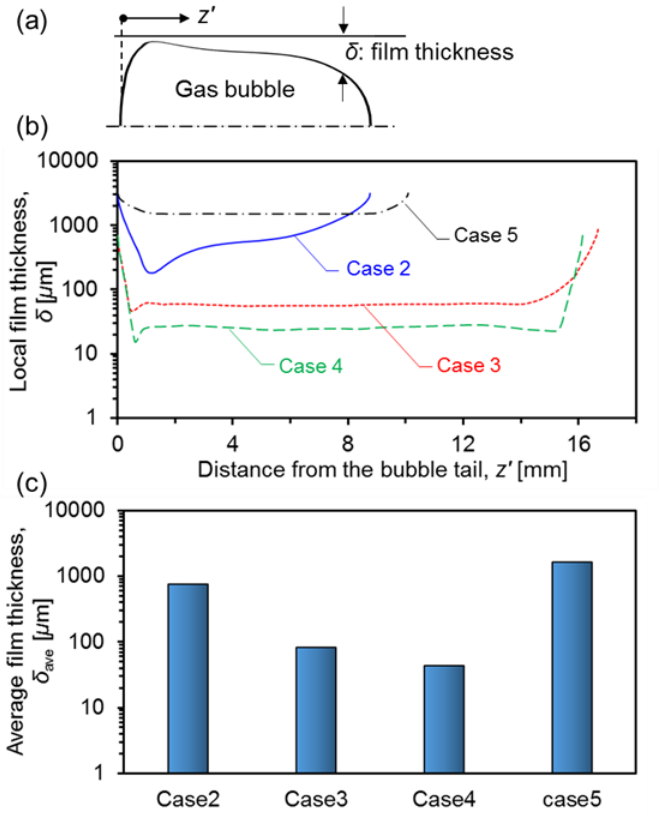

Figure 4.2-9 (a) A gas bubble in a fully-developed slug flow in the bare tube (Case 2); and variation of the (b) local and (c) area-averaged film thickness along a gas bubble in the different cases

Figure 4.2-9(c) shows the area-averaged liquid film thicknesses for different cases, which is calculated by

$$\delta_{\text{ave}} = \frac{1}{L_b}\int_0^{L_b} \delta \, dz'. \tag{4-15}$$

It is seen that the average film thickness is significantly reduced in Cases 3 and 4 where the film thicknesses are about 1/10 and 1/20 of that of the bare tube, respectively. Note that the average liquid film thickness of Case 5 is much larger than that of Case 2, which provides more liquid flow of high temperature required for the convective heat transfer.

Thermal characteristics

The temperature contours in the gas bubble and the adjacent liquid slugs for different cases are shown in Figure 4.2-10. In Cases 3 and 4, the temperatures of the bubble and liquid film below the bubble quickly equilibrate to the wall temperature because of the small thermal capacity (low density of the bubble and small volume of the thin liquid film), while the temperatures of the adjacent liquid slugs near the wall are higher than the wall temperature because of the large thermal capacity.

The bubble-induced liquid circulation in Cases 3 and 5 is a very effective way of mixing hot and cold fluids. In Case 5 with a desirable flow arrangement for the convective heat transfer enhancement, the bubble pushes the hot liquid in the porous tube out to the annular gap adjacent to the tube wall. Then, the hot liquid flows downward, while being cooled by the tube wall, and back into the porous tube behind the bubble.

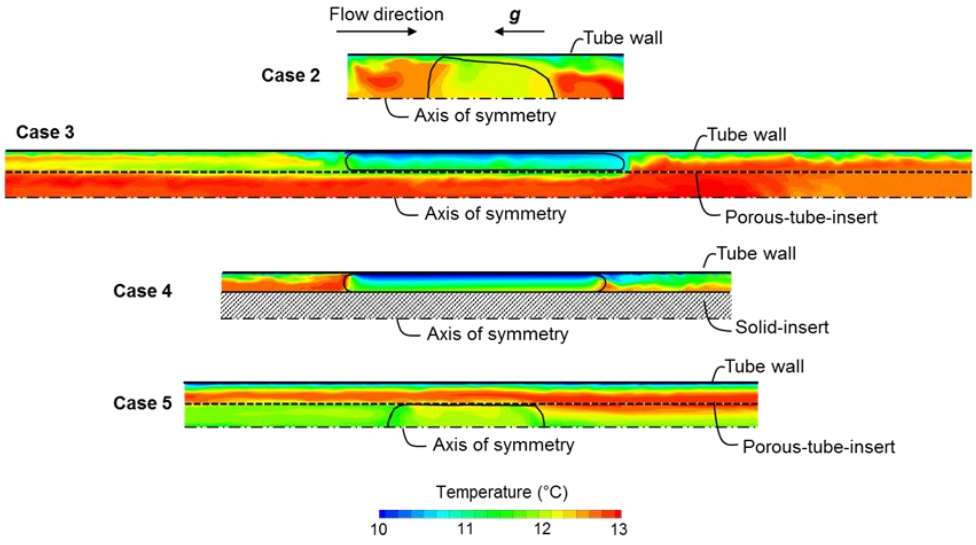

Figure 4.2-10 Temperature contours in a gas bubble and the adjacent liquid slugs in different insert cases

The variations of the bulk temperatures in the slug units for all cases are shown in in Fig. 4.2-11(a). The bulk temperatures are calculated using Eq. (4-6) in the fully-developed region ($98< z/D <111$). In Fig. 4.2-11(a), the big drops of the bulk temperatures

in the bubble region are observed for all cases except Case 5. Detailed discussion on the results for Cases 1 and 2 was given in Section 4.2.1.

Figure 4.2-11(b) shows the local wall heat fluxes in the slug units for all cases, which were calculated from Eq. (4-7). It is observed that the heat fluxes reach the peak behind the bubble tail for all cases except Case 5, because of the highest liquid velocity near the wall (Fig. 4.2-8) and then rapidly drop in the bubble region lined with a thin liquid film, to a lower value than that of the liquid-only flow for Cases 3 and 4. In contrast, in Case 5, the heat flux is the highest near the bubble head where the liquid velocity near the wall is increased and quickly drops into the liquid slug of the low velocity (Fig. 4.2-8). It is noteworthy that for the cases using the PTI, small fluctuations of the wall heat fluxes in the liquid slug regions due to the small jet flows through the pores of the PTI (Fig. 4.2-5 and 4.2-6).

Figure 4.2-11(c) presents the local Nusselt numbers in a slug unit, which was calculated using Eq. (4-8). Note that for Case 4 using a solid insert, the hydraulic diameter, which is two times of the annular gap, was used as the length scale for the Nusselt number. In general, the trends of the variations of the Nusselt number are similar to those of the heat flux variations.

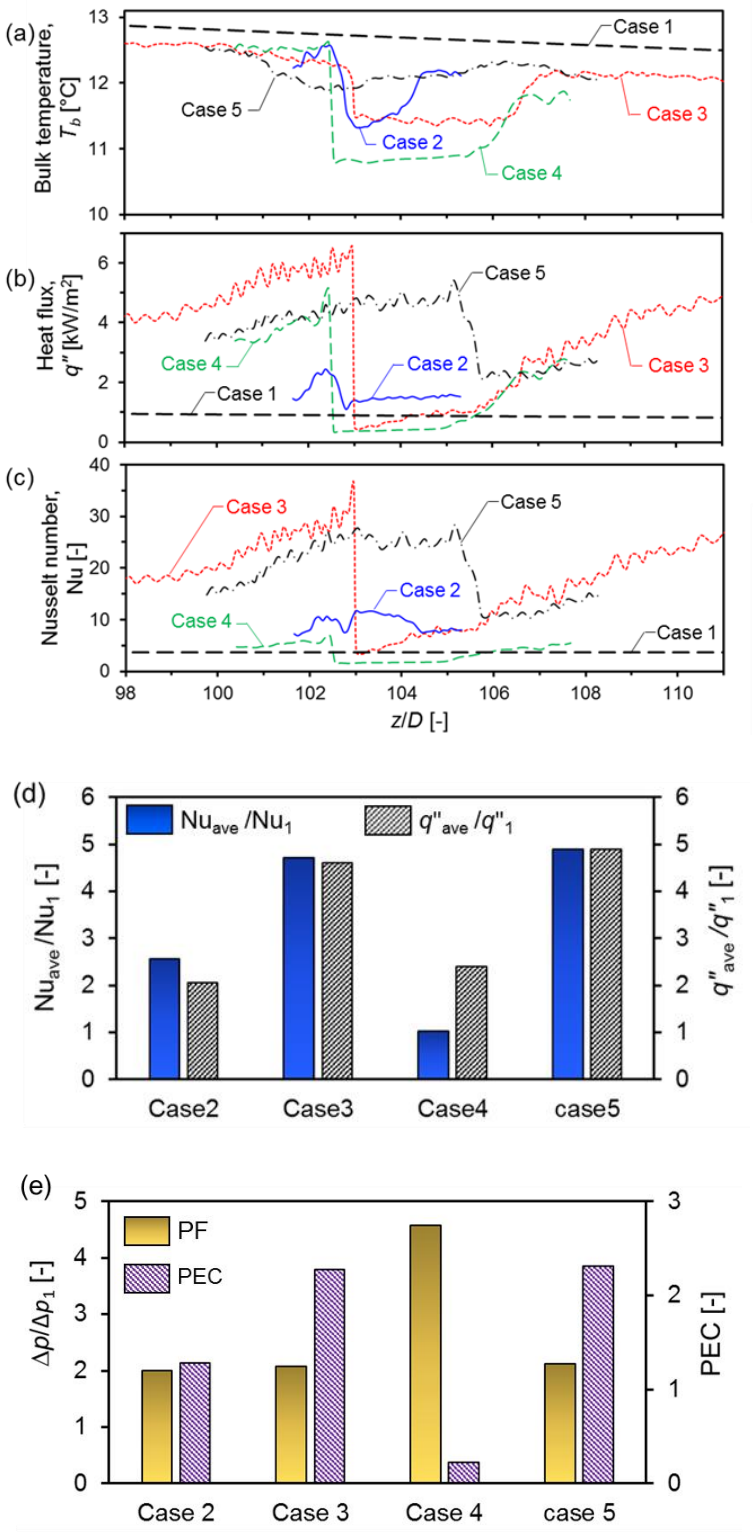

Figure 4.2-11 Variations of (a) the local bulk mean temperature; (b) the local heat flux; (c) the local Nusselt number. Comparison of (d) the normalized average Nusselt number and heat flux; and (e) the normalized pressure drop and performance evaluation criteria (PEC) calculated over a slug unit

The average heat fluxes and Nusselt numbers over the slug unit for all cases are normalized with Case 1 and compared in Fig. 4.2-11(d). It is clearly shown that Cases 3 and 5 with the PTI stand out for both heat flux and Nusselt number. The average Nusselt number for Cases 3 and 5 are 17.23 and 17.91, respectively, which are about 5 times greater than that of the liquid-only flow (Nu=3.66). Case 4 using a solid insert is the worst insert design (Nu=3.74) with no major gain as compared to the liquid-only flow. The liquid circulation through the PTI increases the velocity near the wall, which leads to the convective heat transfer enhancement.

Figure Fig. 4.2-11(e) compares the computed pressure drop for all cases that were normalized with Case 1 (pure liquid flow) as well as the performance evaluation criteria (PEC) to consider both heat transfer enhancement and pressure drop penalty

$$\mathrm{PEC} = \frac{\left(\mathrm{Nu}/\mathrm{Nu}_1\right)}{\left(\Delta p/\Delta \mathrm{p}_1\right)}\,, \tag{4-16}$$

It was found that the overall performances of the porous-tube-inserts (Cases 3 and 5) are much higher than the other cases (Cases 2 and 4). In particular, using the solid-insert (Case 4) led to an excessive pressure drop of about 4.5 times higher than that of the pure liquid flow, resulting in a poor PEC of about 0.2. On the other hand, the maximum PEC of 2.31 was achieved for Case 5.

The annular gap dimension (or porous tube diameter) for Cases 3 and 5 using the PTI is an important design parameter in determining the length of bubble and liquid slug and affecting the heat transfer performance. In the following section, numerical simulations were performed for different annular gap dimensions in a fixed heat transfer tube diameter to find an optimum gap dimension for the maximum overall heat transfer.

4.2.3 Effect of gap dimension on slug flows and heat transfer

Table 4.2-1 lists the five different annular gap dimensions (Δ) in the PTI cases used for the numerical simulations. In the table, *R* and *r* are the radii of the heat transfer and porous insert tube, respectively. The annular gap (Δ) ranges from 0.6 to 2.4 mm with a fixed heat transfer tube diameter of 6.3mm. An aspect ratio (AR) is the ratio of the bubble flow area (BFA) to the tube diameter:

$$\mathrm{PEC} = \frac{\left(\mathrm{Nu}/\mathrm{Nu}_1\right)}{\left(\Delta p/\Delta \mathrm{p}_1\right)}, \tag{4-17}$$

The bubble flow (BFA) in Case 3 is two times of the annular gap (2Δ), whereas the BFA in Case 5 is the porous tube diameter (=2*r*). In Table 3, the aspect ratio (AR) considered for both Cases 3 and 5 has almost the same ranges of 0.2< AR <0.77.

Table 4.2-1 Values of the annular gap, bubble flow area, and aspect ratio of Cases 3 and 5 used for a parametric study

Case#	*R* (mm)	Δ (mm)	*r* (mm)	AR (-)
3a	3.15	0.6	2.45	0.19
3b	3.15	1.0	2.05	0.32
3c	3.15	1.4	1.65	0.44
3d	3.15	1.8	1.25	0.57
3e	3.15	2.4	0.65	0.76
5a	3.15	0.6	2.45	0.77
5b	3.15	1.0	2.05	0.65
5c	3.15	1.4	1.65	0.52
5d	3.15	1.8	1.25	0.40
5e	3.15	2.4	0.65	0.21

As discussed earlier, the convective heat transfer occurs mainly in the liquid slug regions. Figures. 4.2-12(a-b) illustrates the dimensional changes of the fully-developed

bubble and liquid slug for different the aspect ratio (AR) of Cases 3 and 5. It is observed in Fig. 4.2-12(a-b) that by increasing the aspect ratio (AR), the bubble and liquid slug are shortened for both cases. The lengths of the liquid slug and bubble for different aspect ratio (AR) are presented in Fig. 4.2-12(c). The lengths of the liquid slugs and bubble decreases with increasing aspect ratio and approaches to that of the bare tube (Case 2). More elongated bubble (for smaller aspect ratio) creates a stronger liquid circulation in a longer liquid slug. Note that in Case 5e, a small inclined baffle was used at the entrance of the porous tube to guide the bubbles into the porous tube.

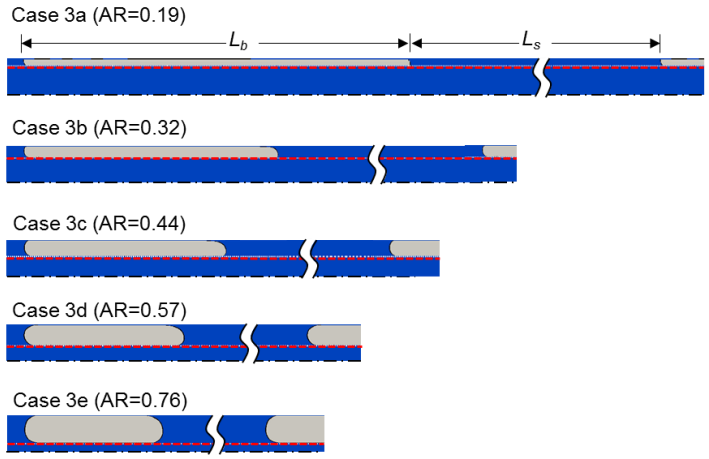

(a)

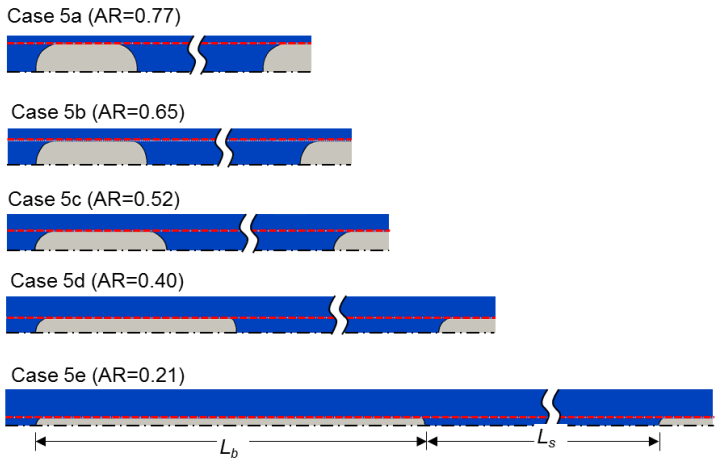

(b)

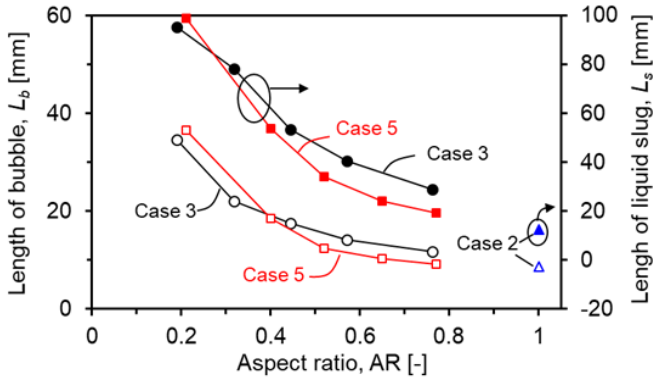

(c)

Figure 4.2-12 Effect of aspect ratio (AR) on flow pattern in (a) Case 3; (b) Case 5; and (c) the calculated length of gas bubble and liquid slug for different cases

As discussed in the previous section, a thinner liquid film is preferred because of a small thermal resistance for the convective heat transfer but provides less thermal capacity. Figure 4.2-13 shows the computed average liquid film thickness (δ) around a bubble for different aspect ratios (AR). The film thicknesses were obtained by averaging ten bubbles over an entire length of each bubble as previously discussed. It is seen that in Case 3 as the aspect ratio (AR) increases, the film thickness also increases. The liquid films in Case 3 ranges from 30μm to 95μm. Note that the film thickness in Case 5 decreases, as the diameter of the porous tube increases, and therefore the annular gap decreases, according to the definition of the aspect ratio in Eq. (4-17).

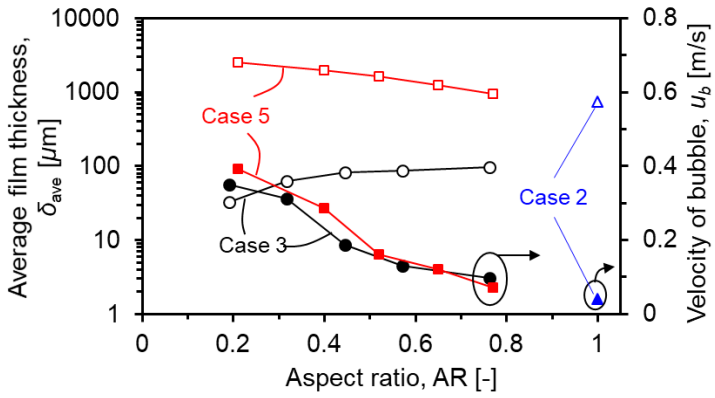

Figure 4.2-13 Effect of aspect ratio on the average liquid film thickness and bubble velocity

The bubble velocity can be used to characterize the flow fields and liquid circulations in a liquid slug unit for convective heat transfer. Larger bubble velocity intensifies the liquid circulation to augment the convective heat transfer. Figure 4.2-13 the effect of the aspect ratio (AR) on the bubble velocity for different cases. As shown, by increasing AR, the bubble moves slower due to the increased flow area for both cases, and approach to that of the bare tube (Case 2).

The convective heat transfer enhancement by the bubble-induced liquid circulation using a PTI can be quantified by the averaged Nusselt number. Figure 4.2-14 shows the effect of aspect ratio on the average Nusselt number for Cases 3 and 5. The averaged Nusselt numbers were calculated over a fully-developed region ($90<z/D<130$). It is seen that all cases using a PTI have higher average Nusselt number than those of liquid-only flow (Case 1) and two-phase slug flow (Case 2) in a bare tube. Interestingly, there exists an optimum aspect ratio (AR) for a maximum of the average Nusselt number in both cases. For Case3, the maximum average Nusselt number of 17.6 was achieved with AR=0.57 of Case 3d (Table 3). For Case 5, the maximum average Nusselt number of 18.24 was obtained for AR=0.65, of Case 5b.

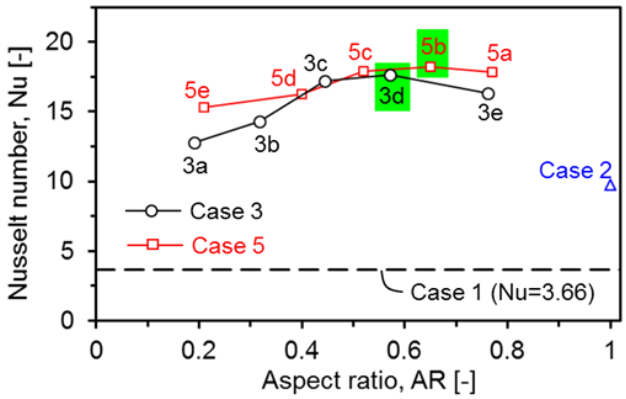

Figure 4.2-14 Effect of the aspect ratio on the average Nusselt number for Cases 3 and 5

It is seen from Fig. 4.2-14 that all of the PTI cases considered in this study have higher Nusselt number than that in liquid-only flow (Case 1) and slug flow in bare tube (Case 2). Additionally, it is interesting to see that there exist an optimum aspect ratio in both PTI cases where the Nusselt number is maximum. In Case3, the maximum Nusselt number of 17.6 was achieved for AR=0.57, which belongs to Case 3d in Table 4.2-1. Also, in Case 5, the maximum Nusselt number of 18.24 was obtained for AR=0.65, which corresponds to Case 5b in Table 4.2-1. The complicated variation of the averaged Nusselt number with the aspect ratio in the PTI cases is determined by the following factors:

- The magnitude of liquid axial velocities near the tube wall (in the annular gap region): higher velocity causes a larger convective heat transfer
- The length (area) occupied by the high liquid velocity zone near the wall (i.e. near the bubble tail region)
- The liquid film thickness in the bubble region: larger film thickness provides higher convective heat transfer rate

4.2.4 Summary

Computational fluid dynamics (CFD) simulations were carried out to investigate the convective heat transfer enhancement in non-condensing slug flows using capillary-assisted phase separation. As such, the air-water slug flow and heat transfer without phase change in a vertical upward direction was considered where a porous-tube-insert was suspended in the main tube. Simulation results show that the capillary phase separation prevented the bubbles to penetrate through the pores of the porous tube. Therefore, depending on the front end of the porous tube, two different scenarios may occur; a closed front prevented the bubbles from entering the porous tube keeping the bubbles in the

annular gap; an open front allows the bubbles to flow through the porous tube. It was found that a buoyancy-induced counter flow of the bulk liquid inside and outside of the porous tube creates internal liquid circulations-micron-scale liquid circulations through the pores and the bulk mili-scale circulations around the bubbles-leading to an increased velocity near the wall and accordingly an enhanced convective heat transfer. Finally, it was found that there exists an optimum dimension of the annular gap between the tube wall and porous tube for the maximum Nusselt number. The intriguing variation of the Nusselt number with the gap dimension is explained by the following factors:

- The magnitude of the liquid velocities near the tube wall,
- The length (area) occupied by the high liquid velocity zone near the wall (i.e. near the bubble tail region), and
- The film thickness in the bubble region. The present study shows that the average Nusselt number by using a porous-tube-insert could be about five times higher than that of a pure liquid flow in a bare tube.

5 CHAPTER 5: FLOW CONDENSATION ENHANCEMENT

This chapter discusses a numerical study on condensation heat transfer of condensing flows. First, the computational formulation for phase change simulation is presented and then validation studies are performed using the available classical problems. Next, the performance of capillary phase separation using a porous-tube-insert (PTI) is investigated to achieve a flow condensation enhancement. As such, a vertical upward slug flow is considered because it can be simulated as a 2-D axisymmetric problem. The preliminary numerical results of flow condensation using a porous-tube-insert (PTI) are compared to those of a bare-tube condenser.

5.1 CONDENSATION MODEL

5.1.1 Governing equations

The modeling of condensing flow based on the VOF method is an extension of the adiabatic two-phase flow model described in Section 2.1. This method treats each phase as an incompressible immiscible fluid and the phase distribution is determined using phase fraction (α) that is a scalar variable for the phase fraction of one phase in a computational cell. Both fluids are assumed to be Newtonian with constant density and viscosity. The governing equations consist of the mass, momentum, energy, and phase-fraction (α) equations.

The continuity equation is modified with a source term ($\dot{v}_c$) representing the volumetric mass generation per unit volume due to phase change

$$\frac{\partial}{\partial t}(\rho)+\nabla\cdot(\rho\boldsymbol{u})=\dot{v}_c\,, \tag{5-1}$$

where $\dot{v}_c$ is the dilation rate. The momentum equation (refer to Section 2.1):

$$\frac{\partial}{\partial t}(\rho\boldsymbol{u})+\nabla\cdot(\rho\boldsymbol{u}\boldsymbol{u})=-\nabla p+\nabla\cdot(\mu\nabla\boldsymbol{u})+\rho\boldsymbol{g}+\boldsymbol{F}\,. \tag{5-2}$$

where $\boldsymbol{u}$ denotes the velocity vector, p the pressure. An energy equation [Eq. (5-3)] is employed to solve for the enthalpy (i), where the volumetric heat source term ($\dot{q}_c$) accounts for the latent heat released in condensation. A thermal energy transport equation is employed to solve for the enthalpy, where pressure transport and viscous dissipation effects and pressure transport are assumed negligible compared to the dominant convective and conduction in phase change process [135, 136] and is given by

$$\frac{\partial}{\partial t}(\rho i)+\nabla\cdot(\boldsymbol{u}\rho i)=\nabla\cdot(k\nabla T)-\dot{q}_c\,, \tag{5-3}$$

where T is temperature, k is thermal conductivity, and $\dot{q}_c$ is the volumetric heat source term to account for the latent heat released during condensation.

Finally, the phase fraction equation is modified with a generation source term ($\dot{\alpha}_c$) to account for the change in liquid (or vapor) volume fraction as a result of condensation, and is given by

$$\frac{\partial}{\partial t}(\alpha)+\nabla\cdot(\boldsymbol{u}\alpha)+\nabla\cdot\left[\boldsymbol{u}_r\alpha(1-\alpha)\right]=\dot{\alpha}_c\,. \tag{5-4}$$

where the phase fraction (α) within a cell and the motion of interface.

In the above equations, the bulk properties such as density ρ, viscosity μ, thermal conductivity k, and specific heat capacity c_p are evaluated as arithmetic phase-fraction weighted averages in each computational cell. The fluid specific heat is evaluated using a

mass weighted average in each computational cell and is given by

$$c_p = \frac{\alpha_L \rho_L c_{p,L} + \alpha_V \rho_V c_{p,V}}{\rho}. \tag{5-5}$$

The liquid and vapor specific heats are assumed constant. Therefore, the fluid enthalpy can be related to temperature and is given by

$$i = c_p \left(T - T_{sat}\right). \tag{5-6}$$

The enthalpy of phase change (latent heat) is not included in Eq. (5-6) because it was accounted in the volumetric heat source term ($\dot{q}_c$) in Eq. (5-3).

The governing equations [(5-1)-(5-4)] are discretized and numerically solved following the finite volume approach described in Section 2.1.

5.1.2 Condensation heat transfer model

The phase change model of Rattner and Garimella [136] is adopted in this study. Rattner and Garimella [136] developed a phase change model that operates only on the volumetric field data (e.g. *T*, *i*, α) in interface cells. In this model, the phase-change heat rate ($\dot{q}_c$) is defined for interface cells by applying limitation criteria as below

$$\dot{q}_c = \max\left(\dot{q}_{\mathrm{c,o}}, \dot{q}_{\mathrm{lim,mass}}, \dot{q}_{\mathrm{lim,CFL}}\right), \tag{5-7}$$

in the above equation, $\dot{q}_{c,o}$ is an initially evaluated phase-change heat transfer and is given by

$$\dot{q}_{\mathrm{c,o}} = \frac{\rho c_p \left(T - T_{sat}\right)}{\Delta t}, \tag{5-8}$$

where Δt is the simulation time-step. This approach resembles the method of empirical rate parameter used in the previous works by other researchers [137-139]. [137-139]. However, in this model, the phase-change heat transfer is specified to force the interface at each time

step to be in saturation temperature and reach the equilibrium condition, and thus the internal heat transfer resistance is negligible. Conceptually, the present model assumes that the interface cells reach the equilibrium condition instantaneously, and thus have negligible internal heat-transfer resistance. A phase change mass conservation criterion should be applied in each cell during a time step to ensure that the condensed mass in a computational cell does not exceed the mass of vapor present in that cell and is given by

$$\dot{q}_{\text{lim,mass}} = -\frac{\alpha_V \rho_V i_{LV}}{\Delta t}, \tag{5-9}$$

where $\alpha_V \rho_V$ is the mass- per-volume of vapor in a computational cell and $i_{LV}/\Delta T$ is the heat transfer per-mass for complete condensation of the vapor during a single time step. Similar to the CFL condition for numerical stability in an advection simulation, the maximum volume for the condensation in a computational cell in each time step is equal to the volume of that certain cell. This is ensured by limiting the local volumetric rate of volume sinking to $1/\Delta t$ as below

$$\dot{q}_{\text{lim,CFL}} = -\frac{i_{LV}}{\Delta t}\left(\frac{1}{\rho_V} - \frac{1}{\rho_L}\right), \tag{5-10}$$

where $\left(1/\rho_V - 1/\rho_L\right)$ is the change of specific volume due to condensation.

Once $\dot{q}_c$ is determined by Eq. (5-7), the volumetric generation ($\dot{v}_c$) and phase-fraction generation ($\dot{\alpha}_c$) terms are computed by, respectively

$$\dot{v}_c = \frac{\dot{q}_c}{i_{LV}}\left(\frac{1}{\rho_V} - \frac{1}{\rho_L}\right), \tag{5-11}$$

$$\dot{\alpha}_c = -\frac{\dot{q}_c}{\rho i_{LV}}. \tag{5-12}$$

where $\dot{v}_c$ is the volumetric generation and $\dot{\alpha}_c$ is the phase-fraction generation.

5.2 MODEL VALIDATIONS

5.2.1 Horizontal film condensation (Stefan problem)

The condensation model is tested for grid independency and accuracy for film condensation over an infinite horizontal plane. This is a simple configuration with insignificant dynamic effects where the vapor condenses to form a liquid film on the surface of an isothermal plate in a quiescent vapor. This is a classical problem and similar to the validation studies performed in previous works in literature [136, 139].

Assuming a linear temperature profile from the bottom wall (T_w) to the interface (T_{sat}), a control volume analysis produces an analytical solution for the condensate film thickness

$$\delta_{an}(t) = \left[2t \left(\frac{k}{\rho c_p} \right)_L \left(\frac{1}{2} + \frac{h_{LV}}{c_{p,L}\Delta T} \right)^{-1} \right]^{1/2}, \tag{5-13}$$

Table 5.2-1 lists the thermophysical fluid properties and simulation conditions. Isobutene used as working fluid because of its moderate liquid-to-vapor property ratios and latent heat that helps to reduce the computational time. For high latent heat and property ratios, the simulation requires finer mesh and a smaller time step to properly resolve the steep gradient and increased scale for heat and mass flux magnitudes. The wall subcooled temperature is chosen to be ΔT=5°C.

Table 5.2-1 Thermophysical fluid properties and simulation conditions

Fluid property (isobutene at 20°C)	Liquid	Vapor
Density, ρ [kg/m^3]	590	7
Dynamic viscosity, μ [kg/m-s]	2×10^{-4}	8×10^{-6}
Thermal conductivity, k [W/m-K]	0.15	0.02
Specific heat, c_p [kJ/kg-K]	2.5	1.7
Surface tension, σ [N/m]	0.01	
Enthalpy of phase change, i_{LV} [kJ/kg]	366	
Simulation parameters		
Domain height [mm]	1	
Domain width [mm]	2	
Wall subcooled, (T_{sat}-T_w) [°C]	5	

A 2-D rectangular domain is used with horizontal and vertical dimensions of 2mm and 1mm, respectively (Fig. 5.2-1). The mesh is generated with five cells per horizontal row while the mesh is graded in the vertical direction with the mesh height in the first bottom row being 1/3 of that in the uppermost row. The domain represents a section of an infinitely deep condensing film. The bottom wall temperature is set to T_w=15°C, and the top "freestream" boundary is set to the saturation temperature of T_{sat}=20°C. The domain is initialized with a uniform temperature of $T(t=0)=T_{sat}$=20°C and filled with all vapor. The initial film thickness is also assumed to be zero.

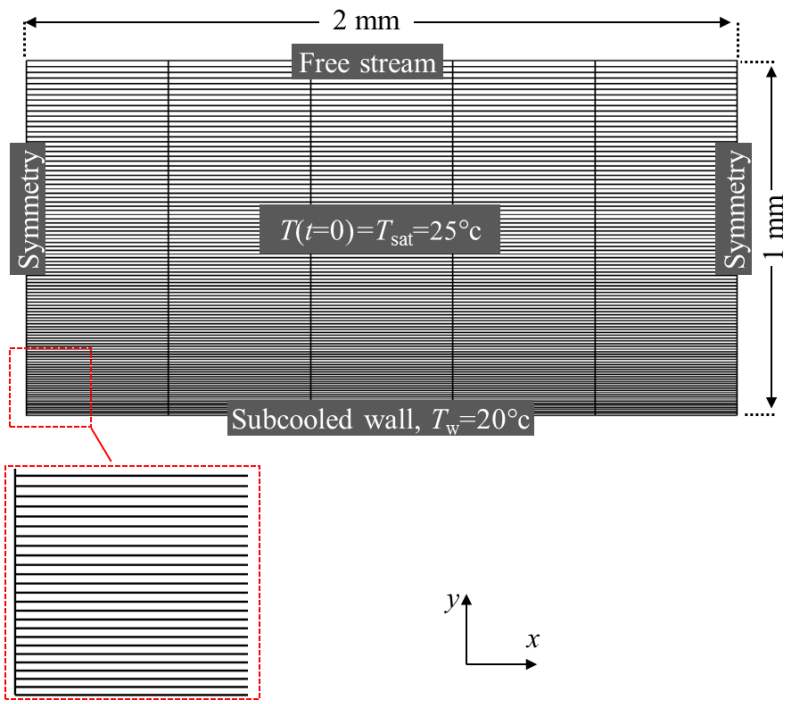

Figure 5.2-1 Computational geometry for horizontal film condensation (Stefan problem)

The grid independency was studied for n=100, 150, and 200 rows in the y-direction. Figure 5.2-2(a) shows the development of the liquid film thicknesses by time. The variation of the numerical film thickness for different cases are compared to the exact solution [Eq. (5-13)] in Fig. 5.2-2(b). The film thickness are determined using the threshold value of α=0.5.

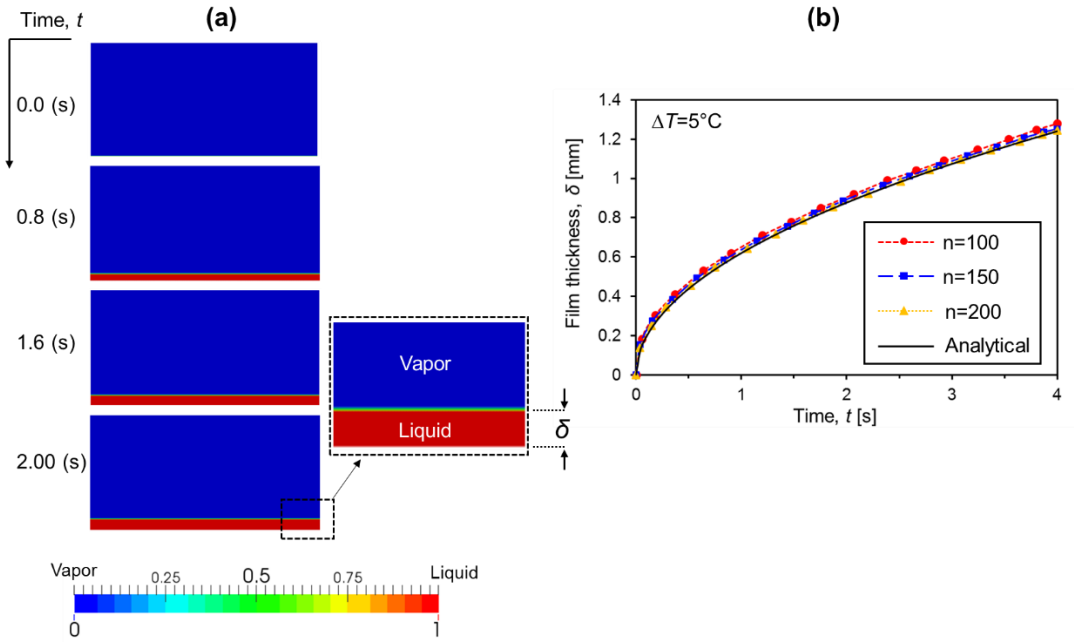

Figure 5.2-2 (a) Horizontal film condensing film development (liquid in red, vapor in blue); (b) comparison of the numerical results of film thickness with the exact analytical solution

The averaged errors in calculation of the liquid film thickness are computed by

$$e = \frac{\sum_i 100 \times \left| \delta_{CFD} - \delta_{an} \right| / \delta_{an}}{i}, \tag{5-14}$$

The computed errors are 5.4%, 3.2% and 2.9% for n=100, 150, and 200, respectively. This shows the converging trend of the accuracy of the numerically predicted film thickness with increasing mesh number and the small errors means good agreement of the numerical results with the exact solution.

5.2.2 Falling-film condensation (Nusselt problem)

Laminar falling-film condensation over a vertical isothermal plate (Nusselt problem) is selected as another classical problem for validation of the condensation simulation Nusselt [88] assumed that the temperature varies linearly from wall (T_w) to interface (T_{sat}),

and showed that the film thickness, velocity profile, and heat transfer coefficient may be derived by

$$\delta_{an} = \left[\frac{3\Gamma \mu_L}{\rho_L (\rho_L - \rho_V) g} \right]^{1/3}, \tag{5-15}$$

$$u_{an} = \frac{3\Gamma}{\rho_L \delta} \left[\frac{x}{\delta} - \frac{1}{2} \left(\frac{x}{\delta} \right)^2 \right], \tag{5-16}$$

$$h_{an} = \frac{k_L}{\delta_{an}}, \tag{5-17}$$

where Γ is the film mass flow rate unit width of the vertical plate ($\mathrm{Re} = 4\Gamma / \mu_L$).

Figure 5.2-3 shows the 2-D rectangular simulation domain (0.4mm wide×6mm tall). A thin inlet guide vane is made to prevent inlet film waviness and avoid numerical instabilities. The inlet film thickness (72μm long) corresponds to the value obtained from Eq. (5-15). The fine meshes were used in the film region and guide vane. The film thickness is resolved with 25 mesh cells (Δx=2.88μm), and the length is meshed with 500 cells (Δy=12μm) (Fig. 5.2-3). The laminar flow for liquid film is assumed ($\mathrm{Re} = 4\Gamma / \mu_L = 42$). The wall temperature (T_w) is set to 15°C and the vapor temperature (T_v) is set to 20°C. The guide vane and outlet sections are assumed to be adiabatic surface. The liquid inlet flow is specified using the analytical temperature (linear) and velocity [Eq. (5-16)] profiles. In the vapor bulk region, cells are graded in the *x*-direction, becoming coarser toward the freestream.

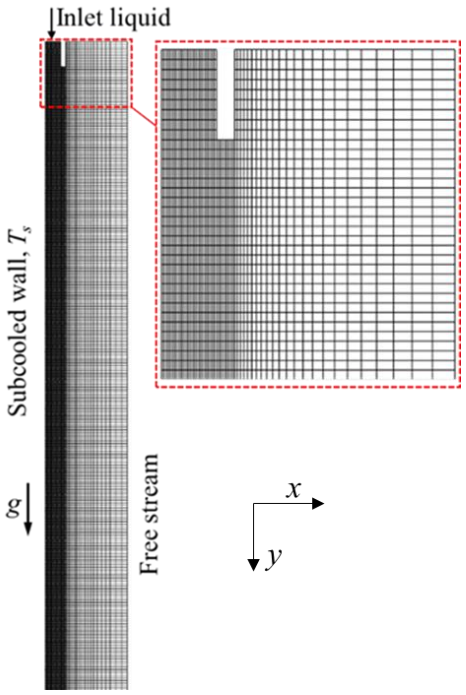

Figure 5.2-3 Computational domain for laminar falling-film condensation

Table 5.2-2 lists the simulation parameters used for the model validation. Fluid properties correspond to those of saturated isobutene at 20°C (Table 5.2-1).

Table 5.2-2 Simulation parameters for laminar falling-film condensation

Simulation parameter	Value
Inlet liquid film thickness, δ [μm]	72
Wall subcooled, (T_{sat}-T_w) [°C]	5
Inlet film Reynolds number, Re_δ [-]	42

Figure 5.2-4(a) shows the simulated condensate film profiles over the vertical subcooled wall. It is seen that the computed values of the local film thickness (δ) [Fig. 5.2-4(b)] and condensation heat transfer coefficient (h) [Fig. 5.2-4(c)] agree well with the analytical values obtained from Eq. (5-15) and (5-17), respectively.

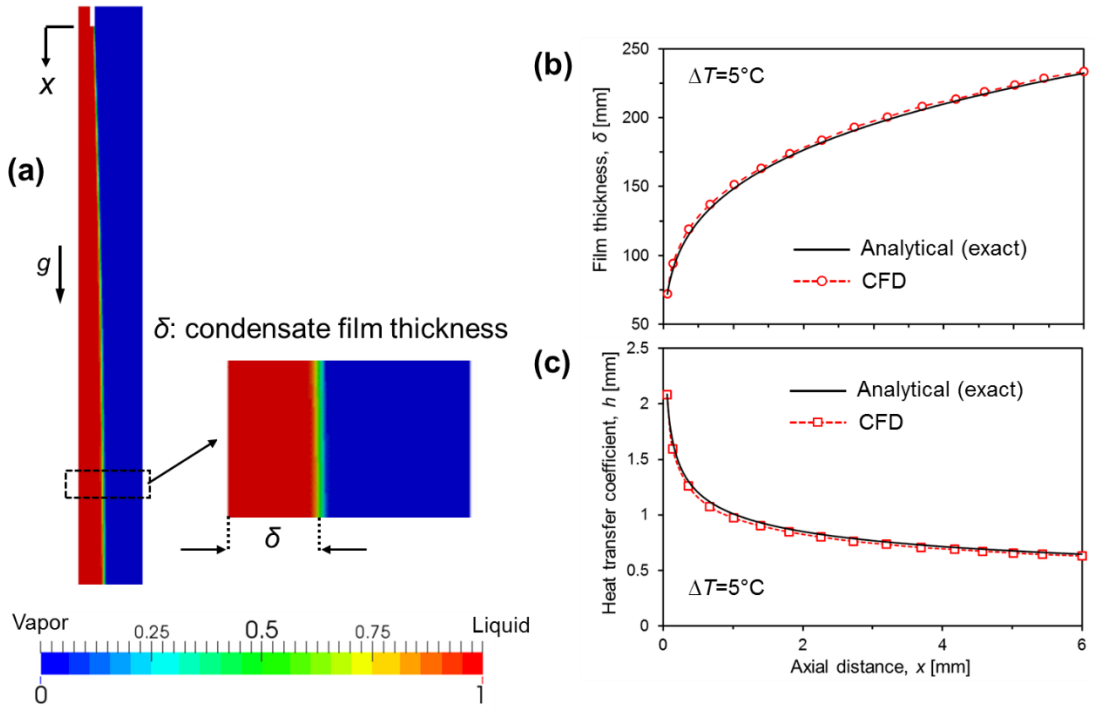

Figure 5.2-4 (a) Condensate film profile (liquid in red, vapor in blue) over vertical distance; and the local variation of (b) liquid film thickness and (c) condensation heat transfer coefficient along the vertical subcooled wall

5.2.3 Flow condensation in a tube

The numerical simulations were performed for fifteen different laminar condensing slug flows with various flow conditions for model validation purpose. The selected superficial velocities created slug flows in the fully-developed region of the vertical tube. Figure 5.2-5 shows the selected flow conditions in the Hewitt and Roberts' flow map [140] and confirms that the selected cases correspond to the slug flow regime. In this study, the maximum Reynolds number for the liquid and gas flows are 1951 and 810.3, respectively, implying that the two-phase flows are all laminar.

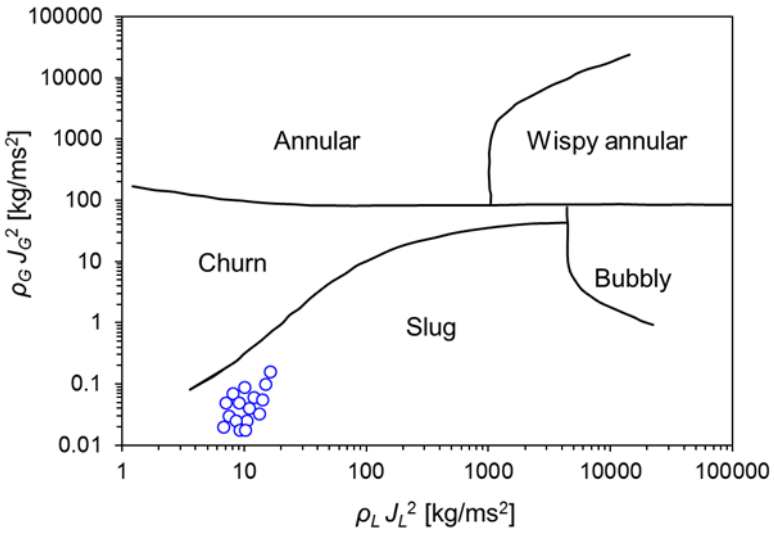

Figure 5.2-5 Simulated conditions used in this study marked in Hewitt and Roberts' flow map

For the flow condensation in vertical tubes, Shah [141] proposed a comprehensive heat transfer correlation that was the modified version of his previous correlation [142]. The correlation for vertical upflow uses the following two heat transfer equations

$$h_I = h_{LO}\left(1+\frac{3.8}{Z^{0.95}}\right)\left(\frac{\mu_L}{14\mu_G}\right)^{(0.0058+0.557\,pr)}, \tag{5-18}$$

$$h_{Nu} = 1.32\,\mathrm{Re}_{LO}^{-1/3}\left[\frac{\rho_L\left(\rho_L-\rho_G\right)g{k_L}^3}{{\mu_L}^2}\right]^{1/3}, \tag{5-19}$$

where Eq. (5-19) is the heat transfer coefficient equation for the laminar film condensation in vertical tubes [143]. h_{LO} in Eq. (5-18) is the heat transfer coefficient of the liquid phase flowing alone in the tube and is given by

$$h_{LO} = 0.023\,\mathrm{Re}_{LO}^{0.8}\,\mathrm{Pr}_L^{0.4}\frac{k_L}{D}, \tag{5-20}$$

where Re_{LO} is the Reynolds number assuming liquid phase flowing alone. These equations are used according to the heat transfer regime as defined by Shah [141] and is given by

$$h_{LO} = 0.023 \mathrm{Re}_{LO}^{0.8} \mathrm{Pr}_L^{0.4} \frac{k_L}{D}, \tag{5-21}$$

where Re_{LO} is the Reynolds number assuming liquid phase flowing alone. These equations are used according to the heat transfer regime as defined by Shah [141] and is given by

Regime I:

$$h_{TP} = h_I, \tag{5-22}$$

Regime II:

$$h_{TP} = h_I + h_{Nu}, \tag{5-23}$$

Regime III:

$$h_{TP} = h_{Nu}, \tag{5-24}$$

where Regime I occurs when We_{GT}>100 and

$$J_g \geq 0.98\left(Z + 0.263\right)^{-0.62}, \tag{5-25}$$

and Regime III occurs when when We_{GT}>20 and

$$J_g \leq 0.95\left(1.254 + 2.27Z^{1.249}\right)^{-1}, \tag{5-26}$$

where We_{GT} is the Weber number assuming all mass flowing as vapor, defined as

$$\mathrm{We}_{\mathrm{GT}} = \frac{G^2 D}{\rho_G \sigma}, \tag{5-27}$$

and J_g is the dimensionless vapor velocity defined as

$$J_g = \frac{xG}{\left[gD\rho_G\left(\rho_L - \rho_G\right)\right]^{0.5}}, \tag{5-28}$$

and Z is the correlating parameter introduced by Shah and is given by

$$Z = \left(\frac{1}{x} - 1\right)^{0.8} \mathrm{Pr}^{0.4}. \tag{5-29}$$

In the numerical simulations, the local Nusselt number is calculated by

$$\mathrm{Nu} = \frac{q'' D}{k_L\left(T_b - T_w\right)}, \tag{5-30}$$

where the local heat flux (q'') is calculated by the conduction through the first liquid layer (5 μm thick) fixed on the tube wall as below

$$q'' = -k \left. \frac{\partial T}{\partial y} \right|_{r=R} , \tag{5-31}$$

where r is the radial coordinate and k is the liquid thermal conductivity. The average Nusselt number was calculated using the averaged heat flux and bulk temperature over the entire selected fully-developed domain ($55D<z<76D$) as below

$$\mathrm{Nu}_{\mathrm{ave}} = \frac{q''_{\mathrm{ave}}}{\left(T_{b,\mathrm{ave}} - T_w\right)} \frac{D}{k_L}, \tag{5-32}$$

$$q''_{\mathrm{ave}} = \frac{1}{L} \int_0^L q''\, dz, \tag{5-33}$$

$$T_{b,\mathrm{ave}} = \frac{1}{L} \int_0^L T_b\, dz, \tag{5-34}$$

where L is the total length of the selected domain. The average Nusselt numbers were calculated using Eq. (5-32) in the numerical simulation and compared with the values predicted by the Shah's correlation [141] within an error band of ±15% as shown in Fig. 5.2-6.

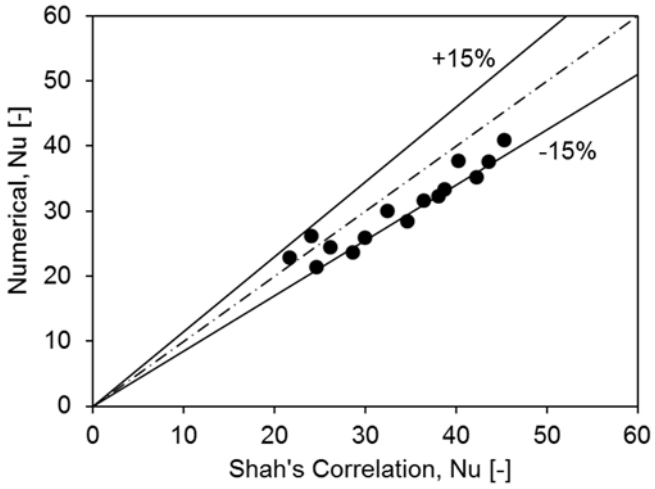

Figure 5.2-6 Comparison of the computed average Nusselt number of two-phase condensing flows with those predicted by Shah's correlation [141]

5.3 FLOW CONDENSATION ENHANCEMENT USING CAPILLARY PHASE SEPARATION

A typical flow condensation in a vertical upflow arrangement consists of various flow regimes as shown in Figure 5.3-1(a). Condensation is gradually degraded along the condenser tube due to the accumulated condensate and increased thermal resistance. Thus, the condensation enhancement is essentially important in the middle and downstream of condensers where the flow regimes are mostly slug and bubbly flow.

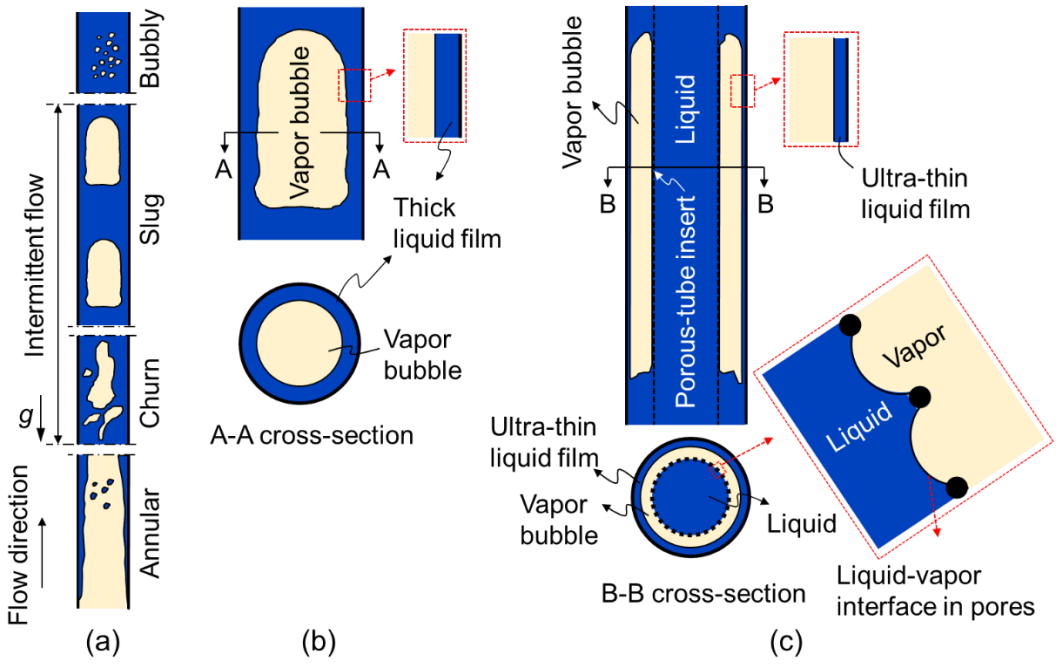

Figure 5.3-1 (a) Evolution of in-tube condensation in a vertical upflow; (b) a vapor bubble in a slug flow in a typical condenser; and (c) an elongated-ring-shape (confined) vapor bubble in the porous-tube insert (PTI) condenser with a porous-tube insert

A porous-tube insert (PTI) installed in a conventional condenser (bare-tube made of) utilizes a capillary-assisted liquid-vapor phase separation to promote a thin-film condensation throughout the condenser as shown in Fig. 5.3-1(c). The capillary phase separation of a slug flow is achieved by preventing the elongated vapor bubble from

entering the porous tube due to the capillary force at the liquid-vapor interfaces (aka meniscus) formed in the pores of the porous tube that is illustrated in Fig. 5.3-1(c). Consequently, the confined elongated bubble stays near the tube wall resulting in an ultra-thin condensate film and an increased area for the thin-film condensation, which leads to an augmented heat transfer.

5.3.1 Simulation condition

Numerical simulation of two-phase flow in a tube including a porous-tube insert is inherently a three-dimensional (3-D) system. However, in the vertical flow, due to the neutral effect of gravity in the radial direction, it is to approximate the 3-D system to a two-dimensional (2-D) axisymmetric one. Figure 5.3-2 shows the computational domain of the 2-D vertical upward slug flow in a vertical tube with a porous-tube insert (PTI). The computational domain consists of a multiscale coupled grid system as shown in Figs. 5.3-2 (c-e); A quasi-uniform mesh size of 100 μm is generated in the bulk flow region along the axial direction [Fig. 5.3-2 (c)] except near the tube wall [Fig. 5.3-2 (d)] and pores [Fig. 5.3-2 (e)]. The height of the wall boundary layer mesh was gradually refined along the radial direction toward the tube wall ranging from 100 μm in the bulk region to 5 μm in the first mesh of the boundary layer on the tube wall [Fig. 5.3-2 (d)]. The refined meshes were also created near the pores where the mesh size is 16.67×16.67 μm and twenty-eight meshes are used within a square pore [Fig. 5.3-2 (e)].

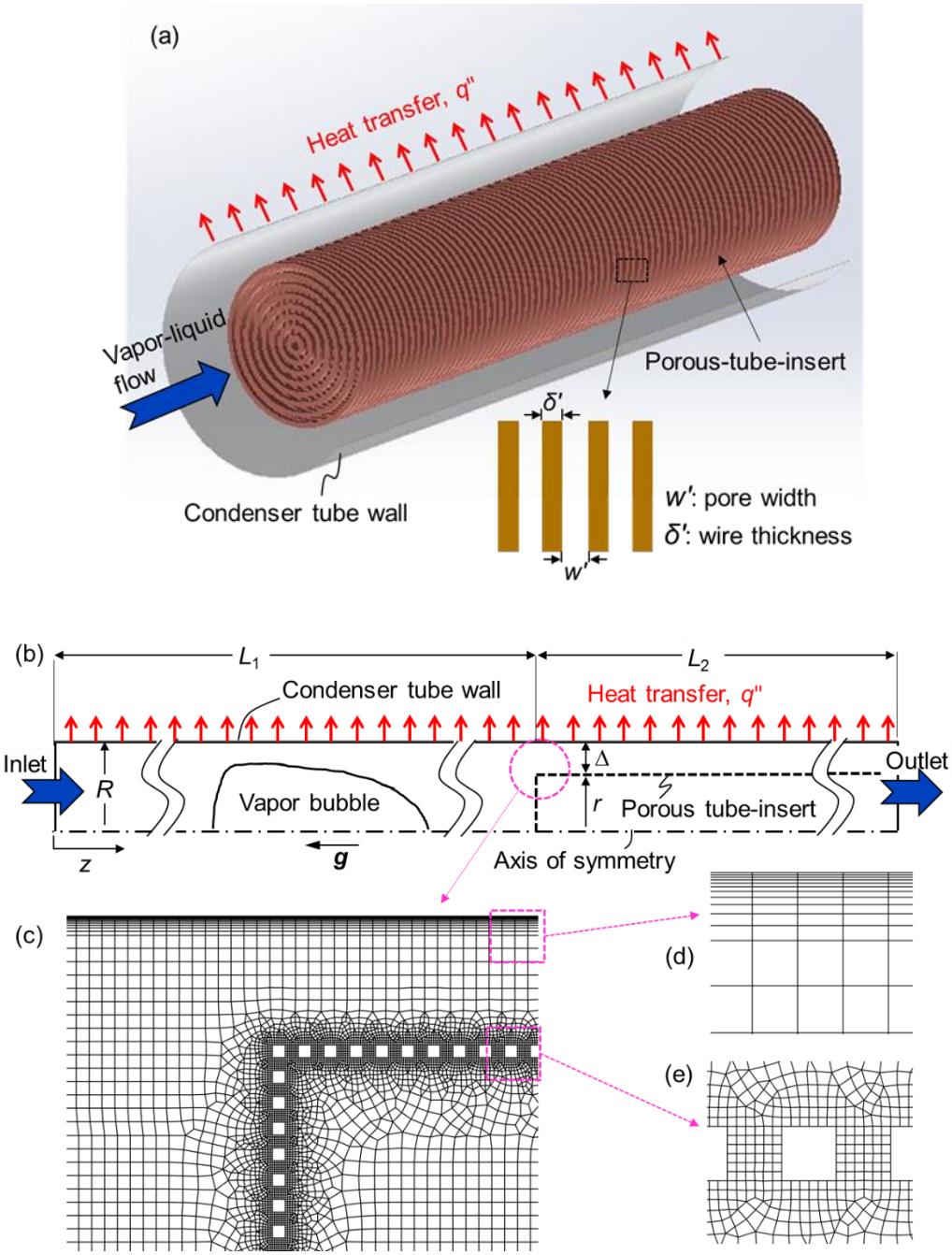

Figure 5.3-2 (a) 2-D axisymmetric system for vertical upflow slug flows in a tube with a porous-tube insert; and (b) computational domain of the slug flow; and (c) multiscale grid system used in the computational domain with refined meshes (d) near the tube wall and (e) in the vicinity of the pores

The mesh was refined near the wall to capture a thin liquid film between the wall and a vapor bubble. Computational fluid dynamics (CFD) simulation was performed to study a laminar flow condensation in a vertical slug flow. As before, isobutene used as working

fluid, whose the thermophysical properties are listed in Table 5.2-1. The main simulation parameters are also summarized in Table 5.3-1.

Table 5.3-1 Simulation parameters for flow condensation of isobutene

Simulation parameter	Value
Tube radius, R [mm]	3.150
Tube length, L [mm]	800
Porous-tube radius, r [mm]	1.650
Porous tube length, L_2 [mm]	500
Wire thickness, δ' [mm]	0.100
Pore width, w' [mm]	0.100
Void fraction, ε_i [-]	0.501
Mass flux, G [kg/m^2-s]	25.370

The wall subcooled temperature is chosen to be ΔT=5°C. The saturated isobutene was introduced from the tube inlet with a uniform velocity (u_i) and a homogenous void fraction (α_i), which allows gas bubbles to break off, and actual void fraction to be determined during the numerical simulation. It is worth mentioning that due to the absence of actual triple-phase-point, the wall contact angle is not important in this study. The liquid film thicknesses around the gas bubbles were in the range of 20 μm ~ 800 μm, which were much larger than nanoscale, where the van der Waal forces can act across the film [81, 87]. The no-slip condition was applied on each pore surface and the tube wall. The atmospheric pressure was set at the tube outlet. This study used a constant wall temperature, which was 5°C colder than the saturation temperature, so that the isobutene flow is cooled by the tube wall.

In order to study the complex hydrodynamics of two-phase flows, a transient simulation with a time step of 10^{-5} s was used. Gravitational field was also applied opposite to the flow direction to create an upward flow configuration. A mesh dependency analysis was performed in which the mesh count was increased until the computed value of the average Nusselt number in fully-developed region in slug flow was within less than 3% of the previous mesh case. Figure 4.1-2 shows a converging trend of the average Nusselt number (Nu) with the mesh number. It was found that 336,927 mesh for the bare tube, and 625,325 mesh for the case of porous-tube insert (PTI) with at least four mesh within a liquid film near the wall is sufficient to ensure a reasonable accuracy for the heat transfer calculations. Therefore, the case with 336,927 cells for bare tube and 625,325 mesh for the PTI was selected for the entire simulations in this study.

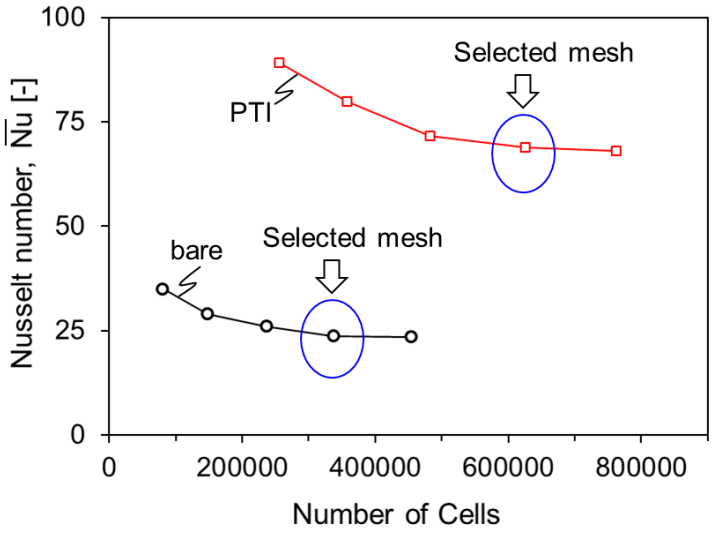

Figure 5.3-3 Grid dependency of the computational results of average Nusselt number for condensing isobutene flow in a bare tube and a PTI condenser

5.3.2 Flow condensation enhancement

Computational fluid dynamics (CFD) simulation was performed to study a laminar flow condensation of isobutene in a vertical slug flow for mass flux of G=25.37 and void fraction of ε=0.50. Figures 5.3-3 (a, b) show the numerical results for a single condensing vapor bubble and the temperature distribution around the vapor bubble in a bare tube and PTI condenser. It is seen that the vapor bubbles maintain the saturation temperature while the variation in liquid bulk temperature exists due to the convection heat transfer. It is also shown that the PTI brings the saturated vapor bubble near the tube wall, reducing the film thickness, and thus thinning the thermal boundary layer.

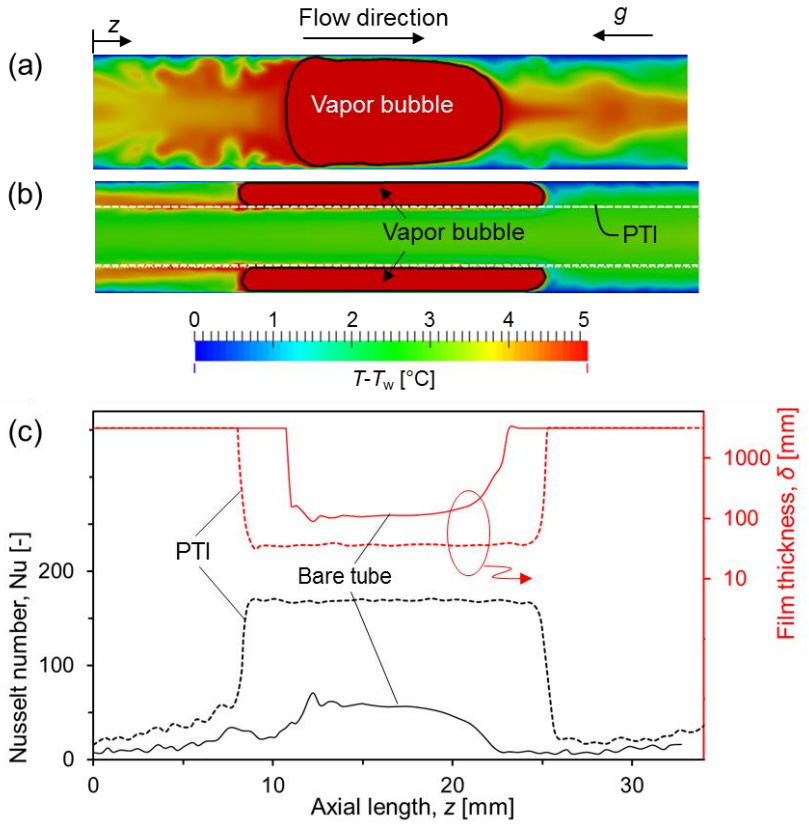

Figure 5.3-4 Numerical results of a condensing vapor bubble and temperature contour in (a) bare tube; (b) porous-tube insert; and (c) the variation of local Nusselt number and liquid film thickness around a vapor bubble

Figures5.3-3 (c) shows the computed local Nusselt numbers using Eq. (5-28) and liquid film thicknesses in the selected domain of the bare tube and PTI condenser. The interface of the bubble is defined by a line with a phase fraction (α) of 0.5. It is apparent that using the PTI significantly increases the local Nusselt number in the bubble region that is due to the substantial decrease in the film thickness resulting in a reduced thermal resistance. The film thickness around the bubble in the bare tube was ~110μm that is reduced to ~35μm in the PTI condenser. Consequently, the Nusselt number (in bubble region) was increased from ~55 in the bare tube to ~170 in the PTI condenser. In addition, the local Nusselt number in the liquid slugs near the bubble is also higher in the PTI case that is attributed to the promoted convective liquid heat transfer by liquid circulation in the PTI section, which was thoroughly explained in Chapter 4.

Figure 5.3-4 illustrates a larger simulation domain ($37D<z<76D$) of the condensing slug flow in the bare tube and PTI condenser. It is shown that once a vapor bubble reaches the entrance of the PTI ($z=48D$), it cannot flow through the mesh pores and therefore only flows through the annular gap region between the tube wall and porous tube. Enhanced condensation of the confined vapor bubbles (reduction in bubble length) in the PTI condenser is visually apparent as compared to that in the bare tube one.

The instantaneous local Nusselt numbers in the downstream region ($55D<z<76D$) are presented in Fig. 5.3-5(b). It is seen that the peak Nusselt numbers, around the vapor bubble, are significantly increased in the PTI condenser as a result of the reduced film thickness [Fig. 5.3-55.3-4(c)]. Also, the local Nusselt numbers in the liquid regions are

mostly higher in the PTI condenser as compared to those in the bare tube due to the increased velocity near the wall, especially in the back tail of the bubbles.

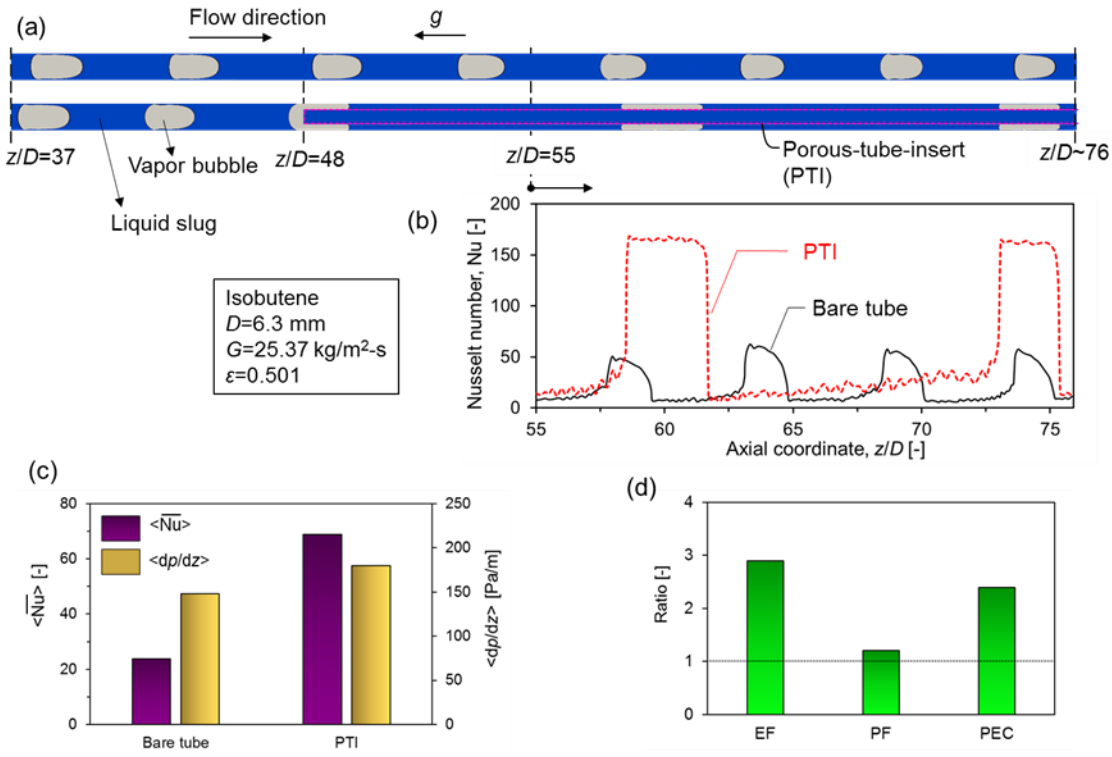

Figure 5.3-5 (a) Simulated condensing slug flow of isobutene; and (b) variation of the local Nusselt numbers in the selected downstream region in the bare tube and porous-tube insert (PTI) condenser; (c) comparison of the area-time-averaged Nusselt numbers and time-averaged pressure gradients; and (d) the enhancement factor, penalty factor, and performance evaluation criterion by using PTI

For a quantitative comparison of the heat transfer, the average Nusselt number was calculated using Eq. (5-32). The area-time-averaged Nusselt numbers as well as the time-averaged pressure gradients for the bare-tube and PTI condenser are compared in Fig. 5.3-4(c). It is shown that the average Nusselt number in the bare-tube (~24) is substantially increased in the PTI condenser (~70) while the pressure gradient is slightly increased from bare tube (~150 Pa/m) to the PTI condenser (~180 Pa/m). In order to evaluate the

condensation enhancement by using PTI, an enhancement factor (EF), penalty factor (PF), and performance evaluation criterion (PEC) is defined, respectively as below

$$\mathrm{EF} = \frac{\mathrm{Nu}_{\mathrm{PTI}}}{\mathrm{Nu}_{\mathrm{bare}}}, \tag{5-35}$$

$$\mathrm{PF} = \frac{\left(\mathrm{d}p/\mathrm{d}z\right)_{\mathrm{PTI}}}{\left(\mathrm{d}p/\mathrm{d}z\right)_{\mathrm{bare}}}, \tag{5-36}$$

$$\mathrm{PEC} = \frac{\mathrm{EF}}{\mathrm{PF}}. \tag{5-37}$$

The computed values of EF, PF, and PEC are shown in Fig. 5.3-4(d). It is seen that, for the above case study, the flow condensation heat transfer in a PTI condenser is enhanced up to 290% as compared to the bare-tube condenser (EF=2.9), which is accompanied by 20% pressure drop penalty (PF~1.2) leading to the 240% increased overall performance (PEC=2.39).

Close scrutiny reveals that the length/area occupied by the ultra-thin liquid film is a key factor determines the overall condensation heat transfer in the PTI condenser. The annular gap dimension is an important design parameter, which can influence the length/area of the confined vapor bubble. In addition, the initial length of the vapor bubble (void fraction) is another factor that affect the condensation heat transfer performance of the porous-tube insert. As such, in the following sections, numerical simulations were performed for various void fractions as well as different annular gap dimensions in a fixed condenser tube diameter to find an optimum void fraction and gap dimension for the maximum condensation heat transfer.

5.3.3 Effect of void fraction

In order to study the effect of void fraction on the condensation heat transfer performance of the PTI condenser, numerical simulations were carried out for seven different void fractions of slug flows. Figure 5.3-5 shows the variation of the vapor quality for different void fractions of isobutene flow using the logarithmic mean void fraction (LMε) model as suggested by El Hajal's et al. [144]. As shown in Fig. 5.3-6, the selected simulation cases correspond to the low vapor quality region (x<0.15). Table 5.3-2 lists the simulation conditions that were considered for this parametric study. It is worth mentioning that further increase in the void fraction (ε>0.7) substantially increased the length of the vapor bubble resulting in a significant increase in mesh number and computational time in the PTI case. Therefore, the present study uses the maximum void fraction and vapor quality of ε=0.7 and x=0.13, respectively for manageable computational loads

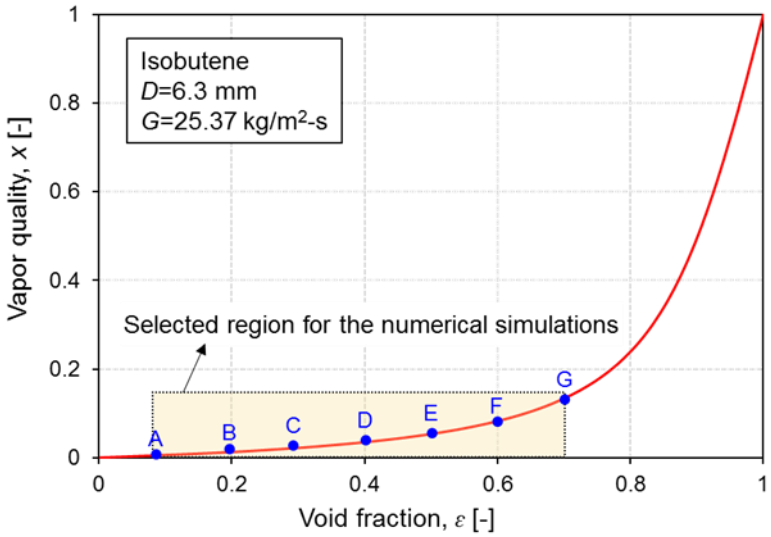

Figure 5.3-6 Variation of vapor quality (x) with void fraction (ε) for isobutene flow condensation in a tube diameter of D=6.3mm and mass flux of G=25.37 kg/m2-s computed by El Hajal's model [144]

Table 5.3-2 Test matrix to study the effect of void fraction

Case#	G (kg/m^2-s)	ε (-)	x (-)
A	25.370	0.103	0.006
B	25.370	0.207	0.014
C	25.370	0.304	0.023
D	25.370	0.399	0.034
E	25.370	0.501	0.053
F	25.370	0.606	0.084
G	25.370	0.702	0.133

Figure 5.3-7(a-b) illustrate the condensing slug flow as well as the local Nusselt numbers in the selected region ($55D<z<76D$) of a bare-tube [Fig. 5.3-6(a)] and the modulated flows using the porous-tube insert [Fig. 5.3-6(b)] for four selected cases. Note that the local Nusselt numbers are shown in a logarithmic scale.

It is seen from Fig. 5.3-6(a) that the pick Nusselt numbers in the bare tubes are generally increased and expanded by increasing void fraction due to the reduced film thicknesses around the vapor bubbles and the increased length/area occupied by the vapor bubble. In addition, the pick Nusselt numbers are more frequent in higher void fractions due to the increased number of the vapor bubble and the shorter liquid slugs.

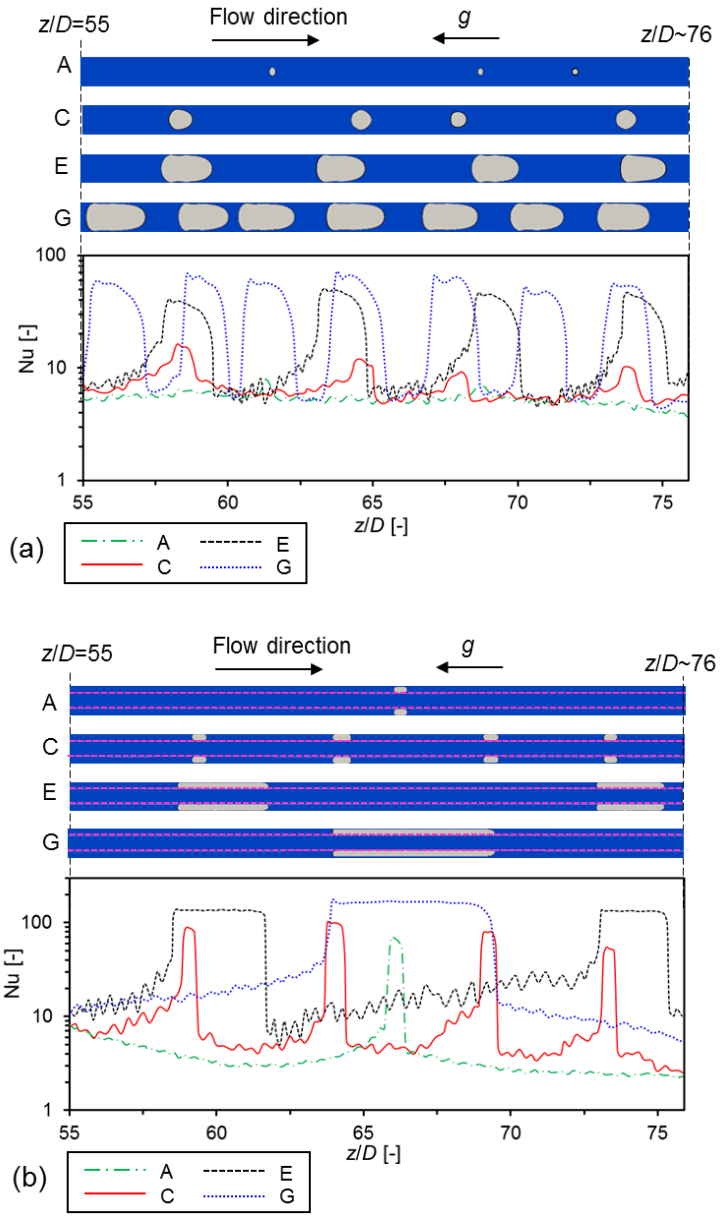

Figure 5.3-7 Effect of void fraction on flow pattern and local Nusselt numbers in a (a) bare tube; and (b) the modulated section in the PTI condenser

In the modulated flows shown in Fig. 5.3-6(b), it is seen that by increasing the void fraction, the peak Nusselt numbers are increased due to the reduced film thicknesses, however, the number of bubbles in the PTI section decreases because of the expanded liquid slugs caused by strong liquid circulations.

Figures 5.3-7 (a-b) show that the vapor bubbles merge together before entering the annular gap region in the PTI section in low void fraction (Case A, ε=0.1) [Fig. 5.3-7 (a)] and also for the case of highest void fraction (Case G, ε=0.7) [Fig. 5.3-7 (b)]. This phenomenon causes a time-lag for vapor bubbles to enter the PTI section in Case A, that is because the small bubble stays at the porous tube entrance until the diameter of the merged bubbles exceeds the porous tube diameter. This explains the existence of only one vapor bubble for Case A in Fig. 5.3-6(b).

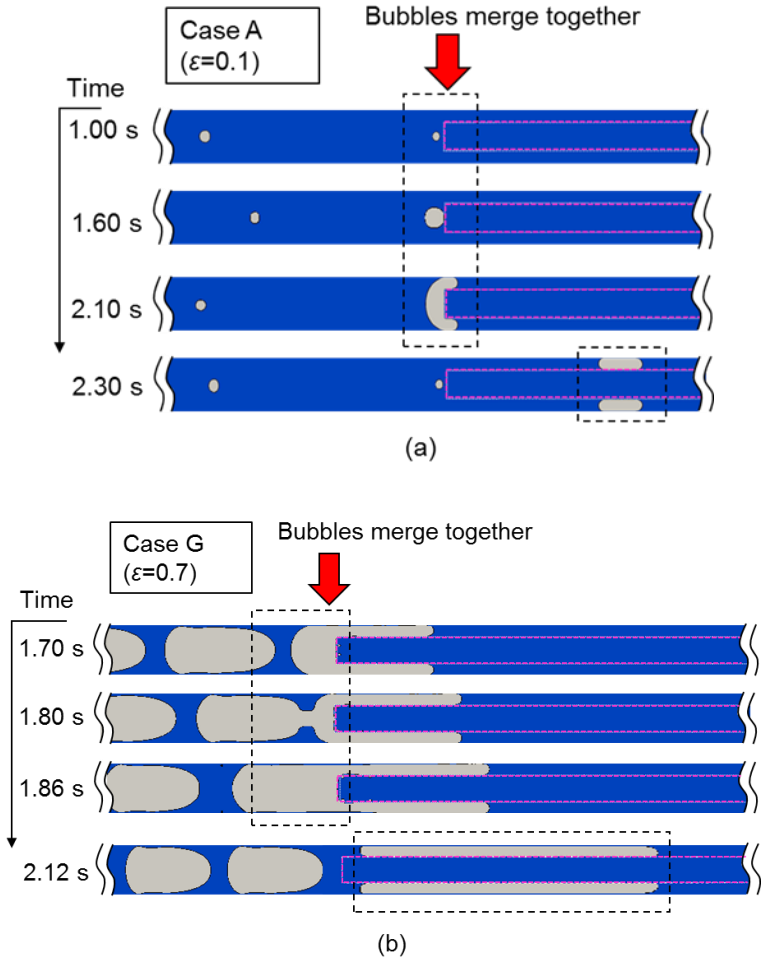

Figure 5.3-8 Illustration of bubble merging phenomena before entering the porous-tube-inset section in the case of (a) very low void fraction (ε=0.1) in Case A; and (b) high void fraction (ε=0.7) in Case G

In order to compare the condensation heat transfer performance, the area-averaged Nusselt numbers were calculated and then averaged over 3 seconds of the simulation time. Figure 5.3-8presents the area-time-averaged Nusselt numbers for all of the simulation cases considered for this parametric study. It is seen that overlay, the average Nusselt number in PTI cases higher than that in the bare tube, except at very low void fraction (ε=0.1) where there is not much difference in Nusselt number. The calculated enhancement factor (EF) shows that within the ranges of the void fraction considered in this study (0.1< ε <0.7) there exists an optimum void fraction for the maximum heat transfer enhancement such that the maximum enhancement factor of EF=2.63 was achieved for the void fractions of ε=0.5 (Case E) and ε=0.6 (Case E). However, by considering the pressure drop penalty, the maximum PEC of about 2.2 was obtained for the void fraction of ε=0.6 (Case F).

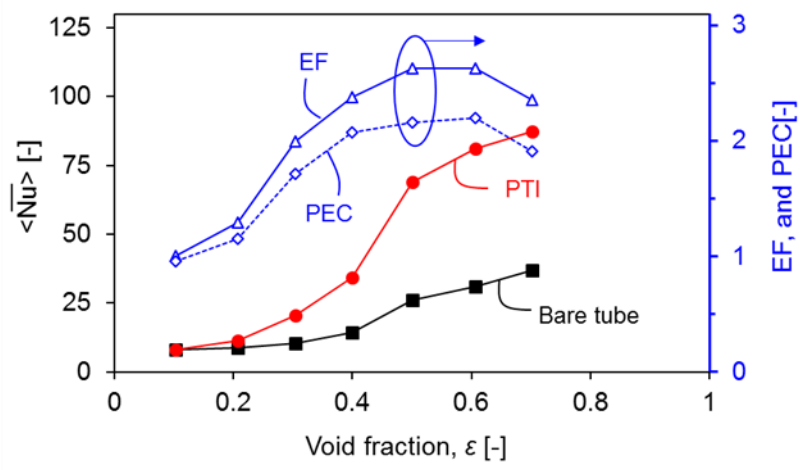

Figure 5.3-9 Variation of area-time-averaged Nusselt number in a bare tube and PTI condenser; and enhancement factor (EF) and performance evaluation criterion (PEC) in different void fractions

5.3.4 Effect of gap dimension

In order to study the effect of void The annular gap dimension between the condenser tube wall and the porous tube influences the length of the confined vapor bubble

and accordingly the area occupied by ultra-thin film near the tube wall. Therefore, it is expected that the overall condensation heat transfer changes by varying the gap dimension in PTI condenser. Therefore, numerical simulations were performed for five different gap dimension with the same flow condition. Table 5.3-3 lists all the annular gap dimensions (Δ) in the PTI cases, which used for the numerical simulations. In the table, R and r are the radii of the condenser and the porous tube, respectively. The annular gap (Δ) ranges from 0.6 to 2.4 mm with a fixed condenser tube diameter of 6.3 mm. An aspect ratio (AR) is the ratio of the bubble flow area (BFA) to the tube diameter:

$$\mathrm{AR} = \frac{\mathrm{BFA}}{2R}. \tag{5-38}$$

The bubble flow area (BFA) in the PTI condenser is two times of annular gap (2Δ).

Table 5.3-3 Values of the annular gap, bubble flow area, and aspect ratio used for a parametric study

Case#	R (mm)	Δ (mm)	r (mm)	AR (-)
a	3.15	0.6	2.45	0.19
b	3.15	1.0	2.05	0.32
c	3.15	1.4	1.65	0.44
d	3.15	1.8	1.25	0.57
e	3.15	2.4	0.65	0.76

Figures 5.3-10(a) represents the condensing slug flow in the bare tube and different PTI condensers with various gap dimensions as well as the variation of the local Nusselt number at the selected downstream region ($55D<z<76D$). It is seen that by increasing the aspect ratio (AR), the bubble and liquid slug are shortened. Note that the more elongated

bubble (for smaller aspect ratio) creates a stronger liquid circulation in a longer liquid slug. It is also seen that, generally, the peak Nusselt number decreases by increasing the gap dimension due to the reduction of film thickness. On the other hand, the number of peak Nusselt numbers increases by increasing the aspect ratio due to the increased number of vapor bubbles in a fixed selected domain.

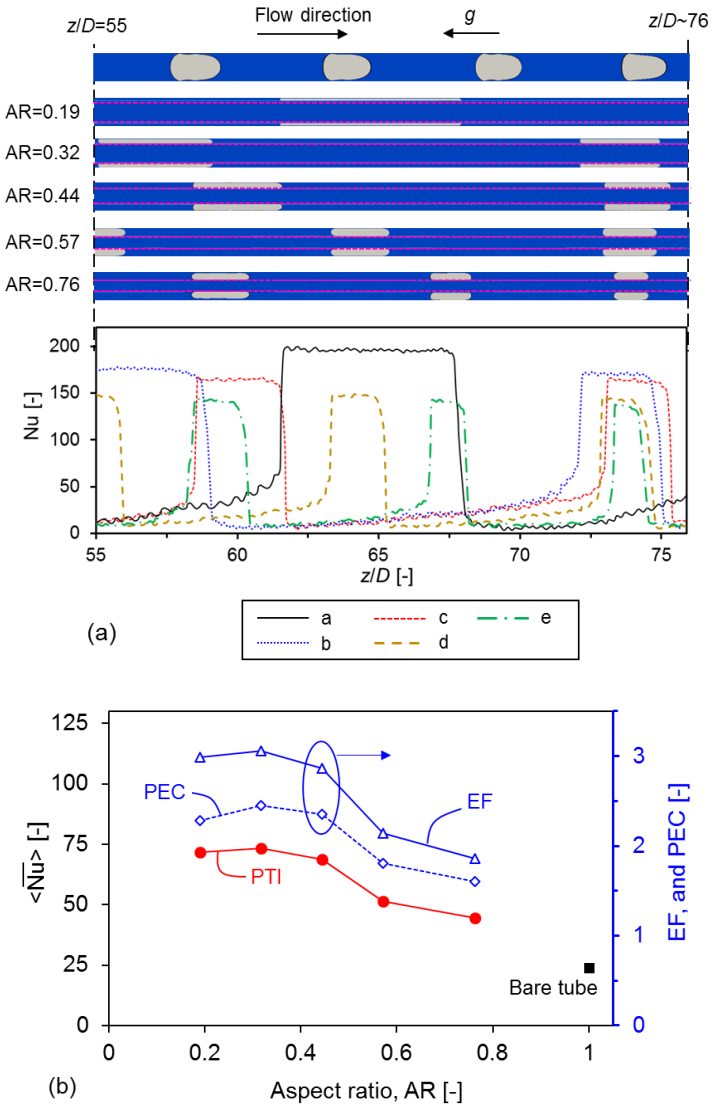

Figure 5.3-10 (a) Condensing slug in a bare tube and PTI condensers for different gap dimension and the variation of local Nusselt number; (b) the effect of aspect ratio on the area-time-averaged Nusselt number enhancement factor (EF), and performance evaluation criterion (PEC)

Figures 5.3-10(b) shows the computed area-time-averaged Nusselt numbers as well as the enhancement factor (EF) and performance evaluation criterion (PEC) for all of the PTI cases considered in this parametric study. It is shown that all cases using a PTI have higher Nusselt number than that in the bare tube. Interestingly, there exists an optimum aspect ratio (AR) for a maximum of the average Nusselt number. This is mainly caused by the total area occupied by the confined bubbles and partially caused by the magnitude of the convective heat transfer in liquid slugs. The maximum average Nusselt number of 73.35 was achieved with AR=0.32 of Case b (Table 5.3-3) that is about three times higher than that in the bare tube condenser (EF=3.05). In addition, by considering the penalty factor caused by pressure drop, Case b with AR=0.32 has the maximum PEC of about 2.45.

5.3.5 Effect of gravity

The computational simulation of flow condensation of isobutene in a porous-tube-insert (PTI) condenser was performed under microgravity ($10^{-4}g_o$) condition. The flow and geometrical conditions are the same described in Section 5.3.2, except the gravitational magnitude. It is seen from Fig. 5.3-11(a) that, under normal gravity, the large density difference of liquid and gas bubble induces a buoyancy force to produce the liquid circulations around the confined bubble in the PTI section. However, the scenario is different under microgravity and the liquid circulation is absent due to the diminished buoyancy effect [Fig. 5.3-11(b)]. In microgravity, liquid is continuously pushed towards the inside of the porous tube, and the liquid slug between two neighboring bubbles are gradually shortened, and finally disappears and the segmented confined bubbles are completely merged. Under this condition, the entire annular gap region is occupied by the ultra-thin liquid film on the tube wall.

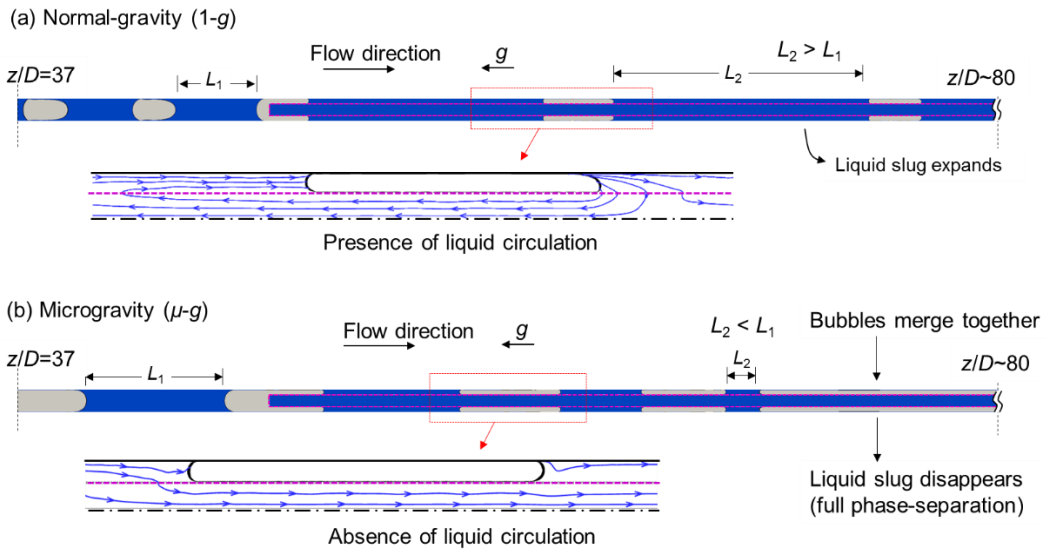

Figure 5.3-11 The slug flow condensation in a PTI condenser and the hydrodynamics of liquid streamlines around a single bubble in (a) normal gravity; and (b) microgravity condition

Figures 5.3-11(a-b) show the bubble velocities along the flow direction in the bare tube and PTI section for both normal 5.3-11(a)] and microgravity condition 5.3-11(b)]. It is shown that under normal gravity 5.3-11(a)], the bubble accelerates when entering to the PTI section due to the counter-current flow of upward gas bubble in the annular gap and downward liquid inside the porous tube. However, under microgravity 5.3-11(b)], the bubble decelerate after entering the PTI section due to the friction caused by the tube wall and the porous tube surface. This is a reason that liquids in liquid slugs flowing from the annular region to the core region under microgravity condition.

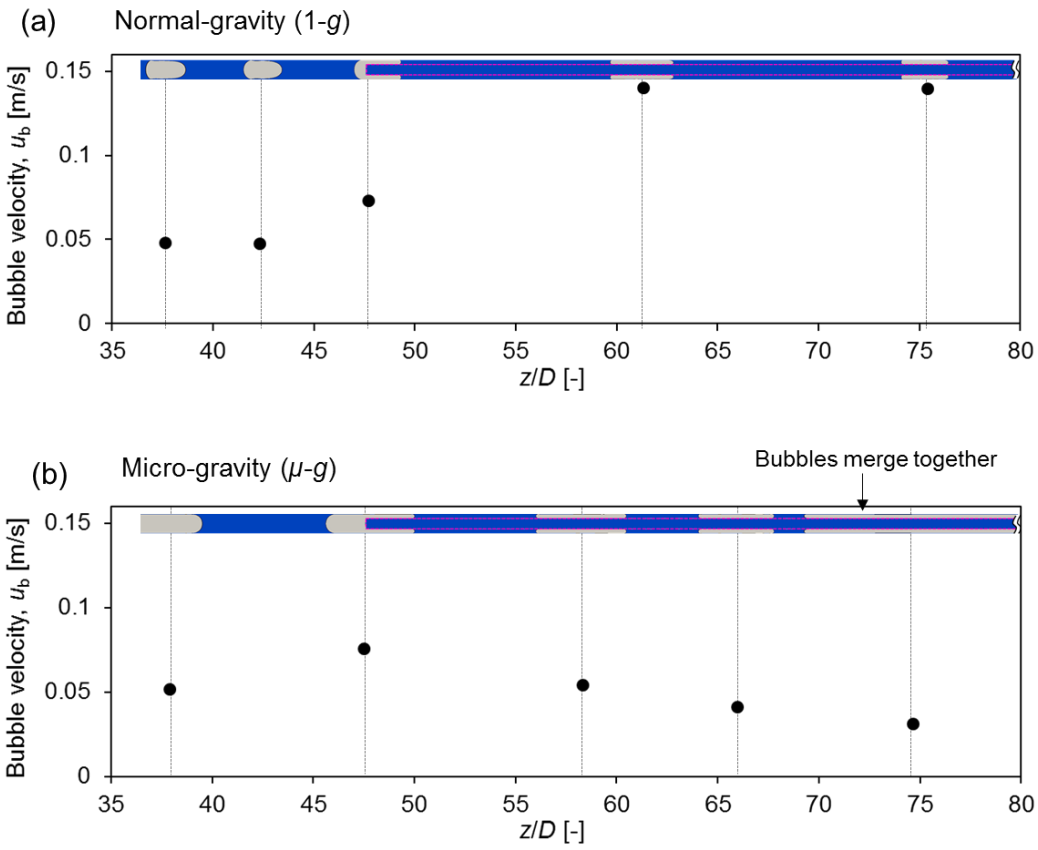

Figure 5.3-12 Bubble velocities along the flow direction of a condenser in a bare tube section and PTI section for (a) normal gravity; and (b) microgravity condition

Figures 5.3-12(a-b) show the condensing slug flow of isobutene in a bare tube and PTI condenser under microgravity condition. Figure 5.3-13(c) compares the variation of local Nusselt number in the selected downstream region ($55D < z < 80D$) for bare tube and PTI condenser. It is apparent that the peak values of Nusselt number is increased in PTI section due to the reduced film thickness similar to that under normal gravity [Fig. 5.3-4]. However, under microgravity, the area occupied by the ultra-thin film is also increased due to the bubble coalescence at the condenser downstream.

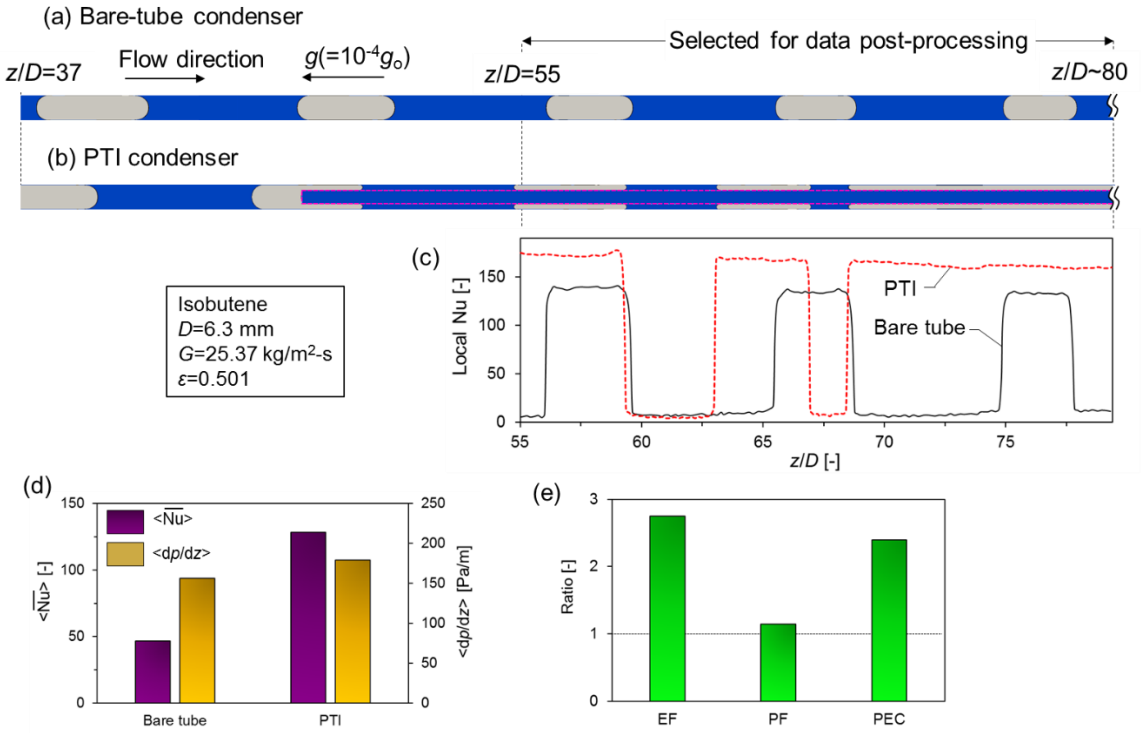

Figure 5.3-13 The effect of gravity on condensing flow in (a) bare tube and (b) PTI condenser under microgravity; and (c) variation of local film Nusselt number in the bare tube and PTI section under

The calculated area-time-averaged Nusselt number and time-averaged pressure gradients for bare tube and PTI condenser under microgravity were also compared in Fig. 5.3-13(d). It is shown that the average Nusselt number in the bare-tube (~46.67) is substantially increased up to (~128.33) in the PTI condenser while the pressure gradient is slightly increased from bare tube (~156.11 Pa/m) to PTI condenser (~179.06 Pa/m). Fig. 5.3-13(e) also presents the computed values of enhancement factor (PF), pressure drop penalty (PF), as well as the performance evaluation criteria (PEC). It is seen that, the condensation heat transfer in the PTI condenser is significantly enhanced as compared to the bare-tube condenser (EF~2.74), which is accompanied by 15% pressure drop penalty (PF~1.15) leading to the increased overall performance of PEC~2.4.

5.3.6 Summary

Computational fluid dynamics (CFD) simulations were carried out to investigate the condensation heat transfer enhancement in slug flows using capillary-assisted phase separation. The condensing flow of isobutene in a vertical upward direction was considered where a porous-tube insert was suspended in the condenser tube. Simulation results show that the capillary phase-separation prevented the bubbles to penetrate through the pores of the porous tube and from entering the porous tube keeping the bubbles in the annular gap resulting in an elongated ultra-thin liquid film near the tube wall. It was found that by using the porous-tube insert, the heat transfer significantly enhanced due to the reduction of film thickness and increasing the area occupied by the ultra-thin film near the wall. Finally, it was shown that the performance of porous-tube insert is affected by vapor void fraction and it was also demonstrated that there exists an optimum dimension of the annular gap between the tube wall and porous tube for the maximum heat transfer. The maximum achieved Nusselt number in the porous-tube insert condenser considered in this study was nearly three times higher than that in a bare tube condenser. In addition, it was shown that the proposed design can substantially enhances the flow condensation heat transfer under microgravity condition.

6 CONCLUSIONS

6.1 CAPILLARY FLOW

The hydrodynamic characteristics of capillary-driven liquid rise in a vertical capillary tube was experimentally and numerically studied. An experimental work was performed to capture the instantaneous capillary height and meniscus shape of water rise in glass cylindrical tubes of two different diameters. The experimentally-observed (apparent) contact angles were corrected accounting for optical distortion. It was shown that the typical LWR model assuming constant (equilibrium) contact angle can be significantly improved by using the appropriate dynamic contact angle model. Then, a computational fluid dynamics (CFD) model based on the volume of fluid-continuum surface force (VOF-CSF) method was developed to simulate the capillary rise accounting for velocity-dependent dynamic contact angle. It was found that using the dynamic contact angle, the numerical results for the capillary height agreed well with those observed in the experimental observation and eliminates the unphysical oscillations that was predicted by using constant contact angle. It was also shown that, under certain condition, the CFD model successfully simulated the realistic oscillation around the equilibrium capillary height.

6.1.1 Recommendation for future work

Although the instantaneous contact angle is known to be the most important parameter that affect the inaccurate calculation of the capillary flows, there are also other factors that attributes to this matter. It is recommended to study the entrance (inlet) effect, displaced gas (outlet) effect, and capillary radius (diameter) effect on capillary rise. Moreover, it is suggested to further investigate the oscillation around the equilibrium height

and the geometry and condition where this oscillation occurs. The non-dimensional analysis of acting forces could be a helpful approach to find out such critical condition for the capillary oscillations. In addition, the capillary rise with surface evaporation is another important practical problem and of interest for further study.

6.2 ADIABATIC TWO-PHASE FLOW

In this research, the hydrodynamics of adiabatic (isothermal) gas-liquid two-phase flows in a circular tube were studied. First, a set of visualization experiments was carried out to observe different two-phase flow regimes. The experimentally-observed stratified, wavy, plug and slug flow regimes were found to be consistent with Mandhane's flow map except annular flow that was observed at relatively lower gas superficial velocities and also wavy flows were observed at relatively higher water superficial velocities. The differences were attributed to different experimental conditions (e.g., tube diameter), complex behavior of two-phase flow near the transition zone and subjective classification of observed flow regimes by researchers.

Then, computational fluid dynamic (CFD) simulations were performed based on the VOF-CSF method using OpenFOAM to simulate different two-phase flows. Experimental and numerical results were generally consistent in the qualitative prediction of flow regimes. In addition, the comparison of the hydrodynamic features (e.g. void fraction, pressure drop) of the simulated cases showed acceptable agreement with the selected empirical correlations in literature.

Next, the hydrodynamic behavior of two-phase flow was studied under reduced gravity conditions. Horizontal plug/bubble flows and a vertical upward slug flow was

selected as the baseline condition for gravitational influence. The gravity level used for the simulations ranged from $10^{-4}g_o$ (micro) to $2g_o$ (hyper) to address the space colonization environments. It was found that in horizontal flow, by reducing the gravity, two-phase flow regime changes from plug to bubble flow as a result of bubble detachment from the tube wall. In addition, the two-phase pressure drop was minimum around normal gravity as a result of two major competing effects of reduced slip ratio (decreased interfacial shear stress) and liquid acceleration (increased wall shear stress).

The simulation results for vertical upward slug slow showed that the Taylor bubbles are shortened more than the liquid slugs by increasing gravity. Analysis of the flow field around a Taylor bubble reveals that a reversal of wall shear stress caused by a falling-film flow can create a positive frictional pressure gradient in the vertical slug flow. The falling film flow is intensified by increasing gravity, whereas at microgravity, no falling film exists around a Taylor bubble. The total pressure gradients, however, are always positive and increase monotonically by increasing gravity due to the increased hydrostatic pressure gradient. The rising velocity of a Taylor bubble was found to be minimum around normal gravity.

6.2.1 Recommendation for future work

In order to improve the available two-phase flow maps, it is suggested to perform experiments in a wide range of flow conditions to provide a large body of data, specially near the transition area. For the numerical simulation, it is recommended to improve the two-phase flow simulation for the turbulence cases by using a sophisticated turbulence modeling. Also, regarding the two-phase flow under reduced gravities, it is suggested to

analyze the gravitational influence on other two-phase flow regimes such as annular flow, bubbly flow, and stratified flow.

6.3 NON-CONDENSING TWO PHASE FLOW

This work focused on the convective heat transfer enhancement of non-condensing slug flows by using phase separation for local liquid circulations through a porous-tube insert (PTI). Numerical simulations using the Volume of Fluid-Continuum Surface Force (VOF-CSF) method were carried out to study the air-water slug flow and heat transfer without phase change in a vertical upward flow. The rear end (exit) of the porous tube was open to allow discharge of fluid, but two different designs of the frontal end were considered; a porous tube with a closed front that prevents the bubbles from entering the porous tube and keeps the bubbles in the annular gap; a porous tube with an open front allows the bubbles to flow through the porous tube. Simulation results show that a counter flow of the bulk liquid inside and outside the porous tube creates internal liquid circulations in both the axial and radial directions, resulting in an increased liquid velocity near the tube wall, thus an enhanced convective heat transfer.

In addition, a set of parametric simulations was systematically carried out for an optimization of the annular gap dimension (or porous tube diameter) for the maximum heat transfer. It was found that there exists an optimum diameter of the porous-tube-insert (or annular gap dimension between the tube wall and porous tube) for convective heat transfer enhancement. The intriguing variation of the Nusselt number with the gap dimension is explained by the magnitude of the liquid velocities near the tube wall, the length (area) occupied by the high liquid velocity zone near the wall, and the film thickness in the bubble

region. The maximum Nusselt number of the porous-tube-insert cases used in this study was about five times higher than that of the liquid-only flow in a bare tube.

6.3.1 Recommendation for future work

It is recommended to study the performance of the porous-tube-insert (PTI) design in convective heat transfer for other two-phase flow configurations such as vertical downward slug flow, horizontal plug flow, and bubbly flow. It would be also interesting to investigate other parametric studies such as the effect of pore diameter, subcooled temperature, and inlet condition on the convective heat transfer performance of PTI. Furthermore, the performance of porous-tube-insert design in non-condensing two phase flow under reduced gravities is another subject of interest.

6.4 CONDENSING TWO-PHASE FLOW

The computational fluid dynamics (CFD) model was improved to account for phase change. First, the numerical model validated using the available classical problems in literature. Next, the computational fluid dynamics (CFD) simulations were carried out to investigate the condensation heat transfer enhancement in slug flows using capillary-assisted phase separation. The condensing flow of isobutene in a vertical upward direction was considered where a porous-tube insert was suspended in the condenser tube. Simulation results show that the capillary phase-separation prevented the bubbles to penetrate through the pores of the porous tube and from entering the porous tube keeping the bubbles in the annular gap resulting in an elongated ultra-thin liquid film near the tube wall. It was found that by using the porous-tube insert, the heat transfer significantly

enhanced due to the reduction of film thickness and increasing the area occupied by the ultra-thin film near the wall.

Then through a set of parametric study, it was shown that the performance of porous-tube insert is affected by vapor void fraction and it was also demonstrated that there exists an optimum dimension of the annular gap between the tube wall and porous tube for the maximum heat transfer. The maximum achieved Nusselt number in the porous-tube insert condenser considered in this study was nearly three times higher than that in a bare tube condenser. Furthermore, it was shown that the PTI significantly enhanced the condensation heat transfer under microgravity condition.

6.4.1 Recommendation for future work

In order to support the numerical results obtained in this work, it is recommended to perform an experimental study of flow condensation using PTI. For the numerical simulation, it is suggested to study the condensation heat transfer performance of porous-tube-insert (PTI) design for other two-phase flow configuration, especially for the case of three-dimensional (3-D) stratified flow.

REFERENCES

1. G. De Marsily, *Quantitative hydrogeology*, 1986. Paris School of Mines, Fontainebleau.
2. K. Vafai, *Porous media: applications in biological systems and biotechnology*, 2010. CRC Press.
3. S. Haeberle, and R. Zengerle, *Microfluidic platforms for lab-on-a-chip applications*, 2007. Lab on a Chip, **7**(9): pp. 1094-1110.
4. F. Maggi, and C. Pallud, *Space agriculture in micro-and hypo-gravity: a comparative study of soil hydraulics and biogeochemistry in a cropping unit on Earth, Mars, the Moon and the space station.* Planetary and Space Science, 2010. **58**(14-15): pp. 1996-2007.
5. Hua Zhang, T. S. Ramakrishnan, Alex Nikolov, and Darsh Wasan, *Enhanced oil recovery driven by nanofilm structural disjoining pressure: flooding experiments and microvisualizatio,*. 2016. Energy & Fuels,. **30**(4): pp. 2771-2779.
6. Lian Zhang, Jae-Mo Koo, Linan Jiang, Mehdi Asheghi, Kenneth E. Goodson, Juan G. Santiago, and Thomas W. Kenny, *Measurements and modeling of two-phase flow in microchannels with nearly constant heat flux boundary conditions*, 2002. Journal of microelectromechanical systems, **11**(1): pp. 12-19.
7. L.L. Crynes, R.L. Cerro, and M.A. Abraham, *Monolith froth reactor: Development of a novel three-phase catalytic system*, 1995. AIChE Journal, **41**(2): pp. 337-345.
8. R. Lucas, *Ueber das Zeitgesetz des kapillaren Aufstiegs von Flüssigkeiten*, 1918. Colloid & Polymer Science, **23**(1): pp. 15-22.
9. E.W. Washburn, *The dynamics of capillary flow*, 1921. Physical review, **17**(3): p. 273.

10. E.K. Rideal, *CVIII. On the flow of liquids under capillary pressure.* The London, Edinburgh, and Dublin Philosophical Magazine and Journal of Science, 1922. **44**(264): pp. 1152-1159.

11. S. Leelajariyakul, H. Noguchi, and S. Kiatkamjornwong, *Surface-modified and micro-encapsulated pigmented inks for ink jet printing on textile fabrics,* 2008. Progress in Organic Coatings, **62**(2): pp. 145-161.

12. L. Fisher, *Physics takes the biscuit.* Nature, 1999. **397**(6719): p. 469.

13. A. Nikolov, and H. Zhang, *The dynamics of capillary-driven two-phase flow: The role of nanofluid structural forces,* 2015. Journal of colloid and interface science, **449**: pp. 92-101.

14. A. Hamraoui, Krister Thuresson, Tommy Nylander, and Vassili Yaminsky, *Can a dynamic contact angle be understood in terms of a friction coefficient?,* 2000. Journal of Colloid and Interface Science, **226**(2): pp. 199-204.

15. A. Hamraoui, and T. Nylander, *Analytical approach for the Lucas–Washburn equation,* 2002. Journal of colloid and interface science, **250**(2): pp. 415-421.

16. O'Loughlin, Muireann, K. Wilk, C. Priest, J. Ralston, and M. N. Popescu, *Capillary rise dynamics of aqueous glycerol solutions in glass capillaries: a critical examination of the Washburn equation,* 2013. Journal of colloid and interface science. **411**: pp. 257-264.

17. B. Zhmud, F. Tiberg, and K. Hallstensson, *Dynamics of capillary rise*, 2000. Journal of colloid and interface science,. **228**(2): pp. 263-269.

18. T. Andrukh, Daria Monaenkova, Binyamin Rubin, Wah-Keat Lee, and Konstantin G. Kornev, *Meniscus formation in a capillary and the role of contact line friction,*

2000. Soft Matter, **10**(4): pp. 609-615.

19. F. Maggi, and F. Alonso-Marroquin, *Multiphase capillary flows,* 2012. International Journal of Multiphase Flow, **42**: pp. 62-73.
20. Wu, P., A.D. Nikolov, and D.T. Wasan, *Capillary rise: validity of the dynamic contact angle models.* Langmuir, 2017. **33**(32): p. 7862-7872.
21. P. Wu, Alex D. Nikolov, and Darsh T. Wasan, *Capillary rise: validity of the dynamic contact angle models,* 2017. Langmuir, **33**(32): pp. 7862-7872.
22. F. Schönfeld, and S. Hardt, *Dynamic contact angles in CFD simulations,* 2009. Computers & Fluids, **38**(4): pp. 757-764.
23. R. Cox, *The dynamics of the spreading of liquids on a solid surface. Part 1. Viscous flow.* Journal of Fluid Mechanics, 1986. **168**: pp. 169-194.
24. R.L. Hoffman, *A study of the advancing interface. I. Interface shape in liquid—gas systems.* Journal of colloid and interface science, 1975. **50**(2): pp. 228-241.
25. O. Voinov, *Hydrodynamics of wetting.* Fluid dynamics, 1976. **11**(5): pp. 714-721.
26. Y.D. Shikhmurzaev, *The moving contact line on a smooth solid surface.* International Journal of Multiphase Flow, 1993. **19**(4): pp. 589-610.
27. T. Blake, and J. Haynes, *Kinetics of liquidliquid displacement.* Journal of colloid and interface science, 1969. **30**(3): pp. 421-423.
28. T.-S. Jiang, O. Soo-Gun, and J.C. Slattery, *Correlation for dynamic contact angle.* Journal of Colloid and Interface Science, 1979. **69**(1): pp. 74-77.
29. S.F. Kistler, *Hydrodynamics of wetting.* Wettability, 1993. **6**: pp. 311-430.
30. J.E. Seebergh, and J.C. Berg, *Dynamic wetting in the low capillary number regime.* Chemical Engineering Science, 1992. **47**(17-18): pp. 4455-4464.

31. S. Kalliadasis, and H.C. Chang, *Apparent dynamic contact angle of an advancing gas–liquid meniscus.* Physics of Fluids, 1994. **6**(1): pp. 12-23.

32. M.Y. Zhou, and P. Sheng, *Dynamics of immiscible-fluid displacement in a capillary tube.* Physical Review Letters, 1990. **64**(8): p. 882.

33. S. Newman, *Kinetics of wetting of surfaces by polymers; capillary flow.* Journal of colloid and interface science, 1968. **26**(2): pp. 209-213.

34. F. Schönfeld, and S. Hardt, *Dynamic contact angles in CFD simulations,* 2009.Computers & Fluids, **38**(4): pp. 757-764.

35. A.A. Saha, and S.K. Mitra, *Effect of dynamic contact angle in a volume of fluid (VOF) model for a microfluidic capillary flow,* 2009. Journal of colloid and interface science. **339**(2): pp. 461-480.

36. S. Afkhami, S. Zaleski, and M. Bussmann, *A mesh-dependent model for applying dynamic contact angles to VOF simulations,* 2009. Journal of Computational Physics, **228**(15): pp. 5370-5389.

37. D. Deganello, T. N. Croft, A. J. Williams, A. S. Lubansky, D. T. Gethin, and T. C. Claypole, *Numerical simulation of dynamic contact angle using a force based formulation,* 2011. Journal of Non-Newtonian Fluid Mechanics, **166**(16): pp. 900-907.

38. Yamamoto, Yasufumi, Takahiro Ito, Tatsuro Wakimoto, and Kenji Katoh, *Numerical simulations of spontaneous capillary rises with very low capillary numbers using a front-tracking method combined with generalized Navier boundary condition,* 2013. International Journal of Multiphase Flow, **51**: pp. 22-32.

39. J.D. Boadway, and E. Karahan, *Correction of laser Doppler anemometer readings*

for refraction at cylindrical interfaces. DISA information, 1981: pp. 4-6.

40. Durrett, R. P., R. D. Gould, W. H. Stevenson, and H. D. Thompson, *A correction lens for laser Doppler velocimeter measurements in a cylindrical tube.* AIAA journal, 1985. **23**(9): pp. 1387-1391.
41. Y. Agrawal, L. Talbot, and K. Gong, *Laser anemometer study of flow development in curved circular pipes.* Journal of Fluid Mechanics, 1978. **85(**3): pp. 497-518.
42. S.A. Ahmed, and D.P. Giddens, *Flow disturbance measurements through a constricted tube at moderate Reynolds numbers.* Journal of biomechanics, 1983. **16**(12): pp. 955-963.
43. Lowe, M. and P. Kutt, *Refraction through cylindrical tubes.* Experiments in fluids, 1992. **13**(5): pp. 315-320.
44. Siebold, Alain, Michel Nardin, Jacques Schultz, André Walliser, and Max Oppliger, *Effect of dynamic contact angle on capillary rise phenomena.* Colloids and surfaces A: Physicochemical and engineering aspects, 2000. **161**(1): pp. 81-87.
45. Xue, H. T., Z. N. Fang, Y. Yang, J. P. Huang, and L. W. Zhou, *Contact angle determined by spontaneous dynamic capillary rises with hydrostatic effects: Experiment and theory.* Chemical Physics Letters, 2006. **432**(1-3): pp. 326-330.
46. O. Baker, *Design of pipelines for the simultaneous flow of oil and gas*. in *Fall Meeting of the Petroleum Branch of AIME*. 1953: Society of Petroleum Engineers.
47. J. Mandhane, G. Gregory, and K. Aziz, *A flow pattern map for gas—liquid flow in horizontal pipes.* International Journal of Multiphase Flow, 1974. **1**(4): pp. 537-553.
48. Y. Taitel, and A. Dukler, *A model for predicting flow regime transitions in*

horizontal and near horizontal gas-liquid flow. AIChE journal, 1976. **22**(1): pp. 47-55.

49. C.C.-W. Tang, *Study of Heat Transfer in Non-boiling Two-phase Gas-liquid Flow in Pipes for Horizontal, Slightly Inclined, and Vertical Orientations*. 2011, Oklahoma State University.

50. G.W. Govier, and K. Aziz, *The flow of complex mixtures in pipes*. Vol. 469. 1972: Van Nostrand Reinhold New York.

51. M.L. Lamari, *An Experimental Investigation of Two-phase (air-water) Flow Regimes in Horizontal Tube at Near Atmospheric Conditions*. 2001: Carleton University.

52. López, Jorge, Hugo Pineda, David Bello, and Nicolás Ratkovich, *Study of liquid–gas two-phase flow in horizontal pipes using high speed filming and computational fluid dynamics.* Experimental Thermal and Fluid Science, 2016. **76**: pp. 126-134.

53. S.C. De Schepper, G.J. Heynderickx, and G.B. Marin, *CFD modeling of all gas–liquid and vapor–liquid flow regimes predicted by the Baker chart.* Chemical Engineering Journal, 2008. **138**(1-3): pp. 349-357.

54. M.J. Vaze, and J. Banerjee, *Visualization of Air-Water Type Two-Phase Flow Patterns.* IUP Journal of Mechanical Engineering, 2010. **3**(3).

55. H. Jasak, *OpenFOAM: open source CFD in research and industry.* International Journal of Naval Architecture and Ocean Engineering, 2009. **1**(2): pp. 89-94.

56. J. Polansky, M. Wang, and Y. Faraj. *Numerical modelling of gas-liquid flow phenomena in horizontal pipelines*. in *Leeds Proceedings*. 2015.

57. A.M. Shuard, H.B. Mahmud, and A.J. King. *Comparison of two-phase pipe flow in*

OpenFOAM with a mechanistic model. in *IOP Conference Series: Materials Science and Engineering*. 2016: IOP Publishing.

58. J.P. Thaker, and J. Banerjee. *CFD simulation of two-phase flow phenomena in horizontal pipelines using openfoam*. in *Proc. 40th Nat. Conf. on Fluid Mech. & Fluid Power*. 2013.

59. V.E. Vershinin, R.M. Ganopolsky, and V.O. Polyakov, *Numerical modeling of two-dimensional gas-liquid flow structures.* Modern Applied Science, 2015. **9**(2): p. 236.

60. M. Narcy, and C. Colin, *Two-Phase Pipe Flow in Microgravity with and without Phase Change: recent progress and future prospects.* Interfacial Phenomena and Heat Transfer, 2015. **3**(1).

61. D. Heppner, C. King, and J. Littles, *Zero-G experiments in two-phase fluids flow regimes.* American Society of Mechanical Engineers, 1975.

62. Dukler, A. E., J. A. Fabre, J. B. McQuillen, and R. Vernon, *Gas-liquid flow at microgravity conditions: flow patterns and their transitions.* International Journal of Multiphase Flow, 1988. **14**(4): pp. 389-400.

63. C. Colin, J. Fabre, and A. Dukler, *Gas-liquid flow at microgravity conditions—I. Dispersed bubble and slug flow.* International Journal of Multiphase Flow, 1991. **17**(4): pp. 533-544.

64. L. Zhao, and K. Rezkallah, *Gas-liquid flow patterns at microgravity conditions.* International Journal of Multiphase Flow, 1993. **19**(5): pp. 751-763.

65. L. Zhao, and K. Rezkallah, *Pressure drop in gas-liquid flow at microgravity conditions.* International journal of multiphase flow, 1995. **21**(5): pp. 837-849.

66. W. Bousman, J. McQuillen, and L. Witte, *Gas-liquid flow patterns in microgravity: effects of tube diameter, liquid viscosity and surface tension.* International Journal of Multiphase Flow, 1996. **22**(6): pp. 1035-1053.

67. B. Choi, T. Fujii, H. Asano, K. Sugimoto, *A study of the flow characteristics in air-water two-phase flow under microgravity*. JSME International Journal Series B Fluids and Thermal Engineering, 2003. **46**(2): pp. 262-269.

68. T.A. Hamm, F.R. Best, *Gravity dependent flow regime mapping*. in *AIP Conference Proceedings*. 1997: AIP, pp. 635-640

69. R. Balasubramaniam, E. Rame, J. Kizito, M. Kassemi, *Two phase flow modeling: Summary of flow regimes and pressure drop correlations in reduced and partial gravity.* 2006.

70. K. Hurlbert, L. Witte, F. Best, C. Kurwitz, *Scaling two-phase flows to Mars and Moon gravity conditions.* International journal of multiphase flow, 2004. **30**(4): pp. 351-368.

71. N. Clarke, and K. Rezkallah, *A study of drift velocity in bubbly two-phase flow under microgravity conditions.* International journal of multiphase flow, 2001. **27**(9): pp. 1533-1554.

72. K.S. Gabriel, *Microgravity Two-phase flow and heat transfer*. 2007: Springer.

73. A.-S. Yang, *Investigation of liquid–gas interfacial shapes in reduced gravitational environments.* International Journal of Mechanical Sciences, 2008. **50**(8): pp. 1304-1315.

74. X. Liu, Y. Chen, and M. Shi, *Influence of gravity on gas–liquid two-phase flow in horizontal pipes.* International journal of multiphase flow, 2012. **41**: pp. 23-35.

75. F. Hassanipour, and J.L. Lage, *Preliminary experimental study of a bio-inspired, phase-change particle capillary heat exchanger.* International Journal of Heat and Mass Transfer, 2010. **53**(15-16): pp. 3300-3307.

76. A. Kiaee, and L. Jose'L. *Particle Size and Speed Effects on the Sweeping Convection in Straight, Isoflux Channels*. in *ASTFE Digital Library*, Begel House Inc., 2017.

77. A. Kiaee, N. Crowe, and L. Jose'L. *Numerical Study of the Distance Between Two Particles Effect on Sweeping Convection in a Straight Isotherm Channel*. in *ASTFE Digital Library*, Begel House Inc., 2018.

78. D. Oliver, and A.Y. Hoon, *Two-Phase Non-Newtonian Flow. Part II: Heat Transfer.* Transactions of the Institution of Chemical Engineers, 1968. **46**(4): pp.T116-T122.

79. D. Lakehal, G. Larrignon, and C. Narayanan, *Computational heat transfer and two-phase flow topology in miniature tubes.* Microfluidics and nanofluidics, 2008. **4**(4): p. 261.

80. R. Gupta, D.F. Fletcher, and B.S. Haynes, *CFD modelling of flow and heat transfer in the Taylor flow regime.* Chemical Engineering Science, 2010. **65**(6): pp. 2094-2107.

81. A. Mehdizadeh, S. Sherif, and W. Lear, *Numerical simulation of thermofluid characteristics of two-phase slug flow in microchannels.* International Journal of Heat and Mass Transfer, 2011. **54**(15-16): pp. 3457-3465.

82. T. Bandara, N.T. Nguyen, and G. Rosengarten, *Slug flow heat transfer without phase change in microchannels: a review.* Chemical Engineering Science, 2015.

126: pp. 283-295.

83. S. Gat, N. Brauner, and A. Ullmann, *Heat transfer enhancement via liquid–liquid phase separation.* International Journal of Heat and Mass Transfer, 2009. **52**(5-6): pp. 1385-1399.

84. W. Xing, A.K. Vutha, X. Yu, A. Ullmann, N. Brauner, and Y. Peles, *Liquid/liquid phase separation heat transfer at the microscale.* International Journal of Heat and Mass Transfer, 2017. **107**: pp. 53-65.

85. A. Ullmann, K. Maevski, and N. Brauner, *Enhancement of forced and free convection heat transfer rates by inducing liquid–liquid phase separation of a partially-miscible equal-density binary liquid system.* International Journal of Heat and Mass Transfer, 2014. **70**: pp. 363-377.

86. H. Chen, J. Xu, Z. Li, F. Xing, J. Xie, W. Wang, and W. Zhang, *Flow pattern modulation in a horizontal tube by the passive phase separation concept.* International Journal of Multiphase Flow, 2012. **45**: pp. 12-23.

87. Q. Chen, J. Xu, D. Sun, Z. Cao, J. Xie, and F. Xing, *Numerical simulation of the modulated flow pattern for vertical upflows by the phase separation concept.* International Journal of Multiphase Flow, 2013. **56**: pp. 105-118.

88. W. Nusselt, *The surface condensation of water vapour*. Zeitschrift Des Vereines Deutscher Ingenieure, 1916. **60**: pp. 541-546.

89. J. Royal, and A. Bergles, *Augmentation of horizontal in-tube condensation by means of twisted-tape inserts and internally finned tubes*. Journal of Heat Transfer, 1978. **100**(1): pp. 17-24.

90. M. Luu, and A.E. Bergles, *Enhancement of Horizontal In-Tube Condensation of R-*

113, ASHRAE Trans, **86**: pp. 293-312.

91. A. Dalkilic, and S. Wongwises, *Intensive literature review of condensation inside smooth and enhanced tubes.* International Journal of Heat and Mass Transfer, 2009. **52**(15-16): pp. 3409-3426.

92. Chen Hongxia, Jinliang Xu, Zijin Li, Feng Xing, Jian Xie, Wei Wang, and Wei Zhang, *Flow pattern modulation in a horizontal tube by the passive phase separation concept.* International Journal of Multiphase Flow, 2012. **45**: pp. 12-23.

93. Chen, Hongxia, Jinliang Xu, Zijin Li, Feng Xing, and Jian Xie., *Stratified two-phase flow pattern modulation in a horizontal tube by the mesh pore cylinder surface.* Applied energy, 2013. **112**: pp. 1283-1290.

94. Sun, DongLiang, JinLiang Xu, QiCheng Chen, and Zhen Cao., *Numerical study of flow pattern modulation in a vertical phase separation condenser tube.* Chinese Science Bulletin, 2013. **58**(13): pp. 1592-1598.

95. Xie Jian, Jinliang Xu, Feng Xing, Zixuan Wang, and Huan Liu, *The phase separation concept condensation heat transfer in horizontal tubes for low-grade energy utilization.* Energy, 2014. **69**: pp. 787-800.

96. Xie Jian, Jinliang Xu, Yu Cheng, Feng Xing, and Xiaotian He, *Condensation heat transfer of R245fa in tubes with and without lyophilic porous-membrane-tube insert.* International Journal of Heat and Mass Transfer, 2015. **88**: pp. 261-275.

97. C.R. Kharangate, and I. Mudawar, *Review of computational studies on boiling and condensation.* International Journal of Heat and Mass Transfer, 2017. **108**: pp. 1164-1196.

98. C.W. Hirt, and B.D. Nichols, *Volume of fluid (VOF) method for the dynamics of*

free boundaries. Journal of computational physics, 1981. **39**(1): pp. 201-225.

99. J.U. Brackbill, D.B. Kothe, and C. Zemach, *A continuum method for modeling surface tension.* Journal of computational physics, 1992. **100**(2): pp. 335-354.

100. H. Rusche, *Computational fluid dynamics of dispersed two-phase flows at high phase fractions*. PhD dissertation, 2003, Imperial College London (University of London).

101. D. A. Hoang, V. van Steijn, L. M. Portela, M. T. Kreutzer, and C. R. Kleijn, *Benchmark numerical simulations of segmented two-phase flows in microchannels using the Volume of Fluid method.* Computers & Fluids, 2013. **86**: pp. 28-36.

102. J. Klostermann, K. Schaake, and R. Schwarze, *Numerical simulation of a single rising bubble by VOF with surface compression.* International Journal for Numerical Methods in Fluids, 2013, **71**(8): pp. 960-982.

103. Fukagata, K., et al., *Numerical simulation of gas–liquid two-phase flow and convective heat transfer in a micro tube.* International Journal of Heat and Fluid Flow, 2007. **28**(1): p. 72-82.

104. Lafaurie, Bruno, Carlo Nardone, Ruben Scardovelli, Stéphane Zaleski, and Gianluigi Zanetti, *Modelling merging and fragmentation in multiphase flows with SURFER.* Journal of Computational Physics, 1994. **113**(1): pp. 134-147.

105. O. Ubbink, *Numerical prediction of two fluid systems with sharp interfaces.* Ph.D. dissertation, 1997, Imperial College of Science, Technology and Medicine, London.

106. F. Jamshidi, H. Heimel, M. Hasert, X. Cai, O. Deutschmann, H. Marschall, and M. Wörner, *On suitability of phase-field and algebraic volume-of-fluid OpenFOAM®*

solvers for gas–liquid microfluidic applications. Computer Physics Communications, 2019, **236**: pp. 72-85.

107. M. Aboukhedr,, A. Georgoulas, M. Marengo, M. Gavaises, and K. Vogiatzaki, *Simulation of micro-flow dynamics at low capillary numbers using adaptive interface compression.* Computers & Fluids, 2018, **165**: pp. 13-32.

108. D.J. Harvie, M. Davidson, and M. Rudman, *An analysis of parasitic current generation in volume of fluid simulations.* Applied Mathematical Modelling, 2006, **30**(10): pp. 1056-1066.

109. A.Q. Raeini, M.J. Blunt, and B. Bijeljic, *Modelling two-phase flow in porous media at the pore scale using the volume-of-fluid method.* Journal of computational physics, 2012, **231**(17): pp. 5653-5668.

110. Quéré, D., É. Raphaël, and J.-Y. Ollitrault, *Rebounds in a capillary tube.* Langmuir, 1999. **15**(10): pp. 3679-3682.

111. Sumner, Ann Louise, Erik J. Menke, Yael Dubowski, John T. Newberg, Reginald M. Penner, John C. Hemminger, Lisa M. Wingen, Theo Brauers, and Barbara J. Finlayson-Pitts., *The nature of water on surfaces of laboratory systems and implications for heterogeneous chemistry in the troposphere.* Physical Chemistry Chemical Physics, 2004. **6**(3): pp. 604-613.

112. P. Lin, and T. Hanratty, *Detection of slug flow from pressure measurements.* International Journal of Multiphase Flow, 1987. **13**(1): pp. 13-21.

113. C. Argyropoulos, and N. Markatos, *Recent advances on the numerical modelling of turbulent flows.* Applied Mathematical Modelling, 2015. **39**(2): pp. 693-732.

114. M.A. Woldesemayat, and A.J. Ghajar, *Comparison of void fraction correlations for*

different flow patterns in horizontal and upward inclined pipes. International journal of multiphase flow, 2007. **33**(4): pp. 347-370.

115. H. Müller-Steinhagen, and K. Heck, *A simple friction pressure drop correlation for two-phase flow in pipes.* Chemical Engineering and Processing: Process Intensification, 1986. **20**(6): pp. 297-308.

116. C. Tribbe, and H. Müller-Steinhagen, *An evaluation of the performance of phenomenological models for predicting pressure gradient during gas–liquid flow in horizontal pipelines.* International Journal of Multiphase Flow, 2000. **26**(6): pp. 1019-1036.

117. J. Thaker, and J. Banerjee, *On intermittent flow characteristics of gas–liquid two-phase flow.* Nuclear Engineering and Design, 2016. **310**: pp. 363-377.

118. A. Tabatabai, and A. Faghri, *A new two-phase flow map and transition boundary accounting for surface tension effects in horizontal miniature and micro tubes.* Journal of heat transfer, 2001. **123**(5): pp. 958-968.

119. X. Lu, and A. Prosperetti, *A numerical study of Taylor bubbles.* Industrial & Engineering Chemistry Research, 2008, **48**(1): pp. 242-252.

120. T. Taha, and Z. Cui, *CFD modelling of slug flow in vertical tubes.* Chemical Engineering Science, 2006, **61**(2): pp. 676-687.

121. D. Nicklin, *Two-phase flow in vertical tubes, Trans.* Transactions of the Institution of Chemical Engineers, 1962, **40**(1): pp. 61-68.

122. Griffith, P. and G.B. Wallis, *Two-phase slug flow.* Journal of Heat Transfer, 1961, **83**(3): pp. 307-317.

123. D.T. Dumitrescu, *Strömung an einer Luftblase im senkrechten Rohr.* ZAMM-

Journal of Applied Mathematics and Mechanics/Zeitschrift für Angewandte Mathematik und Mechanik, 1943, **23**(3): pp. 139-149.

124. K.H. Bendiksen, *On the motion of long bubbles in vertical tubes.* International Journal of Multiphase Flow, 1985, **11**(6): pp. 797-812.

125. A.S. Rattner, and S. Garimella, *Vertical upward intermediate scale Taylor flow: Experiments and kinematic closure.* International Journal of Multiphase Flow, 2015, **75**: pp. 107-123.

126. J. Choi,, E. Pereyra, C. Sarica, C. Park, and J. Kang, *An efficient drift-flux closure relationship to estimate liquid holdups of gas-liquid two-phase flow in pipes.* Energies, 2012, **5**(12): pp. 5294-5306.

127. S.M. Bhagwat, and A.J. Ghajar, *A flow pattern independent drift flux model based void fraction correlation for a wide range of gas–liquid two phase flow.* International Journal of Multiphase Flow, 2014, **59**: pp. 186-205.

128. A. Ansari, M., N. D. Sylvester, O. Shoham, and J. P. Brill., *A comprehensive mechanistic model for upward two-phase flow in wellbores*. Proceedings of SPE Annual Technical Conference and Exhibition, 1990, New Orleans, Louisiana, SPE-20630-MS.

129. E. Lizarraga-Garcia, J. Buongiorno, and M. Bucci, *An analytical film drainage model and breakup criterion for Taylor bubbles in slug flow in inclined round pipes.* International Journal of Multiphase Flow, 2016, **84**: pp. 46-53.

130. D. Langewisch, and J. Buongiorno, *Prediction of film thickness, bubble velocity, and pressure drop for capillary slug flow using a CFD-generated database.* International Journal of Heat and Fluid Flow, 2015, **54**: pp. 250-257.

131. A.J. Ghajar, and S.M. Bhagwat, *Effect of void fraction and two-phase dynamic viscosity models on prediction of hydrostatic and frictional pressure drop in vertical upward gas–liquid two-phase flow.* Heat Transfer Engineering, 2013, **34**(13): pp. 1044-1059.

132. T. Adachi, and H. Uehara, *Correlation between heat transfer and pressure drop in channels with periodically grooved parts.* International Journal of Heat and Mass Transfer, 2001. **44**(22): pp. 4333-4343.

133. C. Dong, and T. Hibiki, *Correlation of heat transfer coefficient for two-component two-phase slug flow in a vertical pipe.* International Journal of Multiphase Flow, 2018. **108**: pp. 124-139.

134. C.J. Geankoplis, *Transport processes and separation process principles:(includes unit operations)*. 2003: Prentice Hall Professional Technical Reference, Fourth Edition, P. 475.

135. C. Kunkelmann, and P. Stephan, *CFD simulation of boiling flows using the volume-of-fluid method within OpenFOAM.* Numerical Heat Transfer, Part A: Applications, 2009. **56**(8): pp. 631-646.

136. A.S. Rattner, and S. Garimella, *Simple mechanistically consistent formulation for volume-of-fluid based computations of condensing flows.* Journal of Heat Transfer, 2014. **136**(7): pp. 071501.

137. Z. Yang, X. Peng, and P. Ye, *Numerical and experimental investigation of two phase flow during boiling in a coiled tube.* International Journal of Heat and Mass Transfer, 2008. **51**(5-6): pp. 1003-1016.

138. Goodson, Kenneth, Anita Rogacs, Milnes David, and Chen Fang, *Volume of fluid*

simulation of boiling two-phase flow in a vapor-venting microchannel. Frontiers in Heat and Mass Transfer (FHMT), 2010. **1**(1).

139. R. Thiele, *Modeling of direct contact condensation with OpenFOAM*. 2010.

140. G.F Hewitt, and D. Roberts, *Studies of two-phase flow patterns by simultaneous x-ray and flast photography*. 1969, Atomic Energy Research Establishment, Harwell, England (United Kingdom).

141. M.M. Shah, *Comprehensive correlations for heat transfer during condensation in conventional and mini/micro channels in all orientations.* International journal of refrigeration, 2016. **67**: pp. 22-41.

142. M.M. Shah, *An improved and extended general correlation for heat transfer during condensation in plain tubes.* Hvac&R Research, 2009. **15**(5): pp. 889-913.

143. W.H. McAdams, *Heat transmission*. 1954. 3rd ed., McGraw Hill, New York.

144. J. El Hajal, J.R. Thome, and A. Cavallini, *Condensation in horizontal tubes, part 1: two-phase flow pattern map.* International Journal of Heat and Mass Transfer, 2003. **46**(18): pp. 3349-3363.

VITA

Milad Darzi was born in Babol, Iran. He completed his Bachelors of Science in Mechanical Engineering at the University of Mazandaran, graduating in June 2010. In June 2014 Milad Received a Master of Science in Mechanical Engineering from the University of Tehran for his thesis work, "Experimental Study of Heat Transfer and Pressure Drop Characteristics during Flow Condensation in Flattened Tubes". Finally, he received a Doctoral Degree also in Mechanical Engineering from the University of Missouri for his work, "Hydrodynamic Characteristics and Capillary-Assisted Heat Transfer Enhancement of Non-Condensing/Condensing Two-Phase Flows". During his PhD at MU, he was responsible for numerous major and minor research projects focusing on two-phase flow and heat transfer with applications within heat-exchangers, heat pipes, gas-lift (bubble) pumps, space-based two-phase systems under reduced gravities, optical visualization, and microfluidics. In particular, he developed various Computational Fluid Dynamics (CFD) models including simulation of phase change (boiling/condensing) flows, dynamic contact angle in capillary flows, and two-phase flow under reduced gravities. Milad start his career outside of academia in January 2020 working for Alpha Omega PDS - ANSYS Certified Channel Partner in Pittsburgh, Pennsylvania as a CFD Application Engineer.